



---

**POLITECHNIKA POZNAŃSKA**

---



Wydział Inżynierii Materiałowej i Fizyki Technicznej

Instytut Fizyki

Zakład Fizyki Molekularnej

**Bartosz Pawałowski**

**Wpływ materiałów nieorganicznych o różnych  
gęstościach na obrazowanie medyczne oraz  
poprawność obliczeń rozkładów dawki w procesie  
radioterapii**

---

Rozprawa doktorska

Promotor

Prof. dr hab. Tomasz Piotrowski

POZNAŃ 2023

Serdecznie dziękuję mojemu Promotorowi Panu Profesorowi Tomaszowi Piotrowskiemu za cenne uwagi, wskazówki oraz poświęcony mi czas.

Serdecznie dziękuję Pani Profesor Alinie Dudkowiak za cenne uwagi oraz pomoc na każdym etapie mojej pracy.

Serdecznie dziękuję wszystkim Współautorom moich prac za pomoc, poświęcony czas oraz cenne uwagi.

# Spis treści

|  |    |
|--|----|
| <b>STRESZCZENIE .....</b>                          | 4  |
| <b>ABSTRACT .....</b>                              | 5  |
| <b>1. Wstęp.....</b>                               | 7  |
| <b>2. Założenia rozprawy.....</b>                  | 11 |
| <b>3. Omówienie prac oraz uzyskane wyniki.....</b> | 12 |
| <b>3.1. Omówienie artykułu numer 1 .....</b>       | 12 |
| <b>3.2. Omówienie artykułu numer 2 .....</b>       | 14 |
| <b>3.3. Omówienie artykułu numer 3 .....</b>       | 16 |
| <b>4. Podsumowanie.....</b>                        | 19 |
| <b>5. Piśmiennictwo.....</b>                       | 21 |

## **STRESZCZENIE**

Prezentowana rozprawa doktorska stanowi cykl artykułów naukowych, w których analizowano wpływ materiałów nieorganicznych o różnych gęstościach na obrazowanie medyczne oraz poprawność obliczeń rozkładów dawki w procesie radioterapii. Analizowany problem wynika przede wszystkim ze zwiększającej się liczby pacjentów posiadających metalowe elementy w swoim ciele, które znacznie wpływają na proces leczenia radioterapeutycznego. Obecność metalowych elementów ze względu na ich dużą gęstość zaburza obraz tomografii komputerowej pacjenta, który jest niezbędny w celu określenia obszaru napromienianego oraz narządów krytycznych. Ze względu na bardzo dużą absorpcję promieniowania jonizującego oraz dodatkowe rozproszenie w obrazie tomografii komputerowej pojawiają się zaburzenia nazywane artefaktami. Pojawiające się artefakty od metalowych elementów w skrajnych sytuacjach uniemożliwiają nie tylko zdefiniowanie zmiany nowotworowej, ale także wpływają na rozkłady liczonych dawek. Wpływa to na możliwość pojawienia się niedokładności zarówno anatomicznych jak i dozymetrycznych podczas realizacji planu leczenia na aparacie terapeutycznym.

W ramach przeprowadzonych badań, w pierwszej pracy, zweryfikowano jedną z dostępnych metod redukujących artefakty, czyli tomografię dwuenergetyczną. Określono parametry skanowania umożliwiające uzyskanie jakościowo najlepszych obrazów. W pracy drugiej oceniono efektywności wykorzystania dwóch różnych metod redukcji artefaktów (tj. tomografia dwuenergetyczna oraz metody algorytmiczne) jak i ich kombinacji w celu poprawy jakości obrazu tomograficznego obszaru, w którym znajduje się element metalowy. W ostatniej pracy z cyklu zweryfikowano wpływ elementów o dużej gęstości (tytan, stal, wolfram) na poprawność obliczeń dawek przy użyciu algorytmów zaimplementowanych w systemie planowania leczenia umożliwiającym przygotowanie komputerowego planu leczenia zawierającego rozkłady dawek.

Na podstawie prac opracowano warunki umożliwiające przygotowanie jakościowo najlepszego obrazu tomograficznego pacjenta, a także warunki pracy jakie należy przestrzegać podczas przygotowywania planu leczenia.

## **ABSTRACT**

The presented doctoral dissertation is a series of scientific articles in which the impact of inorganic materials of various densities on medical imaging and the correctness of calculations of dose distributions in the process of radiotherapy were analyzed. The analyzed problem appears primarily from the increasing number of patients with metal elements in their bodies, which significantly affect the process of radiotherapeutic treatment. The presence of metal elements, due to their high density, disturbs the image of the patient's computed tomography, which is necessary to determine the irradiated area and critical organs. Due to the very high absorption of ionizing radiation and additional scattering, disturbances called artifacts appear in the computed tomography image. Appearing artifacts from metal elements in extreme situations make it impossible to define a shape and localization of tumor and also affect the distribution of calculated doses. This affects anatomical and dosimetric inaccuracies during the realization of the treatment plan on the therapeutic machine.

As part of the research, in the first paper, one of the available artifact reduction methods, i.e. dual-energy tomography, was verified. Scanning parameters have been specified to obtain the best quality images. In the second paper, the effectiveness of the use of two different methods of artifact reduction (i.e. dual-energy tomography and algorithmic methods) and their combination in order to improve the quality of the tomographic image of the area where the metal element is located was assessed. In the last work, the influence of high-density elements (titanium, steel, tungsten) on the correctness of dose calculations was verified using algorithms implemented in the treatment planning system that allows the preparation of a computer treatment plan containing dose distributions.

On the basis of the work, conditions were developed to enable the preparation of the best quality tomographic image of the patient, as well as conditions that should be met during a treatment plan preparation.

## **1. Wstęp**

Od wielu lat radioterapia jest jedną z podstawowych metod leczenia chorób nowotworowych. Osiągnięcie obecnego poziomu wysokiej precyzji deponowania dawki promieniowania jonizującego w ciele pacjenta, wymagało jednak ogromnego postępu technologicznego oraz wielu lat. Już podczas pierwszych zabiegów radioterapeutycznych wykonanych w 1896 roku zaobserwowano szkodliwy wpływ promieniowania X na tkanki zdrowe [1]. Od tego momentu, oprócz zdeponowania właściwej dawki w guzie nowotworowym, nie mniej ważne stało się, podczas napromieniania, ograniczanie dawek dostarczanych do narządów i tkanek zdrowych.

Wśród wielu urządzeń, które znacząco wpłynęły na rozwój radioterapii oraz poprawę efektów leczenia poprzez minimalizację toksyczności, wymienić należy przede wszystkim tomograf komputerowy. Urządzenie po raz pierwszy było klinicznie zastosowane w 1972 i umożliwiło uzyskiwanie dwuwymiarowych przekrojów ciała ludzkiego [2]. Dzięki tej możliwości, naturalnym kierunkiem rozwoju radioterapii było wykorzystanie skanów do określania napromienianych obszarów oraz dalsze obliczanie w nich rozkładów dawek. Obliczenia takie uwzględniają niejednorodności znajdujące się w ciele człowieka.

Współczesny proces leczenia radioterapeutycznego składa się z kilku następujących po sobie etapów:

- 1) Pierwszym etapem jest przygotowanie pacjenta do radioterapii. Polega on na wykonaniu tomografii komputerowej obszaru ciała pacjenta, który zostanie poddany napromienianiu. Na tak uzyskanych obrazach tomograficznych wyznacza się (obrysowuje) guz nowotworowy (obszar tarczowy) i narządy krytyczne znajdujące się w jego sąsiedztwie. Narządy krytyczne to struktury nie zmienione nowotworowo w których łączna wartość zdeponowanej podczas radioterapii dawki powinna być ograniczona i nie powinna przekraczać ścisłe określonej wartości (tzw. dawka tolerancji).
- 2) Kolejnym etapem jest planowanie leczenia, podczas którego fizyk medyczny na przygotowanych skanach tomograficznych pacjenta, przygotowuje komputerowy plan leczenia radioterapeutycznego zawierający informację o odpowiedniej konfiguracji akceleratora (tj. pozycji głowicy, stołu terapeutycznego, układu

kolimatorów oraz np. liczby projekcji terapeutycznych, rodzaju i energii promieniowania), celem uzyskania pożądanego rozkładu dawki terapeutycznej podczas napromieniania.

- 3) Ostatnim etapem jest realizacja leczenia na akceleratorze terapeutycznym zgodnie z przygotowanym planem leczenia oraz schematem dawkowania. Leczenie zazwyczaj realizowane jest przez wiele tygodni. Należy jednak zauważyć, że wysoka precyzaja współczesnych akceleratorów medycznych, umożliwia zmniejszenie dni napromieniania poprzez wzrost dawki dostarczanej podczas jednej, dziennej, frakcji napromieniania.

Mimo ogromnego postępu technologicznego wciąż jednym z największych wyzwań leczenia radioterapeutycznego jest obecność metalowych elementów w ciele pacjenta [3-6]. Prowadzą one do zniekształceń obrazu tomograficznego uniemożliwiając przy tym precyzyjne wyznaczenie obszaru tarczowego i narządów krytycznych oraz obarczając obliczenia dawek przeprowadzane na obrazach tomograficznych dodatkowym błędem.

Głównymi przesłankami do podjęcia badań były odpowiednio: (1) wzrost liczby pacjentów poddawanych radioterapii, którzy posiadają metalowe elementy w swoim ciele (szczególnie wzrost pacjentów po endoprotezoplastyce) [7], (2) brak jednoznacznego stanowiska dotyczącego metod leczenia takich pacjentów jak i (3) metod przygotowania dla nich planu leczenia (tj. minimalizacja artefaktów celem poprawy jakości obrazów tomograficznych jak i ograniczenie błędu obliczeń dawki spowodowanego zaburzeniem obrazu).

Przez wiele lat metalowe elementy w ciele człowieka uniemożliwiały precyzyjną realizację leczenia. Podstawowym problemem były zaburzenia (artefakty) obrazu tomograficznego powstałe pod ich wpływem. Artefakty takie powstają głównie ze względu na pojawiające się dodatkowe rozproszenia promieniowania jonizującego, efekt utwardzania wiązki - polegający na zwiększonej absorpcji promieniowania niskoenergetycznego, a także całkowitego pochłaniania fotonów. Powstałe zaburzenia uniemożliwiają precyzyjne oznaczenie (okonturowanie) napromienianych struktur i w związku z tym obliczone dawki mogą być obarczone dużymi błędami.

Obecnie wyróżnia się dwie podstawowe metody umożliwiające redukcję artefaktów od struktur metalowych na obrazach tomografii komputerowej. Pierwsza metoda wykorzystuje algorytmy obliczeniowe (np. **algorytm iMAR**, z ang. *iterative Metal Artifact Reduction method*), których zadaniem jest detekcja obszarów o zwiększym pochłanianiu promieniowania X oraz ich eliminacja, z wykorzystaniem techniki zamalowywania danych na podstawie interpolacji (inpainting). Drugą metodą jest tomografia dwuenergetyczna (spektralna) (**DECT**, z ang. *dual energy computed tomography*), podczas której obiekt skanowany jest dwukrotnie, raz z niższą i drugi raz z wyższą energią. Tomografia taka poprzez zebranie informacji o liniowym współczynniku osłabiania promieniowania X dla dwóch różnych spektrów energetycznych, umożliwia uzyskanie dodatkowych informacji o budowie skanowanego materiału. Dodatkowo taki zestaw danych umożliwia wygenerowanie serii skanów pseudomonoenergetycznych, gdzie dla wybranych energii (rekonstrukcji) można zaobserwować redukcję artefaktów [8].

Podczas kolejnego etapu realizacji radioterapii, jakim jest planowanie leczenia, trudności pojawiają się podczas obliczania rozkładów dawek. Gdy artefaktów nie da się usunąć z obrazu, można przypisać im gęstości np. wody. Zabieg taki uniemożliwia właściwe określenie napromienianych obszarów anatomicznych, jednakże częściowo redukuje błędy obliczeniowe. W przypadku zastosowania technik niwelujących artefakty kolejnym wyzwaniem jest jednak właściwy wybór algorytmu obliczającego rozkład dawki. Do obliczeń rozkładów dawek obecnie zastosować można kilka różnych algorytmów o różnej precyzyji dokonywanych obliczeń. Współcześnie wykorzystywane algorytmy posiadają pewne ograniczenia, które ujawniają się w skrajnych sytuacjach. Rutynowo wykorzystywane algorytmy umożliwiają precyzyjną realizację obliczeń w obszarach o zbliżonych gęstościach, lecz zawodzą, gdy następuje przejście pomiędzy obszarami o skrajnie różnych gęstościach. W takich przypadkach najlepsze są algorytmy bazujące na symulacjach Monte Carlo. Jednak, należy zauważyć, że takie symulacje zazwyczaj wymagają dużych mocy obliczeniowych oraz długiego czasu prowadzonych obliczeń [9-14].

Obecna w radioterapii różnorodność posiadanych urządzeń, systemów planowania leczenia i dostępności algorytmów, a także ich różnych wersji sprawia, że ośrodki realizujące takie leczenie nie zawsze są w stanie skorzystać z najlepszego rozwiązania. Jednakże realizacja leczenia jest często dla pacjenta jedyną opcją ratującą życie, zatem

porównanie metod redukujących artefakty oraz ich dalszego wpływu na obliczenia jest bardzo ważne. Ponadto lepsze poznanie algorytmów oraz ich ograniczeń staje się niezbędne w przypadku napromieniania nowotworów znajdujących się blisko metalowych elementów oraz do nich przylegających. Ze względu na różnego rodzaju ograniczenia ważne jest, aby realizowane obliczenia uwzględniały zjawiska fizyczne, zachodzące na granicy ośrodków o niskiej i wysokiej gęstości, a także właściwego obliczenia absorbcji promieniowania w metalu, co przekłada się na rozkład dawki.

## **2. Założenia rozprawy**

Celem ogólnym rozprawy była analiza wpływu materiałów nieorganicznych o różnych gęstościach na obrazowanie medyczne oraz poprawność obliczeń rozkładów dawki w procesie radioterapii.

Zadania szczegółowe rozprawy obejmowały:

1. Ocenę jakościową i ilościową pseudomonoenerygetycznych obrazów tomograficznych (PMR) zrekonstruowanych w oparciu o dane uzyskane na podstawie dwuenergetycznej tomografii komputerowej (DECT).
2. Ocena efektywności wykorzystania metod redukcji artefaktów (tj. DECT oraz iMAR) jak i ich kombinacji w celu poprawy jakości obrazu tomograficznego obszaru, w którym znajduje się element metalowy.
3. Weryfikacja wpływu elementów o dużej gęstości (tytan, stal, wolfram) na poprawność obliczeń dawek przy użyciu algorytmów zaimplementowanych w systemie planowania leczenia Eclipse firmy Varian (tj. algorytmy AAA i AXB).

Wyniki badań określone zakresem zadań szczegółowych (**ZS**) zostały przedstawione w cyklu trzech publikacji naukowych. Są to odpowiednio:

**Artykuł 1** (IF: 2.485; MNiSW: 70.000) odpowiadający **ZS 1:**

Pawałowski B, Szweda H, Dudkowiak A, Piotrowski T.

*Quality evaluation of monoenergetic images generated by dual-energy computed tomography for radiotherapy: a phantom study.*

Phys Med 2019;63:48–55. doi:10.1016/j.ejmp.2019.05.019.

**Artykuł 2** (IF: 2.685; MNiSW: 70.000) odpowiadający **ZS 2:**

Pawałowski B, Panek R, Szweda H, Piotrowski T.

*Combination of dual-energy computed tomography and iterative metal artefact reduction to increase general quality of imaging for radiotherapy patients with high dense materials. Phantom study.*

Phys Med. 2020; 77:92-99. doi:10.1016/j.ejmp.2020.08.009

**Artykuł 3** (IF: 4.379; MNiSW: 140.000) odpowiadający **ZS 3:**

Pawałowski B, Ryczkowski A, Panek R, Sobocka- Kurdyk U, Graczyk K, Piotrowski T.

*Accuracy of the doses computed by the Eclipse treatment planning system near and inside the metal elements.*

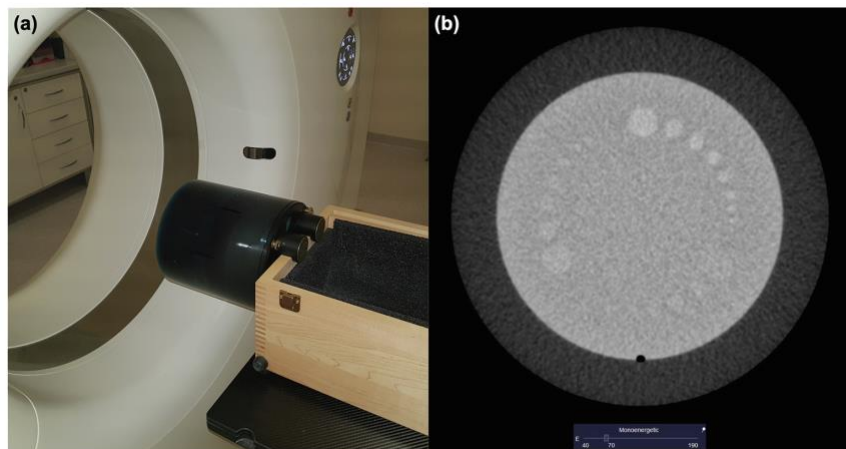
Sci Rep. 2022; 12(1):5974. doi: 10.1038/s41598-022-10072-8

### **3. Omówienie prac oraz uzyskanych wyników**

Wszystkie prace wchodzące w skład rozprawy doktorskiej są oryginalnymi pracami prezentującymi badania własne doktoranta. Pierwsza praca dotyczy analizy obrazów uzyskanych z tomografii spektralnej, druga weryfikuje wybrane metody redukcji artefaktów oraz ich kombinacje, trzecia kompleksowo analizuje wpływ użytych metod redukujących oraz poprawność obliczeń rozkładów dawek z wykorzystaniem dostępnych algorytmów obliczeniowych.

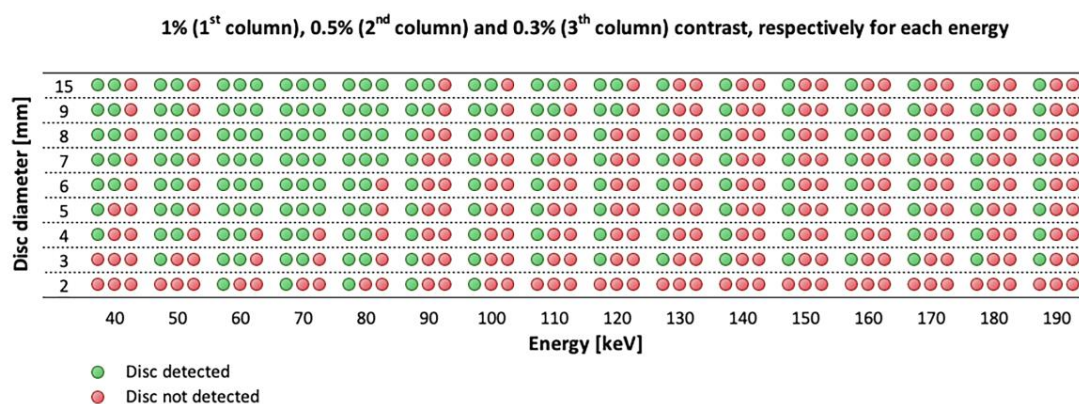
#### **3.1. Omówienie artykułu numer 1**

W artykule 1 - *Quality evaluation of monoenergetic images generated by dual-energy computed tomography for radiotherapy: a phantom study*, zweryfikowano jeden z trybów redukcji artefaktów tj. tomografię dwuenergetyczną. Celem pracy była ocena jakości obrazów monoenergetycznych generowanych poprzez wykorzystanie dwuenergetycznej tomografii komputerowej. W pracy zrekonstruowano serie obrazów monoenergetycznych (w zakresie od 40 keV do 190 keV co 10 keV) fantomu Catphan CTP 504 (The Phantom Laboratory, Salem, NY, USA). Fantom ten umożliwia ocenę jakości obrazowania tomograficznego. Analiza ilościowa uzyskanych obrazów fantomu, wykonana została z wykorzystaniem oprogramowania do automatycznej kontroli jakości. W pracy oceniono liniowość skali jednostek Hounsfielda dla obszarów z materiałami o różnej gęstości elektronowej, rozdzielcość nisko kontrastową, rozdzielcość wysokokontrastową, jednorodność, poziom szumu oraz stosunek sygnału do szumu. Obrazy wstępnie zweryfikowano także pod kątem ich potencjalnego wykorzystania podczas wyznaczania obszarów struktur anatomicznych w planowaniu radioterapii. Na podstawie oceny ilościowej wykazano, że najlepsze wyniki uzyskiwane były dla serii monoenergetycznych wygenerowanych dla 70 keV. Szczególną uwagę należy zwrócić na parametr progowego kontrastu, który oceniany jest na podstawie detekcji dysków o różnej średnicy oraz gęstości tj. różnicy gęstości o 1%, 0.5% oraz 0.3% względem tła.



Rysunek 1. (a) Układ pomiarowy. (b) Przekrój fantomu Catphan z modułem umożliwiającym ocenę progowego kontrastu (rys. z pracy nr 1).

Zauważać można, że największa liczba zdetektowanych dysków uzyskana została dla serii 60 oraz 70 keV co oznacza, że serie zrekonstruowane dla tych energii charakteryzują się najlepszą rozróżnialnością struktur o zbliżonej gęstości.



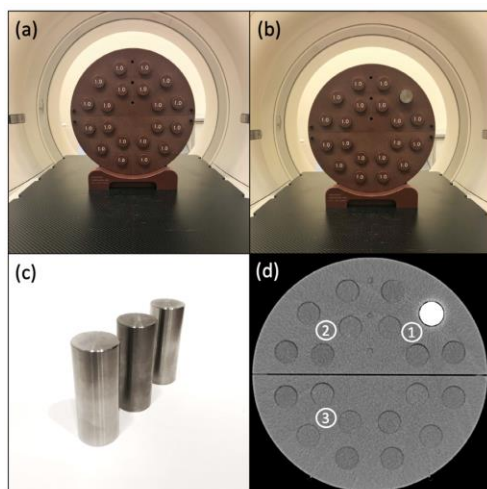
Rysunek 2. Graficzna interpretacja wyników uzyskanych podczas oceny kontrastu progowego. Liczba zdetektowanych dysków (kolor zielony) o różnej średnicy i różnych gęstościach (rys. z pracy nr 1).

Również parametry takie jak szum oraz stosunek sygnału dla szumu, wykazały znaczą przewagę tych dwóch energii. Analizując kolejny parametr jakim była zależność wartości HU od gęstości elektronowej, zauważono znaczne różnice w wartościach HU pomiędzy seriami. W związku z tym kolejnym wnioskiem wynikającym z pracy jest konieczność stosowania różnych krzywych kalibracyjnych, umożliwiających konwersję skali HU do wartości gęstości elektronowych, celem obliczenia dawki w strukturach anatomicznych. Zatem, w przypadku chęci wykorzystania skanów podczas planowania leczenia radioterapii, należy wyznaczyć krzywe kalibracyjne dedykowane do każdej z energii. W dalszej części pracy zrekonstruowano serie obrazów monoenergetycznych dla pacjenta

leczonego radioterapeutycznie, u którego badanie wykonano w trybie tomografii dwuenergetycznej. Na podstawie analizy przeprowadzonej przez lekarza radioterapeutę stwierdzono, że najbardziej użyteczne z punktu widzenia klinicznego były obrazy wygenerowane dla 70 keV, które charakteryzowały się najlepszą rozróżnialnością struktur. Należy jednak zauważyć, że ocena wykonana została tylko przez jednego lekarza i ograniczona była tylko do jednego pacjenta. Na podstawie analizy przygotowanego planu leczenia zauważono, że różnice w obliczonej dawce, wynikające z zastosowania tylko jednej krzywej konwersji (umożliwiającej zmianę jednostek HU na gęstości elektronowe), która rutynowo wyznaczona jest dla 120 keV. Świadczy to o konieczności wyznaczenia dedykowanych krzywych konwersji w przypadku obliczeń dla skanów wykonanych dla różnych energii.

### 3.2.Omówienie artykułu numer 2

W drugim artykule - *Combination of dual-energy computed tomography and iterative metal artefact reduction to increase general quality of imaging for radiotherapy patients with high dense materials. Phantom study*, weryfikowano i porównywano wybrane metody redukcji artefaktów oraz ich kombinacje. W pracy wykorzystano fantom Virtual Water phantom (Gammex RMI, Middleton, WI, USA) który został zeskanowany na tomografie komputerowym (Siemens Medical Solution, Erlangen, Niemcy) w trybach: (a) standardowej tomografii komputerowej, (b) tomografii połączonej z algorytmem redukującym metalowe artefakty (iMAR), (c) tomografii dwuenergetycznej oraz (d) tomografii dwuenergetycznej połączonej z algorytmem iMAR.



Rysunek 3. (a) Virtual Water Phantom. (b) Virtual Water Phantom z metalowym insertem. (c) Metalowe inserty. (d) Obszary, w których dokonywana była analiza. (rys. z pracy nr 2).

Budowa fantomu umożliwiała umiejscowienie w nim metalowych walców wykonanych z tytanu oraz dwóch typów stali będących stopami pierwiastków zbliżonymi do składu endoprotez. Analiza obrazów polegała na ocenie w trzech wybranych obszarach zmian wartości HU oraz odchylnia standardowego w stosunku do obrazu bez metalowych elementów. Dotychczasowe prace naukowe wskazywały na brak korzyści podczas łączenia obu metod redukujących artefakty tj. monoenergetycznych skanów z zakresu 120 - 140 keV z algorytmem iMAR. Jednakże bazując na publikacji numer 1 postanowiono zweryfikować także kombinacje algorytmu z monoenergetyczną serią skanów dla 70 keV. Wśród ocenianych serii pomiarowych, zgodnie z oczekiwaniemi, najgorsze wyniki obserwowane były dla rekonstrukcji niewykorzystujących algorytmu redukującego artefakty. Uzyskane wyniki podzielić można na najlepsze pod kątem precyzji odwzorowania metalowego elementu (efekt lokalny) oraz ze względu na poprawę jakości całego obrazu tomograficznego (efekt globalny). Analiza ilościowa wykazała znaczącą redukcję absolutnej różnicy jednostek HU pomiędzy obrazem referencyjnym, a obrazami zawierającymi metalowe elementy przy zastosowaniu algorytmu iMAR. Dla drugiego analizowanego parametru jakim było odchylenie standardowe wartości HU, najmniejsze wartości świadczące o najlepiej odtworzonym obrazie zaobserwowane zostały dla kombinacji skanów monoenergetycznych dla 70 keV z algorymem iMAR. Celem quasi klinicznej weryfikacji wyników uzyskanych w fantomie Virtual Water, przygotowano antropomorficzny fantom obszaru miednicy zawierający kości miednicy, kość udową, endoprotezę oraz struktury imitujące pęcherz, odbytnicę i prostatę. Fantom został zeskanowany na tomografie komputerowym z identycznymi parametrami jak pierwszy fantom poddawany ocenie ilościowej. Analiza jakościowa przeprowadzona została przez specjalistów fizyki medycznej, którzy ocenili, że dla serii pomiarowych wykorzystujących tylko tomografię dwuenergetyczną najlepsze jakościowo obrazy uzyskiwane były dla serii wygenerowanych dla 130 keV. Z kolei, w przypadku zastosowania algorytmu redukującego artefakty (iMAR), za najlepsze jakościowo wskazywano rekonstrukcje dla 70 keV oraz 130 keV. Dla rekonstrukcji 130 keV z iMAR zaobserwowano najlepszą redukcję artefaktów w okolicy metalowego elementu oraz jego najlepsze odwzorowanie (efekt lokalny). Seria skanów monoenergetycznych 70 keV z iMAR, która zdobyła największą liczbę punktów, wskazywana była przez fizyków medycznych jako całkowicie najlepsza oraz o wizualnie najmniejszych zaburzeniach obrazu (efekt globalny).

### **3.3. Omówienie artykułu numer 3**

Ostatni z artykułów - *Accuracy of the doses computed by the Eclipse treatment planning system near and inside the metal elements*, w sposób kompleksowy weryfikował tryby redukcji artefaktów oraz dokładności obliczeń dawek w zależności od wybranych metod rekonstrukcji obrazu i wybranych algorytmów obliczeniowych. W ramach pracy przygotowany został fantom wodny z wydrukowanym w technologii 3D uchwytem, umożliwiającym umiejscowienie filmu radiochromowego pionowo wzduż osi wiązki oraz utrzymanie przeciętego na pół, metalowego elementu. W porównaniu do prac 1 i 2, badania zostały rozszerzone o dodatkowy metal jakim był wolfram. Fantom został zeskanowany na tomografie komputerowym w warunkach identycznych jak w artykule numer 2, tj.: standardowe CT, standardowe CT z iMAR, DECT 70 keV, DECT 130 keV oraz kombinacja DECT z iMAR. Przed przystąpieniem do obliczeń, bazując na wnioskach z artykułu numer 1, przygotowano dla każdego z obrazowanych trybów dedykowane krzywe kalibracyjne umożliwiające konwersję wartości HU do gęstości elektronowej lub fizycznej. Dodatkowo celem uzyskania danych referencyjnych, które umożliwiły weryfikację obliczeń, wykonane zostały symulacje Monte Carlo. Model medycznego akceleratora liniowego przygotowany został z wykorzystaniem danych dostarczanych przez producenta aparatu. Należy wspomnieć, że obliczenia z wykorzystaniem metod Monte Carlo, ze względu na precyzyję odwzorowywania oddziaływań fizycznych są obecnie złotym standardem. Symulacje takie dzięki uwzględnianiu wszystkich istotnych zjawisk fizycznych, powstających podczas oddziaływania promieniowania z materią, pozwalają na uzyskiwanie zgodnych z rzeczywistością rozkładów dawek. Kolejnym krokiem była walidacja symulacji Monte Carlo z wykorzystaniem filmu radiochromowego EBT 3 (Ashland Inc. Wilmington, Delaware, USA). Przed przystąpieniem do napromieniania filmów wykonano krzywą kalibracyjną umożliwiającą konwersję gęstości optycznej do dawki. Zaobserwowana zwiększona wartość dawki od promieniowania wstecznie rozproszonego wymusiła rozszerzenie przygotowanej krzywej kalibracyjnej o 80 punktów procentowych dawki na głębokości dawki maksymalnej. Tak przygotowany układ wskazał rozbieżności pomiędzy symulacjami a pomiarem. Podczas analizy zauważono, znaczny wzrost dawki w obszarze filmu, co świadczyć może o perturbacji wiązki, dlatego w kolejnym kroku przygotowano symulacje uwzględniające obecność filmu. Dopiero symulacje uwzględniające film umożliwiły walidację kodu Monte Carlo. Wysokie wyniki

współczynnika korelacji Pearsona  $R \geq 0.998$ , potwierdzają zgodność symulacji z pomiarem. Wobec tego posłużyły one do przygotowania referencyjnych procentowych dawek głębokościowych. Następnym krokiem było zaprojektowanie obliczeń z wykorzystaniem algorytmów zaimplementowanych w systemie Aria. W pracy porównano dwa algorytmy pracujące w różnych trybach:

- AAA (*Analytical Anisotropic Algorithm*), z uwzględnieniem wartości HU metalowego elementu zrekonstruowanego przez tomograf,
- AAA, z uwzględnieniem przypisanej wartości HU dla całego metalowego elementu będącą wartością średnią HU z elementu,
- Acuros XB, obliczający dawkę bezpośrednio w ośrodku i raportującym dawkę w trybie *dose to medium*,
- Acuros XB, obliczający dawkę bezpośrednią w ośrodku i raportującym dawkę w trybie *dose to water*.

Wszystkie z wykorzystanych algorytmów posiadają pewne ograniczenia. Pierwszy z nich (AAA) umożliwia względnie szybką kalkulację rozkładów dawek, jednakże obliczenia dla obszarów, gdzie następuje znaczna zmiana gęstości (przejście ze struktur miękkich do płuca lub kości) zachodzi niedoszacowanie wartości dawki. Błąd ten ze względu na zdeponowanie niewłaściwej wartości dawki w obszarze tarczowym niekorzystnie wpływa na efekt terapeutyczny. Drugi z algorytmów (Acuros XB) jest algorymem klasy Monte Carlo. Obliczenia dawek wykonane tym algorymem w warunkach standardowych (tj. bez elementów metalowych) charakteryzują się wysoką zgodnością z pomiarami dawek zdeponowanych. Algorytm rozwiązuje liniowe równanie transportu Boltzmana fluencji elektronów w ośrodku z wykorzystaniem właściwych dla materiału zdolności hamowania (*stopping powers*). Dwa sposoby raportowania dawki realizowane są na etapie przetwarzania końcowego, kiedy fluencja energii będąca wynikiem obliczeń transportu mnożona jest przez funkcje odpowiedzi w dowolnym medium. Ograniczeniem tego algorytmu jest konieczność przypisywania konkretnego materiału do struktury o wysokiej gęstości z niemodyfikowej biblioteki.

Obliczenia przeprowadzono dla trzech metali tytanu, stali (alloy 600) oraz wolframu. Wyboru wolframu dokonano ze względu na jego bardzo dużą gęstość oraz fakt, że w bibliotece materiałów znajdowało się złoto o zbliżonej gęstości co umożliwiło przypisanie go do struktury. Następnie na wszystkich uzyskanych skanach tomograficznych z wykorzystaniem różnych metod redukujących artefakty przeprowadzono obliczenia rozkładów dawek z wykorzystaniem dostępnych

algorytmów. Analiza wyników wskazała bardzo dobrą zgodność algorytmu Acuros XB w trybie pracy *dose to medium*. Algorytm jako jedyny właściwie oblicza rozkład dawki z uwzględnieniem fenomenu fizycznego zachodzącego w miejscu łączenia metalowego elementu z wodą (lub tkanką pacjenta), polegającym na wygenerowaniu promieniowania wstecznie rozproszonego. Jak wspomniano pewnym ograniczeniem algorytmu jest jednak niemodyfikowalna biblioteka materiałów, zatem obliczenia dla alloy 600 oraz wolframu zostały zrealizowane dla predefiniowanej stali oraz złota. Obliczenia te pokazują pewne różnice wynikające ze wskazania materiałów zbliżonych, a nie wprost tych, które były użyte w eksperymencie. W przypadku drugiego trybu pracy algorytmu Acuros XB, czyli *dose to water* zaobserwowano znaczne przeszacowywanie dawki w metalu, jednakże obliczenia realizowane w wodzie są poprawne i zgodne z symulacjami. Drugi z algorytmów, czyli AAA, ze względu na wykonywane skalowanie dawki polegające na obliczaniu dawki w wodzie, a następnie z wykorzystaniem gęstości elektronowej skalowaniu dawki w danym punkcie, uniemożliwia uwzględnienie promieniowania wstecznie rozproszonego. Na podstawie analizowanych danych zauważono, że dla algorytmu AAA, przypisanie do całej struktury wartości HU wynikającej z tomografii komputerowej poprawia obliczenia za metalowym wkładem. Ostatnim wnioskiem płynącym z pracy była informacja, że różne tryby redukcji artefaktów nie wskazują istotnych statystycznie różnic pod kątem kalkulacji dawki, warunkiem jest jednak zastosowanie dedykowanej krzywej kalibracyjnej. W związku z powyższym wybór rekonstrukcji przez lekarza nie ma istotnego wpływu na obliczenia.

#### **4. Podsumowanie**

Przedłożona rozprawa doktorska poddała ocenie wpływ materiałów nieorganicznych o różnych gęstościach na obrazowanie medyczne oraz poprawność obliczeń rozkładów dawki w procesie radioterapii. W oparciu o przedstawiony cykl publikacji wyciągnięto następujące wnioski:

**Artykuł 1:** W oparciu o analizę danych ilościowych wykazano, że dla serii obrazów pseudo monoenergetycznych najlepsza jakościowo jest seria zrekonstruowana dla 70 keV. Również z punktu widzenia klinicznego seria wygenerowana dla 70 keV została oceniona jako najlepsza (subiektywna ocena lekarska).

**Artykuł 2:** W oparciu o analizę ilościową danych wykazano, że zastosowanie algorytmu iMAR znacznie zredukowało absolutną różnicę jednostek HU pomiędzy obrazem referencyjnym, a obrazem po redukcji artefaktów. Na podstawie analizy odchylenia standardowego wartości HU wykazano, że najmniejsze wartości świadczące o najlepiej odtworzonym obrazie zaobserwowane zostały dla kombinacji skanów monoenergetycznych dla 70 keV z algorytmem iMAR.

**Artykuł 3:** Na podstawie analizy danych wykazano, że algorytmem najlepiej obliczającym rozkłady dawek w obecności metali jest Auros XB – *dose to medium*, który uwzględnia promieniowanie wsteczne rozproszone, pewnym ograniczeniem jest niemodyfikowalna biblioteka materiałów, tryb pracy *dose to water* przeszacowuje dawkę w metalu, aczkolwiek poprawnie realizuje obliczenia w wodzie. Algorytm AAA ze względu na skalowanie dawki i obliczenia gęstości elektronowej, oblicza dawkę lokalnie i nie uwzględnia promieniowania wstecznie rozproszonego, jednakże przypisanie do całej struktury wartości HU wynikającej z tomografii komputerowej poprawia obliczenia za metalowym wkładem. Ponadto, po zweryfikowaniu różnych trybów redukcji artefaktów nie wykazano istotnych statystycznie różnic pod kątem kalkulacji dawki, pod warunkiem zastosowania dedykowanej krzywej kalibracyjnej - zatem lekarz ma możliwość wyboru trybu obrazowania najlepszego według osobistej oceny.

Na podstawie prac w oparciu, o które zbudowana została rozprawa doktorska można stwierdzić, że najlepszą strategią przygotowania pacjentów do radioterapii jest wykonanie dwuenergetycznej tomografii komputerowej z wykorzystaniem algorytmu

iMAR oraz wygenerowanie serii pseudo monoenergetycznej dla 70 keV. Kombinacja tych metod umożliwia uzyskanie najlepszej jakości obrazów tomograficznych na których znajdują się elementy metalowe. Następnie celem przygotowania planu leczenia, który realizowany będzie na akceleratorze medycznym należy zastosować algorytm klasy Monte Carlo np. Auros w trybie *dose to medium*, co umożliwia uzyskanie najlepszych zgodności pomiędzy obliczonym i rzeczywistym rozkładem dawek.

## 5. Piśmiennictwo

1. Grubbe EH. *Priority in the therapeutic use of X-rays.* Radiology, 1933;21:156–162. <https://doi.org/10.1148/21.2.156>.
2. Hounsfield, G. N. (1977). "The E.M.I. Scanner". *Proceedings of the Royal Society of London. Series B, Biological Sciences.* 195 (1119): 281–289. doi:10.1098/rspb.1977.0008.
3. Barrett JF, Keat N. *Artifacts in CT: recognition and avoidance.* Radiographics 2004;24(6):1679–91. doi:10.1148/rg.246045065.
4. Bongers MN, Schabel C, Thomas C, Raupach R, Notohamiprodjo M, Nikolaou K, et al. *Comparison and combination of dual-energy- and iterative-based metal artefact reduction on hip prosthesis and dental implants.* PLoS ONE 2015;10(11):e0143584 doi:10.1371/journal.pone.0143584.
5. Lee MJ, Kim S, Lee SA, Song HT, Huh YM, Kim DH, et al. *Overcoming artifacts from metallic orthopedic implants at high-field-strength MR imaging and multi-detector CT.* Radiographics 2007;27(3):791–803. doi:10.1148/rg.273065087.
6. Spadea MF, Verburg JM, Baroni G, Seco J. *The impact of low-Z and high-Z metal implants in IMRT: A Monte Carlo study of dose inaccuracies in commercial dose algorithms.* Med Phys. 2014; 41(1):011702. doi:10.1118/1.4829505
7. Ferguson RJ, Palmer AJ, Taylor A, Porter ML, Malchau H, Glyn-Jones S. *Hip replacement.* Lancet. 2018 Nov 3;392(10158):1662-1671. doi: 10.1016/S0140-6736(18)31777-X.
8. McCollough CH, Leng S, Yu L, Fletcher JG. *Dual- and Multi-Energy CT: Principles, Technical Approaches, and Clinical Applications.* Radiology. 2015 Sep;276(3):637-53. doi: 10.1148/radiol.2015142631. PMID: 26302388; PMCID: PMC4557396.
9. Ojala J, Kapanen M, Sipilä P, Hyödynmaa S, Pitkänen M. *The accuracy of Acuros XB algorithm for radiation beams traversing a metallic hip implant - comparison with measurements and Monte Carlo calculations.* J Appl Clin Med Phys. 2014; 15(5):4912. doi: 10.1120/jacmp.v15i5.4912.
10. Lloyd SA, Ansbacher W. *Evaluation of an analytic linear Boltzmann transport equation solver for high-density inhomogeneities.* Med Phys. 2013; 40(1):011707. doi:10.1118/1.4769419.

11. Kry SF, Lye J, Clark CH, Andratschke N, Dimitriadis A, Followill D, et al. *Report dose-to-medium in clinical trials where available; a consensus from the Global Harmonisation Group to maximize consistency.* Radiother Oncol. 2021; 159:106-111. doi: 10.1016/j.radonc.2021.03.006.
12. Failla GA, Wareing T, Archambault Y, Thompson S. *Acuros XB advanced dose calculation for the Eclipse treatment planning system.* Palo Alto, CA: Varian Medical Systems; 2010.
13. Yan C, Combine AG, Bednarz G, Lalonde RJ, Hu B, Dickens K, et al. *Clinical implementation and evaluation of the Acuros dose calculation algorithm.* J Appl Clin Med Phys. 2017; 18(5):195-209. doi:10.1002/acm2.12149.
14. Paulu, D. and Alaei, P, *Evaluation of dose calculation accuracy of treatment planning systems at hip prosthesis interfaces.* J Appl Clin Med Phys. 2017; 18: 9-15. doi:10.1002/acm2.12060



## Original paper

## Quality evaluation of monoenergetic images generated by dual-energy computed tomography for radiotherapy: A phantom study

Bartosz Pawałowski<sup>a,b</sup>, Hubert Szweda<sup>a</sup>, Alina Dudkowiak<sup>b</sup>, Tomasz Piotrowski<sup>a,c,\*</sup><sup>a</sup> Department of Medical Physics, Greater Poland Cancer Centre, Poznań, Poland<sup>b</sup> Department of Technical Physics, Poznań University of Technology, Poznań, Poland<sup>c</sup> Department of Electroradiology, Poznań University of Medical Sciences, Poznań, Poland

## ARTICLE INFO

**Keywords:**  
 Spectral CT  
 Monoenergetic CT  
 Dual energy  
 Quality of CT images

## ABSTRACT

**Purpose:** Quantification analysis for monoenergetic computed tomography (CT) images obtained from dual-energy CT scanning was performed in the light of their potential use for structures delineation during radiotherapy.

**Methods:** Parameters that describe the quality of the images are: linearity, low and high contrast resolution, uniformity, noise and signal to noise ratio (SNR). To evaluate these parameters, a Catphan phantom was scanned using a dual-energy mode at Somatom Definition AS. Based on the polyenergetic CT images, sixteen monoenergetic series (ranged from 40 keV to 190 keV) were created by CT scanner software and automatically analyzed using Artiscan software.

**Results:** Analysis of linearity shows that a potential use of any monoenergetic images in radiotherapy planning requires that individual calibration curves are implemented for each of them. While the results of the high contrast resolution analysis were comparable for each energy (5 lp/cm), the results of the analyses for uniformity, low contrast resolution, noise and SNR allowed us to select the best imaging energies. The highest relative uniformity was detected for images reconstructed for energies of 60 keV and 70 keV (98.54% and 98.61%). Similar results were observed for low contrast resolution, where the largest number of disks was detected for these energies, and the noise values (0.42% for 60 keV, 0.44% for 70 keV). The best SNR was observed for images reconstructed for energy of 60 keV.

**Conclusions:** Taking into account these results, the energy of 70 keV was selected as potentially the best for reconstruction of monoenergetic images used for structures delineation during radiotherapy.

## 1. Introduction

Limited differentiation of anatomical structures on computed tomographic (CT) images significantly affects the precision of the determination of the target volumes and organs at risk during the segmentation process which is one of the crucial parts of the treatment planning procedure performed before radiation therapy [1,2]. In the case of dynamic techniques of radiation therapy (e.g. intensity modulated radiation therapy or volumetric modulated arc therapy), inaccuracy of segmentation affects directly the optimization of dose distribution during the treatment plan preparation and, eventually, the accuracy of dose deposition during the treatment. The reason for these difficulties is that the CT-numbers measured for a specific voxel (representing an elemental part of the tissue) is related to the linear attenuation coefficient  $\mu(E)$  which is not unique for any given tissue/

material, but is a function of the material composition, the photon energies interacting with the material, and the mass density of the material [1]. Assuming the use of monoenergetic x-rays, at approximately 120 keV, the same linear attenuation coefficients can be measured for example, for calcified plaques and iodine-containing lymph nodes [1]. Data acquired at approximately 70 keV would allow the differentiation of the two materials.

This was a prerequisite for the development of new computed tomography technologies, which, apart from imaging capabilities using a polyenergetic spectrum of radiation with defined nominal energy, would enable to obtain a few anatomically identical sets of images differentiated by the energy of radiation during one imaging session on CT in such a way that each set of images is related to specific monoenergetic radiation (monoenergetic CT). There are several technical solutions to generate monoenergetic CT images. First group of them is

\* Corresponding author at: Department of Medical Physics, Greater Poland Cancer Centre, Garbary 15, 61-866 Poznań, Poland.  
 E-mail address: [tomasz.piotrowski@me.com](mailto:tomasz.piotrowski@me.com) (T. Piotrowski).

based on using two or more polyenergetic spectra with different nominal energies (e.g. 80 keV and 140 keV) and is realized, respectively, by: (i) a system of two x-ray tubes [3–5], (ii) technology of fast switching of scanning energy between possible highest and lowest nominal energy [6–8], or (iii) double helix technique, where the object is scanned twice (each time using a different nominal energy) [9,10]. The second group of technical solutions applies to the construction of CT detectors, e.g. (i) two-layer detectors, where the surface layer collects a signal with lower energies and the layer located deeper collects a signal with higher energies [11–14], or (ii) technology based on counting single photons for which the detector is a semiconductor diode that allows to detect single photons and correlate the strength of the detected signal with energy [15–18].

Use of a different set of monoenergetic images based on the spectral analysis allows to resolve problems with non-differentiated structures for conventional imaging (polyenergetic CT with specified nominal energy of radiation). When the anatomical data are non-contrasted and free of high-density material, there is a possibility to select the monoenergetic set of images that, based on the parameters characterizing the image quality, are most appropriate for treatment plan preparation.

## 2. Material and methods

The aim of this study was to evaluate the monoenergetic CT images collected by the dual-energy mode using the double helix technique on the Somatom Definition AS machine (Siemens Medical Solutions, Erlangen, Germany). The evaluation was performed on the images gathered for the Catphan 504 (CTP504) phantom (The Phantom Laboratory, Salem, NY, USA). The CTP504 was placed on the CT table in such a way that only the basis of the phantom was on the table while the active (imaged) part of the phantom was outside the table during scanning (Fig. 1a). The slice thickness of 3 mm, 1.2 value of the pitch and 80 keV and 140 keV energies for the first and the other helix, respectively, were used during imaging of the phantom. The CT dose volume indices (CTDI<sub>vol</sub>) and dose length products (DLP) were, respectively: 16.8 mGy and 369.6 mGy\*cm for the first helix (80 keV); and 18.4 mGy and 404.8 mGy\*cm for the other helix (140 keV). Based on the obtained set of dual-energy CT images, the reconstructions of the sixteen monoenergetic CT sets of images were performed with energies ranging from 40 keV to 190 keV with a step of 10 keV. Fig. 1b shows the operation window available in the reconstruction module of software installed on an operator station of the Somatom Definition AS machine, where a monoenergetic CT set of images is created from the dual-energy

CT set of images. The energy selection slider located at the bottom of the window on Fig. 1b allows to extract the monoenergetic data ranged from 40 keV to 140 keV from data gathered during scanning and extrapolate these data to the monoenergetic data for energies from 141 keV up to 190 keV.

All quantitative analyses of the quality of images included in this study were performed in the Artisan software (AQUILAB, Loos les Lille, France) enabling automatic analysis of the CT images gathered for the CTP504 phantom. The CTP504 is 20 cm in length and includes four modules dedicated for measurements of the parameters of CT images describing their quality [19,20]. For each monoenergetic CT set of images, the following parameters were evaluated: (i) linearity of the CT-numbers for different mass densities displayed on different monoenergetic CT sets of images (imaging data collected in CTP401 module), (ii) low contrast resolution (imaging data collected in CTP515 module), (iii) uniformity, noise and signal to noise ratio (imaging data collected in CTP486 module), and (iv) high contrast resolution (imaging data collected in CTP528 module).

According to the Artisan brochure describing details of parameters [21] the low contrast resolution, uniformity, noise and signal to noise ratio were expressed, respectively, as:

$$C_o = \frac{S_o - S_F}{S_F} \times 100 \quad (1)$$

where  $C_o$  is the low contrast resolution,  $S_o$  is the mean signal value collected on the object and  $S_F$  is the mean signal value of the signal from the background around the object.

$$Uni = \frac{NdG_{max} - NdG_{min}}{NdG_{max} + NdG_{min}} \quad (2)$$

where  $Uni$  is the uniformity, and  $NdG_{max}$  and  $NdG_{min}$  are, respectively, the maximum and minimum gray levels measured in the region of interest.

$$N = \frac{\sigma_{NH}}{HU_{Water} - HU_{Air}} \times 100\% \quad (3)$$

where  $N$  is the noise level,  $\sigma_{NH}$  is the standard deviation of the Hounsfield units in the region of interest, and  $HU_{Water}$  and  $HU_{Air}$  are, respectively, the Hounsfield units for water and for air.

$$SNR = \sqrt{2} \frac{GL}{\sigma_{Dif}} \quad (4)$$

where  $SNR$  is the signal to noise ratio,  $GL$  is the mean value of gray

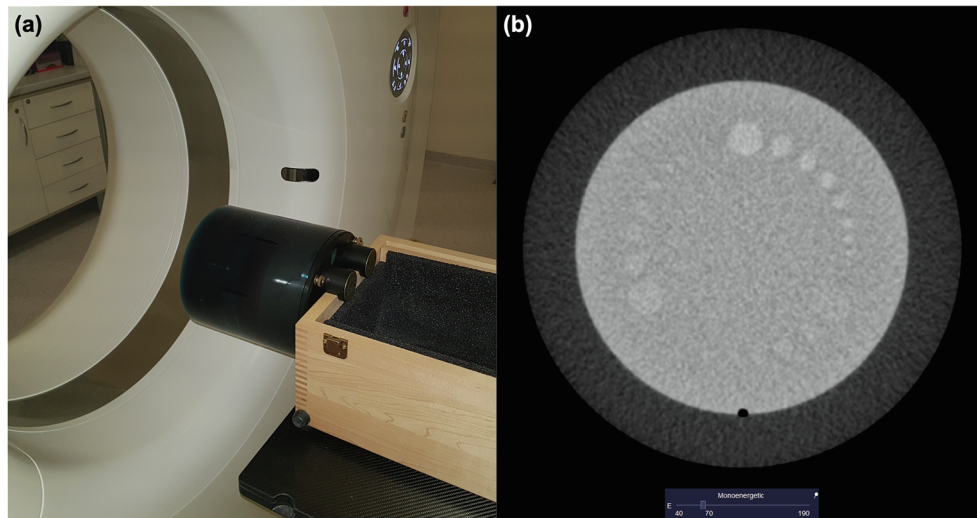


**Fig. 1.** The Catphan 504 – phantom used in the study. Figures show: (a) position of the phantom during data gathering and (b) image of CTP515 module of the phantom with energy selector at the bottom of the window.

levels in the region of interest and  $\sigma_{dif}$  is the standard deviation of the gray level difference in the region of interest.

The high contrast resolution was calculated from the ratios for the 21 test patterns of the insert in the phantom (CTP528 module). The power spectral density ratio curve was plotted according to the all test patterns, expressed as pairs of lines per unit of measure. This curve tends towards 100% for the largest pattern and towards 0% when the imaging system can no longer distinguish between them. The first minimum of the curve gives the high contrast resolution. The power spectral density is defined as [21]:

$$PSDR_i = \frac{PSD_{acq}}{PSD_{rec}} \times 100 \quad (5)$$

where  $PSDR_i$  is the power spectral density  $PSD$  for the  $i$ -th pattern  $R_i$ , and  $PSD_{rec}$  and  $PSD_{acq}$  are the power spectral densities for the reconstructed theoretical profile and for the acquired profile, respectively.

To analyze the linearity, absolute differences (AD) [HU] and absolute relative differences (ARD) [%] between CT-numbers were measured on monoenergetic and polyenergetic (dual-energy mode) images. The AD and ARD were expressed as follows:

$$AD_{MEj,D_i} = |CTnumber_{MEj,D_i} - CTnumber_{DE,D_i}| \quad (6)$$

$$ARD_{MEj,D_i} = \left| \frac{CTnumber_{MEj,D_i} - CTnumber_{DE,D_i}}{CTnumber_{DE,D_i}} \right| \cdot 100\% \quad (7)$$

where  $CTnumber_{MEj,D_i}$  is an average value of Hounsfield units detected in pixels contained in the  $i$ -th disc ( $D_i$ ) at the monoenergetic CT set of images reconstructed for the  $j$ -th energy ( $ME_j$ ),  $CTnumber_{DE,D_i}$  is an average value of Hounsfield units detected in pixels contained in the  $i$ -th disc ( $D_i$ ) at the polyenergetic CT set of images obtained from imaging based on the dual energy mode ( $DE$ ).

### 3. Results

Based on the linearity analysis, the absolute differences (AD) and absolute relative differences (ARD) between the CT-numbers from

monoenergetic and polyenergetic (dual energy mode) CT images were computed. Fig. 2 shows the relations of these values in the light of different relative electron densities displayed on different monoenergetic CT sets of images. The relative electron densities ranged from low values (e.g. 0.001 e/cm<sup>3</sup> for air) through the values comparable to electron densities for water (e.g. 0.998 e/cm<sup>3</sup> for polystyrene) to high values (e.g. 1.868 e/cm<sup>3</sup> for teflon). Based on values of the AD (Fig. 2a) and ARD (Fig. 2b) parameters, the most consistent and the smallest values were observed for energy of 70 keV (1 HU and 0.1% for air, 2HU and 5.9% for polystyrene, and 3HU and 0.3% for teflon). The highest inconsistency was observed for energy of 40 keV: 2 HU and 0.2% for air, 111 HU and 302.1% for polystyrene, and 156 HU and 16.2% for teflon. While the ARD parameter is small for low (air) and high (teflon) relative electron densities, the values of ARD increase for relative electron densities near 1 e/cm<sup>3</sup>. For example, for CT images reconstructed for energy of 120 keV the ARD is: 0.4% for air (0.001 e/cm<sup>3</sup>), 91.3% for polystyrene (0.998 e/cm<sup>3</sup>) and 4.9% for Teflon (1.868 e/cm<sup>3</sup>).

Fig. 3 shows the results for low contrast resolution analysis performed in the CTP515 module of CTP504. The CTP515 module contains low contrast supra-slice discs with diameters ranging from 2 mm to 15 mm, and contrast levels of 0.3%, 0.5% and 1.0%. These discs are used to evaluate the ability to differentiate objects with slightly different densities. The first column of the graphical table in Fig. 3 represents the diameters of the discs. The analysis was performed for monoenergetic CT sets of images reconstructed for energies ranging from 40 keV to 190 keV (last row in Fig. 3). The results for contrast levels of 1.0%, 0.5% and 0.3% are presented in the first, second and third column, respectively, for each energy (Fig. 3). While the green dots in Fig. 3 represent the positive result of detection (disc is visible), the red dots mean that no disc was detected. The best results of low contrast resolution analysis were observed for energies of 70 keV and 60 keV. For both of these energies, all discs with contrast level of 1% were visible. For the contrast level of 0.5%, the disc with a diameter of 2 mm, and for the contrast level of 0.3%, discs with diameters of 2 mm, 3 mm and 4 mm were not detected for these energies. The worst results were observed for all energies higher than 120 keV. For these energies, only the discs with diameters higher than 2 mm verified on the contrast

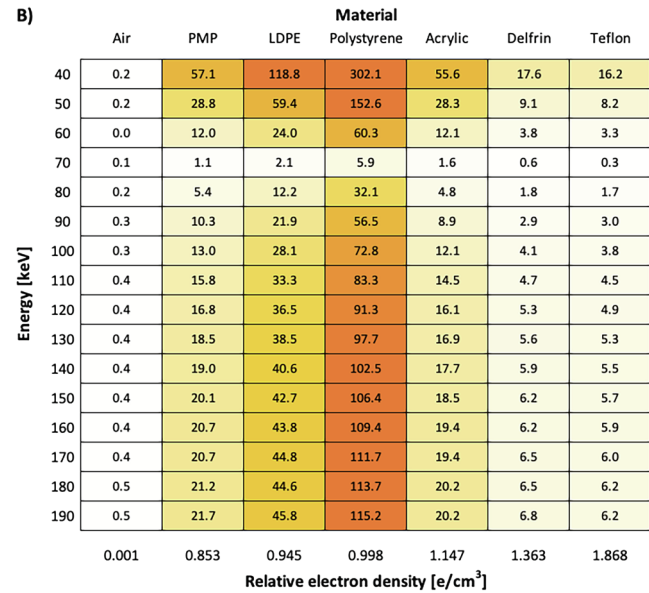
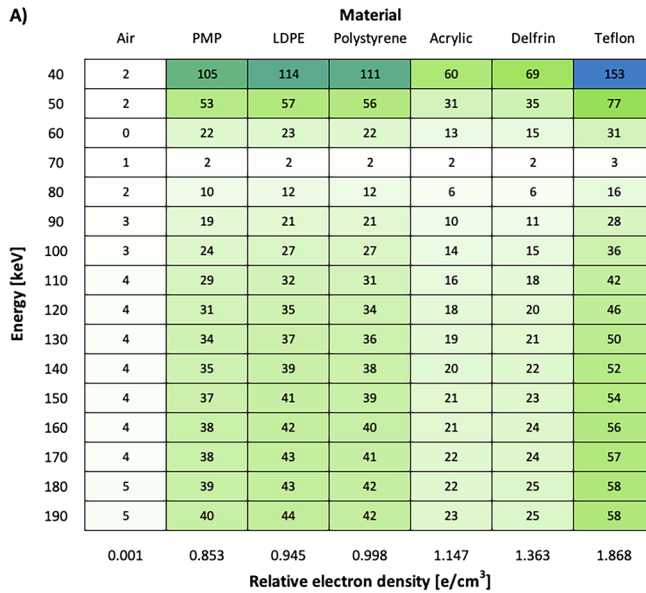
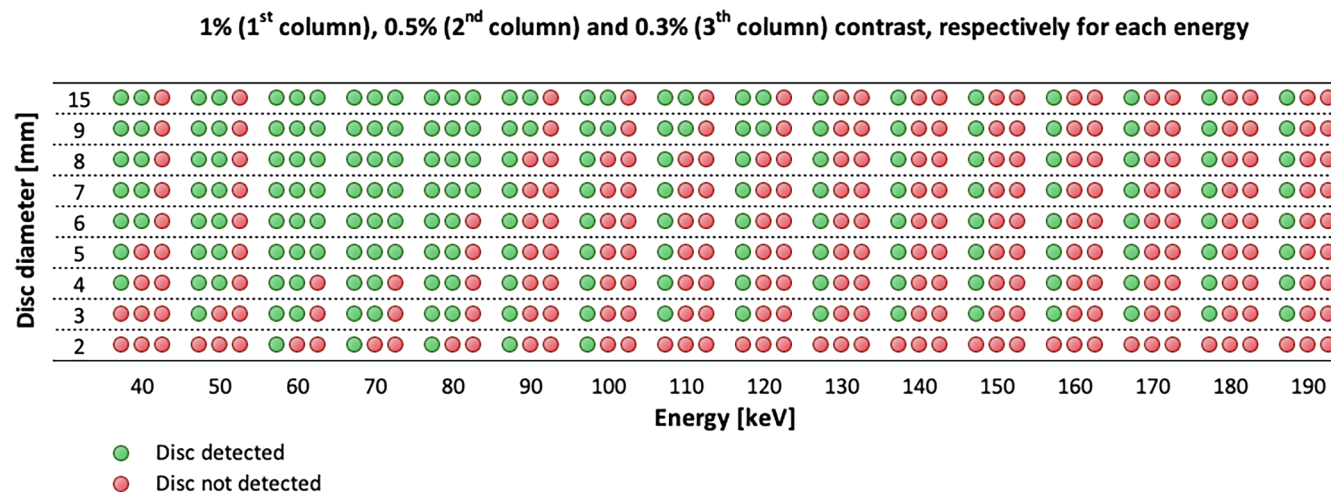


Fig. 2. The absolute differences (a) and the absolute relative differences (b) between the CT-numbers from monoenergetic and polyenergetic (dual energy mode) CT images and their relations to different relative electron densities and different monoenergetic CT sets of images.



**Fig. 3.** The results for low contrast resolution analysis performed in the CTP515 module of the Catphan 504 phantom. The green dots represent the positive result of detection, the red dots mean that no disc was detected. (For interpretation of the references to colour in this figure legend, the reader is referred to the web version of this article.)

**Table 1**

High contrast resolution, relative uniformity, noise and signal to noise ratio in relation to the energies of monoenergetic CT images.

| Energy [keV] | High Contrast Resolution [lp/cm] | Relative Uniformity [%] | Signal to Noise Ratio | Noise [%] |
|--------------|----------------------------------|-------------------------|-----------------------|-----------|
| 40           | 5.63                             | 92.42                   | 54.66                 | 2.21      |
| 50           | 5.74                             | 96.58                   | 129.00                | 0.98      |
| 60           | 5.79                             | 98.54                   | 300.00                | 0.42      |
| 70           | 5.82                             | 98.61                   | 254.90                | 0.44      |
| 80           | 5.85                             | 98.04                   | 175.81                | 0.63      |
| 90           | 5.86                             | 97.47                   | 142.45                | 0.78      |
| 100          | 5.88                             | 97.09                   | 125.67                | 0.88      |
| 110          | 5.88                             | 96.86                   | 115.72                | 0.96      |
| 120          | 5.88                             | 96.62                   | 110.01                | 1.01      |
| 130          | 5.89                             | 96.54                   | 105.51                | 1.06      |
| 140          | 5.89                             | 96.44                   | 103.20                | 1.09      |
| 150          | 5.90                             | 96.35                   | 100.35                | 1.12      |
| 160          | 5.90                             | 96.26                   | 98.74                 | 1.13      |
| 170          | 5.90                             | 96.24                   | 97.49                 | 1.15      |
| 180          | 5.90                             | 96.21                   | 96.51                 | 1.16      |
| 190          | 5.90                             | 96.17                   | 95.68                 | 1.17      |
| Dual-Energy* | 5.83                             | 98.66                   | 227.41                | 0.49      |

\*Images obtained from scanning with two polyenergetic beams with nominal energies of 80 keV and 140 keV (dual energy mode). Data from dual energy mode are the source for reconstruction of monoenergetic images.

level of 1% were detected.

The results of high contrast resolution as well as relative uniformity were presented in Table 1. While almost the whole table contains data for specified energy, the last row of Table 1 contains data for polyenergetic imaging (dual energy mode). Despite a difference between high contrast resolution measured at monoenergetic and polyenergetic CT sets of images, the results are comparable because, in fact, 5 lines pair per cm were detected for every energy.

The best relative uniformity for the monoenergetic CT sets of images was obtained for 70 keV energy (98.61%). The relative uniformity for images obtained from this energy correspond to the relative uniformity for the polyenergetic images (98.66%). For the rest of monoenergetic images, except the images obtained for the energy of 40 keV, the relative uniformity ranged from 96% to 98% and was slightly worse than for the polyenergetic images. The relative uniformity for 40 keV images was significantly worse than for polyenergetic images and was 92.42%.

In addition to the data of high contrast resolution and relative uniformity, Table 1 includes data of noise and signal to noise ratio (SNR) that were visualized in Fig. 4. Among all analyzed energies, the

best SNR and the lowest value of the noise were observed for images obtained for the energies of 60 keV and 70 keV.

Moreover, images obtained for these energies were characterised by better values of SNR and noise than the polyenergetic images. The noise and SNR were respectively: 0.42% and 300.00 for 60 keV, 0.44% and 254.90 for 70 keV and 0.49% and 227.41 for polyenergetic images.

#### 4. Discussion

In connection to the technical solutions of the CT scanner used in our hospital (Somatom Definition AS), the evaluation of the monoenergetic CT images was limited to the dual-energy mode realized by the double helix technique. The double helix technique at the Somatom Definition AS scanner consists of two successive spiral scans, where the first scanning uses the energy of 140 keV and the other, the energy of 80 keV. One of the potential limitations of this method is the time delay between the two helices that can lead to inaccurate imaging of tissues and organs susceptible to motion [1]. In our study, analysis was performed for data gathered from the static phantom. Therefore, the study is free of potential influence of inaccuracy caused by movement. Because our therapeutic line is based on Varian products, the CTP504 was the phantom that was used by us for data gathering [22]. To eliminate the potential influence of the CT table on the images, the CTP504 was placed on the CT table in such a way that the active (imaged) part of the phantom was outside the table during the scanning process (Fig. 1a). To reduce inaccurate image reconstruction at the edges of the active part CTP504 with a full length of 20 cm, a 1 cm margin was used from each side of the phantom. As a result, the scanned length was 22 cm. Therefore, total (for both helices) CTDI<sub>vol</sub> and DLP were 35.2 mGy and 774.4 mGy\*cm. In contrast to conventional scanning (e.g. when a polyenergetic spectrum of radiation with nominal energy of 120 keV is used), total CTDI<sub>vol</sub> for the dual energy mode available on our CT scanner is fixed and cannot be modified. This makes it impossible to reduce the dose during scanning. Nevertheless, the total CTDI<sub>vol</sub> for the dual energy mode is not dramatically higher than every CTDI<sub>vol</sub> obtained for conventional scanning. For example, in our hospital, for conventional scanning and routinely used protocols, such as protocols for the abdomen and head, the CTDI<sub>vol</sub> and DLP (for 22 cm) were 14.9 mGy and 327.8 mGy\*cm (for abdomen), and 59.4 mGy and 1306.8 mGy\*cm (for head). These values were obtained for the same conditions (pitch and slice thickness) as used for dual energy scanning.

The monoenergetic CT images collected by the dual-energy mode were evaluated in the light of parameters characterizing their quality. The quantification analysis of linearity, uniformity, noise and signal to

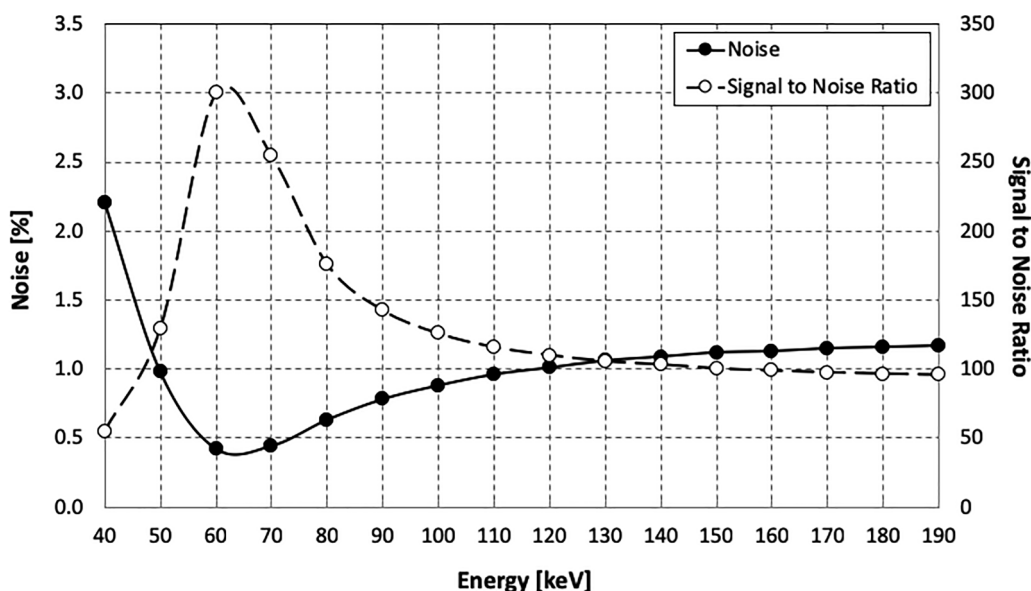


Fig. 4. Noise and signal to noise ratio in relation to the energies of monoenergetic CT images.

noise ratio, and low and high contrast resolution were performed by us with the Artisan software. The automation tools implemented in the Artisan software use well-known and widely accepted calculation formalizations. The Artisan automate manual and objective operations were performed by the investigator for the analysis of linearity, uniformity, noise and signal to noise ratio. The classical assessment of low contrast is based on measurements made by counting numbers of visible targets by the investigator. To maintain reproducibility, the measurements should be carried out by the same investigator and on the same monitor screen with the same viewing conditions (same window settings, same day, subdued ambient light). To minimize all possible factors influencing the results and subjective interpretation of the investigator, Artisan software performs these measurements automatically. As in low contrast measurements, the classical (visual) evaluation of high resolution is replaced by automated measuring. While automation reduces the impact of inter-observer effect on the obtained results, there is still a question of whether the detection made by the computer is compatible to an average detection performed by investigators in a classical way. Nevertheless, the concept of our study prevents us from addressing this problem because the analysis was based on the evaluation of the parameters computed always in the same way (by Artisan) between different monoenergetic CT images.

The results from the analysis of linearity (Fig. 2) clearly show that CT-numbers counted for different materials at monoenergetic images differ from one another and are different from CT-numbers counted on polyenergetic images. It means that a potential use of any monoenergetic images in radiation therapy planning, requires that individual calibration curves are implemented for each of them. While individual calibration curves require an absolute difference for evaluation (Fig. 2a), the absolute relative differences (Fig. 2b) show the strength of the absolute differences in the light of the HU ranges detected in structures with specified relative electron density and imaged by different energies. The lowest differences between monoenergetic and polyenergetic images were observed for the energy of 70 keV (Fig. 2). This is caused by the fact that the energy of 70 keV is a main component of the polyenergetic spectrum of radiation used during scanning by the dual energy mode. While the results of a high contrast resolution analysis were comparable for each energy (5 lp/cm), the results of analyses for relative uniformity, low contrast resolution, noise and SNR allowed us to select the best imaging energies. The highest relative uniformity was detected for images reconstructed for energy of 70 keV (98.61%).

The best results for low contrast resolution (Fig. 3) and the noise values (Table 1) were observed for energies of 70 keV and 60 keV. Images obtained for both of these energies were characterized by better signal to noise ratios than polyenergetic images (Fig. 4 and Table 1). All the results analyzed and discussed above were gathered in CTP504. Fig. 5 shows images of the head and neck anatomy gathered for monoenergetic (for energies of 50 keV, 70 keV, 120 keV) and mixed (polyenergetic) imaging.

Fig. 5 complement visually the data collected in Table 1. In conjunction to the limitations of the double helix technique, we decided to visualize the head and neck region characterized by relatively low organ flexibility during scanning.

Using one calibration curve (e.g. calibration curve for polyenergetic images) for different sets of monoenergetic images causes inaccuracies of dose calculation. It results directly from the differences in linearity between sets of monoenergetic images (Fig. 2) and their different relative uniformity (Table 1). Fig. 6 shows an example of differences between doses calculated on sets of images differing in energy (50 keV, 70 keV, 120 keV and polyenergetic images) while one calibration curve (for polyenergetic images) was applied. The treatment plans were prepared for Varian TrueBeam™ accelerator (Varian Medical Systems, Palo Alto, CA, USA) using the Eclipse™ treatment planning system ver. 13.6 (Varian Medical Systems, Palo Alto, CA, USA). The analytic anisotropic algorithm with the spatial resolution of 2.5 mm was used for computing dose to the irradiated region. The same simple geometry of the therapeutic beams (i.e. two lateral photon beams with 6 MeV energy, normalised in the same isocentre point) was used for each calculation. As can be seen in Fig. 6, the smallest inaccuracies in the calculation of the dose were observed for images obtained for the energy of 70 keV. This is due to the smallest differences of the linearity and relative uniformity between these images and the polyenergetic images. Nevertheless, it should be clearly noted that the usage of different sets of monoenergetic images during dose calculation induces the need of adding individual calibration curves for each set.

While the linearity and relative uniformity impact the accuracy of the dose calculation, the noise, SNR and low contrast resolution impact the clarity and detail of the images (Fig. 5) that can affect the accuracy of the contouring for specific parts of patient's anatomy. Fig. 7 shows the outlines of bones and the tongue prepared on four different sets of images, i.e. on three monoenergetic sets with energies of 50 keV, 70 keV and 120 keV, and on one set of polyenergetic images.

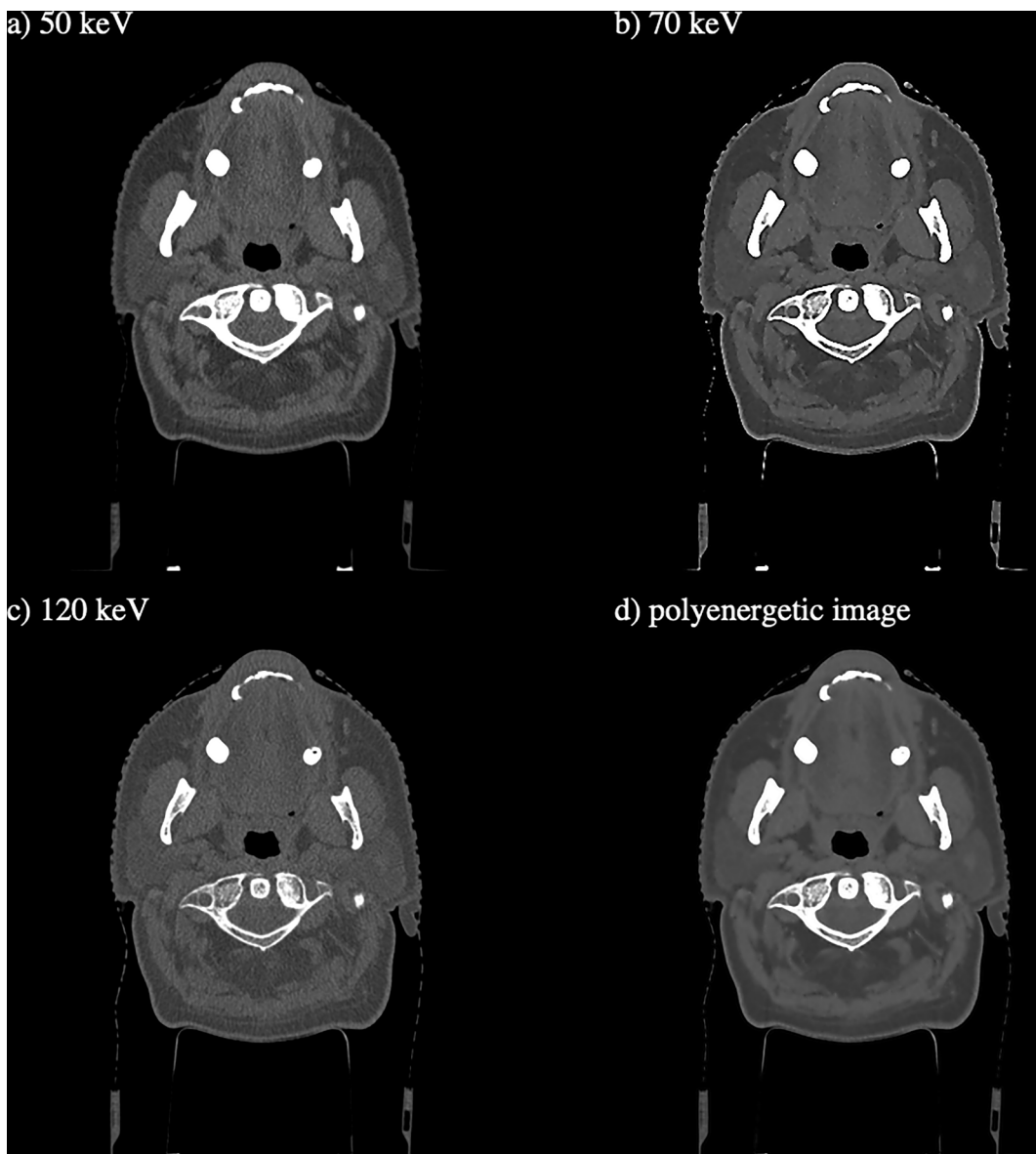


**Fig. 5.** Head and neck anatomy gathered for (a-c) monoenergetic imaging (respectively: a) 50 keV, b) 70 keV, c) 120 keV), and (d) mixed (polyenergetic) imaging. For each image the same displaying settings were used (window width: 1160 and level: 140).

The bones were outlined automatically, and the tongue was outlined manually by a well experienced radiation oncologist. 70 keV images were indicated by the radiation oncologist as the clearest and most useful during segmentation. Therefore, the outlines performed on this set of images was established as the reference for outlines performed on the other sets of images (50 keV, 120 keV and polyenergetic). Differences between referenced outline and the other outlines were analysed by the Sørensen–Dice coefficient (DSC) [23,24] and by the relative volumes of the outlined structures. The DSC was defined in this example as:

$$DSC = \frac{2(V_R \cap V_X)}{V_R + V_X} \quad (8)$$

where  $V_R$  is the volume of structure obtained during segmentation on the set of 70 keV images,  $V_X$  is the volume of structure obtained during segmentation on the other sets of images and

$V_R \cap V_X$  is a common part of these volumes.

The relative volumes ( $V_{norm}$ ) were defined in per cent as the relation between the volume of the structure obtained during segmentation on

the other sets of images ( $V_X$ ) to the volume of structure obtained during segmentation on the set of 70 keV images ( $V_R$ ).

Table 2 shows the results of analysis for the differences between the reference outline and the other outlines. For both methods of segmentation (automatic for bones and manual for tongue), the differences between the coverage of the outlines performed on different sets of images as well as the differences in relative volumes were detected. These differences can affect the dose distribution in the treatment plans for dynamic techniques of radiotherapy (e.g. intensity modulated radiotherapy or volumetric modulated arc therapy) where inverse planning is used.

Both of these examples are limited to one patient and one investigator (physicist in the first example and radiation oncologist in the other one). Therefore, it should be interpreted as a clinical illustration of our analysis rather than a fundamental part of our study. In future studies, reconstructed monoenergetic scans for 70 keV will be analyzed for clinical use for tumor and organs at risk delineation.

Taking the results of this study, the energy of 70 keV was selected as potentially the best for the reconstruction of monoenergetic images.

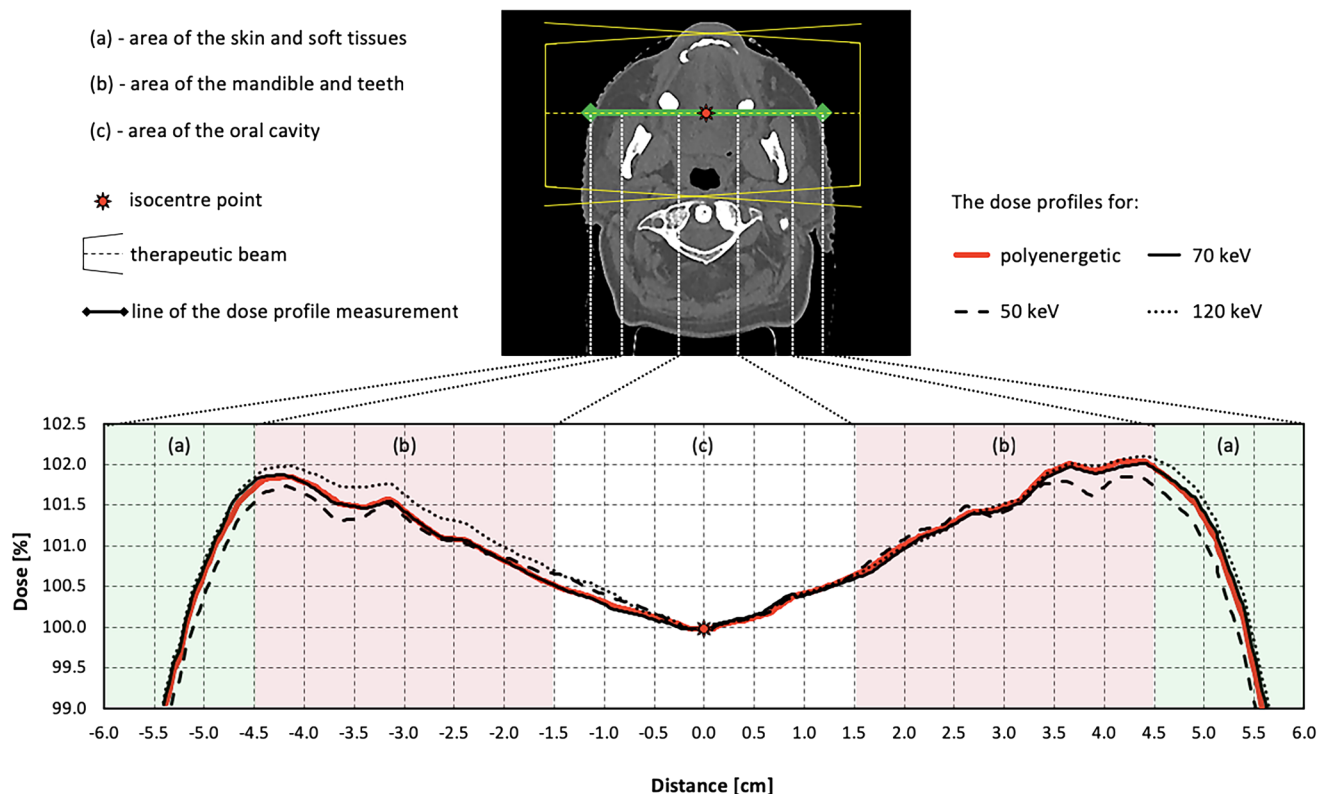


**Fig. 6.** The differences between doses calculated on four different sets of images (i.e. three sets of monoenergetic images with energies of 50 keV, 70 keV, 120 keV and one set of polyenergetic images) while one calibration curve (for polyenergetic images) was applied.

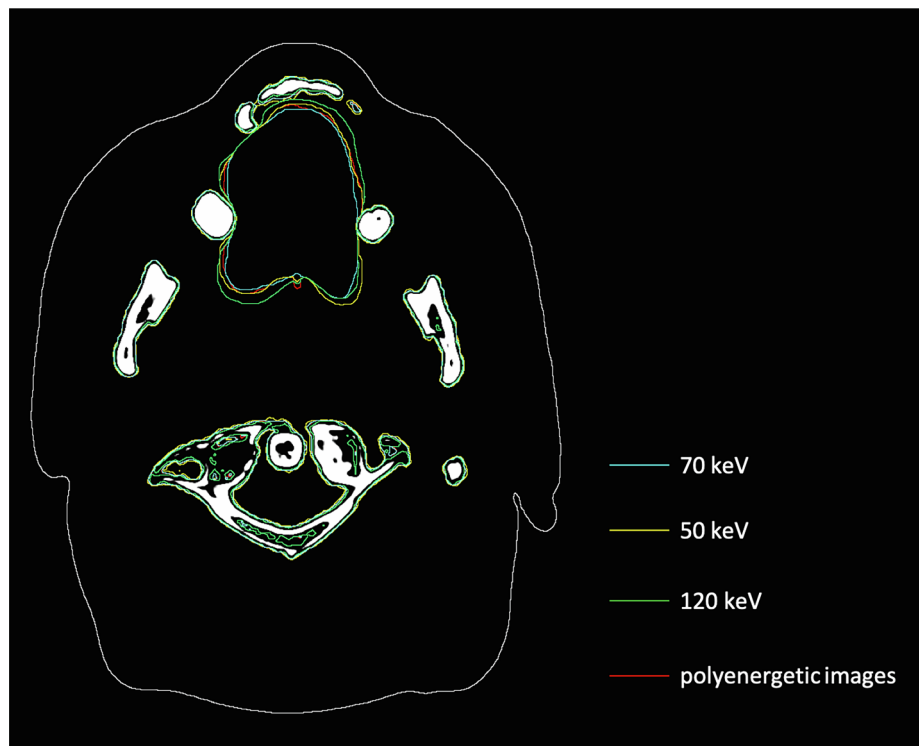


**Fig. 7.** The outlines for the bones (automatic segmentation) and for the tongue (manual segmentation) prepared on four different sets of images, i.e. on three monoenergetic sets with energies of 50 keV, 70 keV and 120 keV and on one set of polyenergetic images.

**Table 2**

The differences between the outlines obtained from set of 70 keV images and the outlines from the sets of 50 keV, 120 keV and polyenergetic images.

| Structure:                 | Bones     | Tongue                |
|----------------------------|-----------|-----------------------|
| Method of segmentation:    | Automatic | Manual                |
| Reference outlines: 70 keV | DSC       | V <sub>norm</sub> [%] |
| 50 keV:                    | 1.000     | 109.1                 |
| 120 keV:                   | 0.940     | 89.0                  |
| Polyenergetic images:      | 0.976     | 99.8                  |
|                            |           | DSC                   |
|                            |           | V <sub>norm</sub> [%] |
|                            |           | 0.994                 |
|                            |           | 117.0                 |
|                            |           | 0.995                 |
|                            |           | 131.7                 |
|                            |           | 0.996                 |
|                            |           | 101.7                 |

DSC – Sørensen–Dice coefficient between the structure contoured on X set of images and the same structure contoured on the set of images with energy of 70 keV.

V<sub>norm</sub> [%] – Volume of the structure contoured on X set of images, normalised to volume of the same structure contoured on the set of images with energy of 70 keV.

## 5. Conclusion

To improve relative uniformity, low contrast resolution, noise and signal to noise ratio, monoenergetic CT sets of images reconstructed from dual energy CT scanning can be used. The best results of the above pointed parameters were obtained for images reconstructed for energy of 70 keV that are potentially the best for radiotherapy treatment plan preparation.

## Declaration of Competing Interest

None.

## Acknowledgements

This study was supported by the Greater Poland Cancer Centre institutional grant no 19/2015(111).

## References

- [1] McCollough CH, Leng S, Yu L, Fletcher JG. Dual- and multi-energy CT: principles, technical approaches, and clinical applications. *Radiology* 2015;276(3):637–53.
- [2] Zarzour JC, Milner D, Valentim R, Jackson BE, Gordetsky J, West J, et al. Quantitative iodine content threshold for discrimination of renal cell carcinomas using rapid kV-switching dual-energy CT. *Abdom Radiol (NY)* 2017;42(3):727–34.
- [3] Flohr TG, McCollough CH, Bruder H, Petersilka M, Gruber K, Stüss C, et al. First performance evaluation of a dual-source CT (DSCT) system. *Eur Radiol* 2006;16(2):256–68.
- [4] Johnson TR, Krauss B, Sedlmair M, Grasnick M, Bruder H, Morhard D, et al. Material differentiation by dual energy CT: initial experience. *Eur Radiol* 2007;17(6):1510–7.
- [5] Matsubara K, Nagata H, Okubo R, Takata T, Kobayashi M. Method for determining the half-value layer in computed tomography scans using a real-time dosimeter: application to dual-source dual-energy acquisition. *Phys Med* 2017;44:227–31.
- [6] Kalender WA, Klotz E, Suess C. Vertebral bone mineral analysis: an integrated approach with CT. *Radiology* 1987;164(2):419–23.
- [7] Kalender WA, Perman WH, Vetter JR, Klotz E. Evaluation of a prototype dual energy computed tomographic apparatus. I. Phantom studies. *Med Phys* 1986;13(3):334–9.
- [8] Patel BN, Marin D. Strategies to improve image quality on dual-energy computed tomography. *Radiol Clin North Am* 2018;56(4):641–7.
- [9] Alvarez RE, Macovski A. Energy-selective reconstructions in x-ray computerized tomography. *Phys Med Biol* 1976;21(5):733–44.
- [10] Macovski A, Alvarez RE, Chan JL, Stonestrom JP, Zatz LM. Energy dependent reconstruction in x-ray computerized tomography. *Comput Biol Med* 1976;6(4):325–36.
- [11] Tsang DS, Merchant TE, Merchant SE, Smith H, Yagil Y, Hua C-H. Quantifying potential reduction in contrast dose with monoenergetic images synthesized from dual-layer detector spectral CT. *Br J Radiol* 2017;90:20170290.
- [12] Mei K, Ehn S, Oechsner M, Kopp FK, Pfeiffer D, Fingerle AA, et al. Dual-layer spectral computed tomography: measuring relative electron density. *Eur Radiol Exp* 2018;2:20.
- [13] Sakabe D, Funama Y, Taguchi K, Nakaura T, Utsunomiya D, Oda S, et al. Image quality characteristics for virtual monoenergetic images using dual-layer spectral detector CT: comparison with conventional tube-voltage images. *Phys Med* 2018;49:5–10.
- [14] van Ommen F, Bennink E, Vlassenbroek A, Dankbaar JW, Schilham AMR, Viergever MA, et al. Image quality of conventional images of dual-layer SPECTRAL CT: a phantom study. *Med Phys* 2018;45(7):3031–42.
- [15] Shikhaliev PM. Energy-resolved computed tomography: first experimental results. *Phys Med Biol* 2008;53(20):5595–613.
- [16] Taguchi K, Iwanczyk JS. Vision 20/20: single photon counting X-ray detectors in medical imaging. *Med Phys* 2013;40(10):100901.
- [17] Atak H, Shikhaliev PM. Dual energy CT with photon counting and dual source systems: comparative evaluation. *Phys Med Biol* 2015;60(23):8949–75.
- [18] Leng S, Zhou W, Yu Z, Halaweh A, Krauss B, Schmidt B, et al. Spectral performance of a whole-body research photon counting detector CT: quantitative accuracy in derived image sets. *Phys Med Biol* 2017;62(17):7216–32.
- [19] Gulliksrød K, Stokke C, Martinsen AC. How to measure CT image quality: variations in CT-numbers, uniformity and low contrast resolution for a CT quality assurance phantom. *Phys Med* 2014;30(4):521–6.
- [20] Verdun FR, Racine D, Ott JG, Tapiolaara MJ, Toroi P, Bochuda FO, et al. Image quality in CT: from physical measurements to model observers. *Phys Med* 2015;31(8):823–43.
- [21] ARTISCAN Details of parameters, Phantom CATPHAN Modality CT, Annex A1.27. <http://www.aquilab.com>.
- [22] Catphan 500 and 600 Manual. The Phantom Laboratory. <https://www.phantomlab.com>.
- [23] Sørensen T. A method of establishing groups of equal amplitude in plant sociology based on similarity of species and its application to analyses of the vegetation on Danish commons. *Kongelige Danske Videnskabernes Selskab* 1948;5(4):1–34.
- [24] Dice LR. Measures of the amount of ecological association between species. *Ecology* 1945;26(3):297–302.



## Original paper

## Combination of dual-energy computed tomography and iterative metal artefact reduction to increase general quality of imaging for radiotherapy patients with high dense materials. Phantom study



Bartosz Pawałowski<sup>a,b</sup>, Rafał Panek<sup>c,d</sup>, Hubert Szweda<sup>a</sup>, Tomasz Piotrowski<sup>a,e,\*</sup>

<sup>a</sup> Department of Medical Physics, Greater Poland Cancer Centre, Poznań, Poland

<sup>b</sup> Department of Technical Physics, Poznan University of Technology, Poznań, Poland

<sup>c</sup> Medical Physics & Clinical Engineering, Nottingham University Hospitals NHS Trust, Nottingham, UK

<sup>d</sup> School of Medicine, University of Nottingham, Nottingham, UK

<sup>e</sup> Department of Electroradiology, Poznań University of Medical Sciences, Poznań, Poland

## ARTICLE INFO

**Keywords:**

Metal artefact reduction

Dual energy CT

iMAR

Quality of CT images

Imaging for radiation therapy

## ABSTRACT

**Purpose:** To evaluate the use of pseudo-monoenergetic reconstructions (PMR) from dual-energy computed tomography, combined with the iterative metal artefact reduction (iMAR) method.

**Methods:** Pseudo-monoenergetic CT images were obtained using the dual-energy mode on the Siemens Somatom Definition AS scanner. A range of PMR combinations (70–130 keV) were used with and without iMAR. A Virtual Water™ phantom was used for quantitative assessment of error in the presence of high density materials: titanium, alloys 330 and 600. The absolute values of CT number differences (AD) and normalised standard deviations (NSD) were calculated for different phantom positions. Image quality was assessed using an anthropomorphic pelvic phantom with an embedded hip prosthesis. Image quality was scored blindly by five observers.

**Results:** AD and NSD values revealed differences in CT number errors between tested sets. AD and NSD were reduced in the vicinity of metal for images with iMAR ( $p < 0.001$  for AD/NSD). For ROIs away from metal, with and without iMAR, 70 keV PMR and pCT AD values were lower than for the other reconstructions ( $p = 0.039$ ). Similarly, iMAR NSD values measured away from metal were lower for 130 keV and 70 keV PMR ( $p = 0.002$ ). Image quality scores were higher for 70 keV and 130 keV PMR with iMAR ( $p = 0.034$ ).

**Conclusion:** The use of 70 keV PMR with iMAR allows for significant metal artefact reduction and low CT number errors observed in the vicinity of dense materials. It is therefore an attractive alternative to high keV imaging when imaging patients with metallic implants, especially in the context of radiotherapy planning.

## 1. Introduction

Dual-energy computed tomography (DECT) is increasingly used to improve general image quality of computed tomography (CT) in brachy and radiotherapy planning [1–4]. Several technical solutions of DECT have been proposed [5–11], providing additional information on linear attenuation coefficients and allowing for pseudo-monoenergetic reconstruction (PMR) of CT images. It has been shown that 70 keV reconstructed PMR images have superior uniformity, low contrast resolution and signal to noise ratio in comparison to conventional polyenergetic CT (pCT) [12,13]. In these studies, the main goal was to appropriately differentiate between the tissues/materials of different elemental compositions represented by very similar CT numbers on the pCT images such as calcified plaques and iodine-containing lymph

nodes.

An important application of DECT is the reduction of artefacts generated by high density materials present in patients' implanted devices. Typical metal artefacts occur predominantly due to two physical effects: photon starvation and beam hardening, which increase the image noise and produce "signal bands"; both of these effects create insufficient soft tissue contrast [14,15].

These artefacts significantly limit the ability to evaluate adjacent anatomic structures on standard pCT images [16]. One possible solution is a use of high tube voltages of up to 140 kV, resulting in reduction of beam hardening. It was shown that the use of pseudo-monoenergetic CT images, reconstructed for energy that ranged from 120 keV to 150 keV, provided a significant reduction of artefacts caused by metallic implants [17–21]. Zhou *et al.* [22] reported the lowest metal artefacts at 130 keV.

\* Corresponding author at: Department of Medical Physics, Greater Poland Cancer Centre, Garbary 15, 61-866 Poznań, Poland.

E-mail address: [tomasz.piotrowski@wco.pl](mailto:tomasz.piotrowski@wco.pl) (T. Piotrowski).

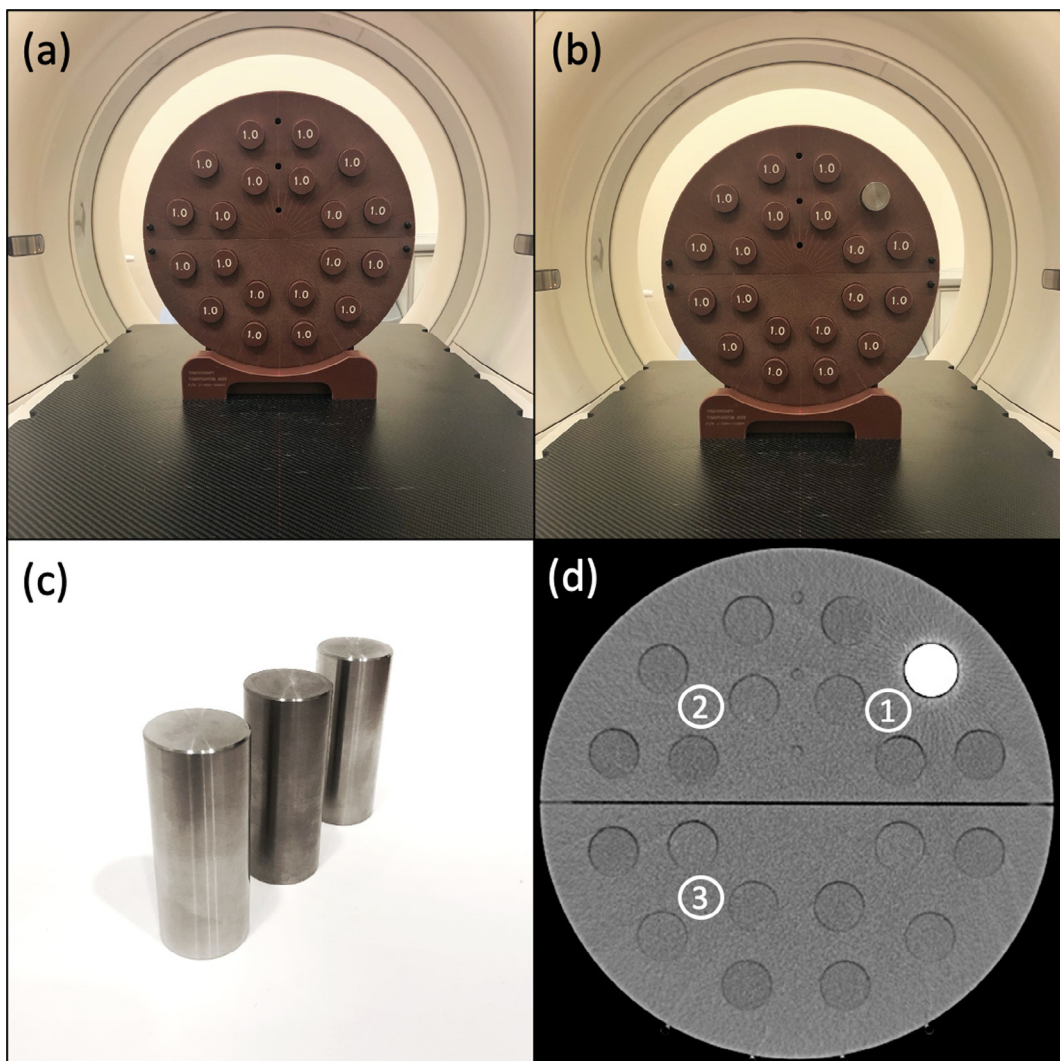


**Fig. 1.** Experimental setup, Phantom 1: (a) plain inserts, (b) plain inserts with a single high density insert, (c) titanium, alloy 330 and alloy 600 inserts and (d) CT image with the high density insert and location of three regions of interest.

**Table 1**  
The chemical composition and density of inserts used in the study.

| Chemical Composition         | Insert  |   |   |
|------------------------------|---|---|---|
|                              | Titanium  | Alloy 330   | Alloy 600   |
| Main Components              | Ti: > 99.9%   | Fe: 39%<br>NiCo: 37%<br>Cr: 19%<br>Fe: 10%              | NiCo: 72%<br>Cr: 17%<br>Fe: 10%                         |
| Supplementary Components     | Fe: 0.25%<br>O: 0.25%<br>C: 0.08%<br>N: 0.03%<br>H: 0.02% | Si: 2.6%<br>Mn: 1.5%<br>Cu: 0.5%<br>Ti: 0.2%<br>C: 0.1% | Mn: 1%<br>Cu: 0.5%<br>Si: 0.5%<br>C: 0.15%<br>S: 0.015% |
| Density [g/cm <sup>3</sup> ] | 4.51  | 7.86  | 8.47  |

Another method is the iterative metal artefact reduction algorithm (iMAR), which uses a sinogram inpainting technique incorporating high-frequency data from standard weighted filtered back projection reconstructions [23–25]. A recent study by Kim *et al.* [26] demonstrates superiority of the iMAR method over the DECT metal artefact reduction technique, facilitating visualization of the acetabular cortex in a loosening hip phantom model. A similar observation, but performed on a wider spectrum of clinical cases, was made by Bongers *et al.* [15].

Moreover, that study highlighted a significant benefit of combining the 130 keV PMR with iMAR in quantitative analysis of very pronounced metal artefacts caused by dental implants. For smaller artefacts (e.g. caused by unilateral hip prosthesis), the benefit of combining 130 keV reconstructed from DECT and iMAR was not confirmed. This is in line with the Lim *et al.* study [27], which reported comparable results obtained for DECT combined with iMAR and pCT combined with iMAR for a unilateral hip prosthesis.

In this study, we evaluated the use of pseudo-monoenergetic reconstructions (PMR) from dual-energy computed tomography (DECT), combined with the iterative metal artefact reduction (iMAR) method. We investigated general image quality, artefact reduction effectiveness and CT number errors caused by the presence of dense materials commonly used in implanted devices.

## 2. Material and method

### 2.1. Test objects

Phantom 1: Virtual Water™ (Gammex RMI, Middleton, WI, USA). A 30 cm diameter cylindrical phantom composed of 18 cm thick solid water with a matrix of 20 removable inserts. Plain inserts matching the rest of the phantom density of 1.018 g/cm<sup>3</sup> were used in the study (Fig. 1a). One of the inserts was subsequently replaced with a high

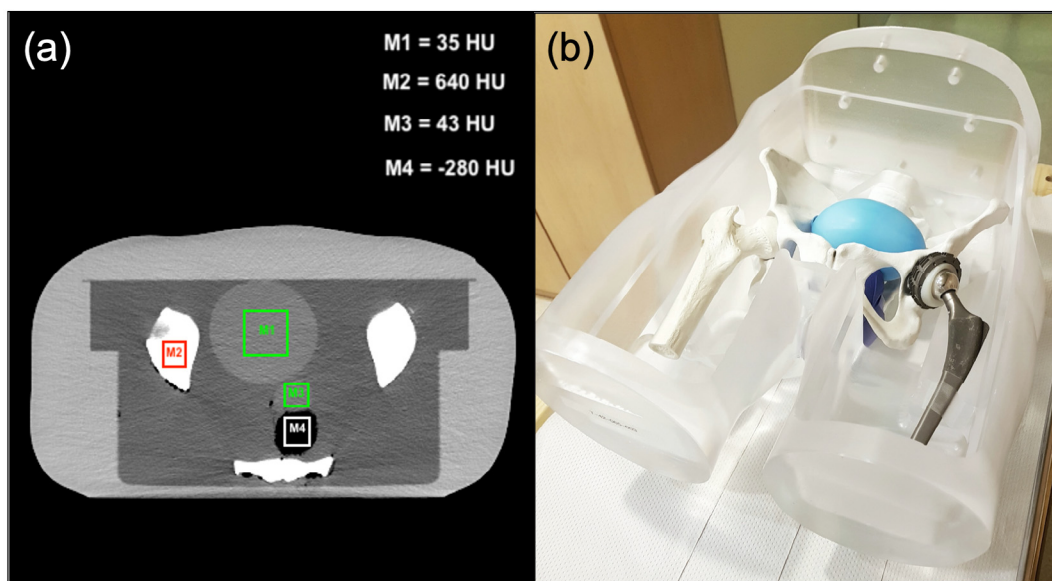


**Fig. 2.** Phantom 2: custom made, anthropomorphic phantom of the pelvic region with unilateral hip prosthesis. The phantom was filled with water and contains bladder (M1 ROI mean = 35 HU), bones (M2 ROI mean = 640HU) and soft- tissue structures: prostate (M3 ROI mean = 43 HU) and rectum (M4 ROI mean = 280 HU).

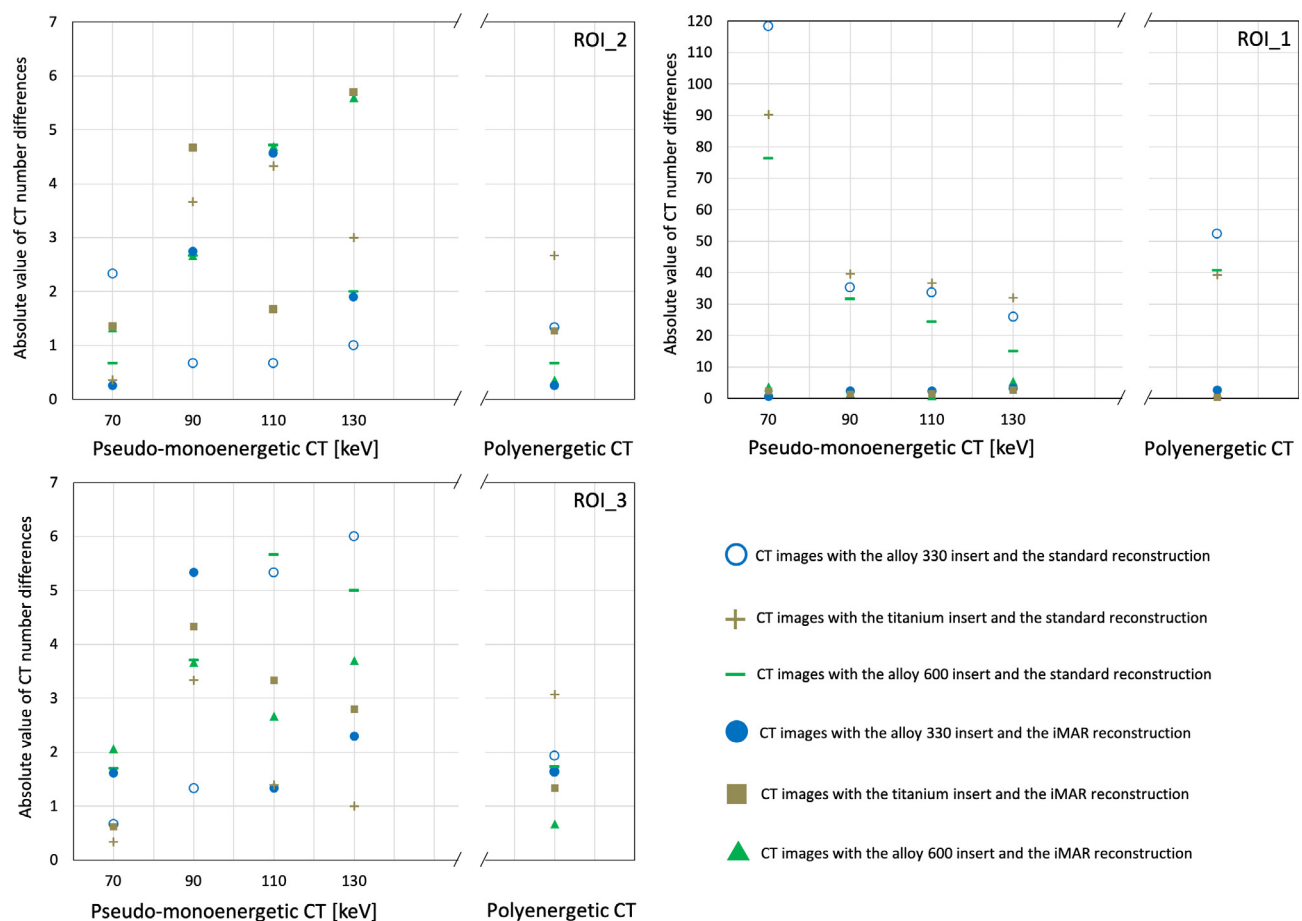


**Fig. 3.** The absolute value of CT number differences (AD) obtained for different energies, inserts and methods of reconstruction, for each ROI separately (Phantom 1).

density insert (Fig. 1b-c). Three different materials commonly used in hip endoprosthesis implants were tested: titanium, alloy 330 and alloy 600 (Fig. 1c). The chemical composition and the density of the inserts are summarised in Table1.

Phantom 2: An anthropomorphic water filled

polymethylmethacrylate (milled PMMA) pelvic phantom (maximum dimensions: A-P: 230 mm, R-L: 375 mm, S-I: 450 mm). The phantom included 3D printed male bones (pelvic bone and femurs with femoral heads) made from gypsum using a binder jetting technology (Fig. 2b) [28–30]. In addition, the phantom contained soft tissue structures:

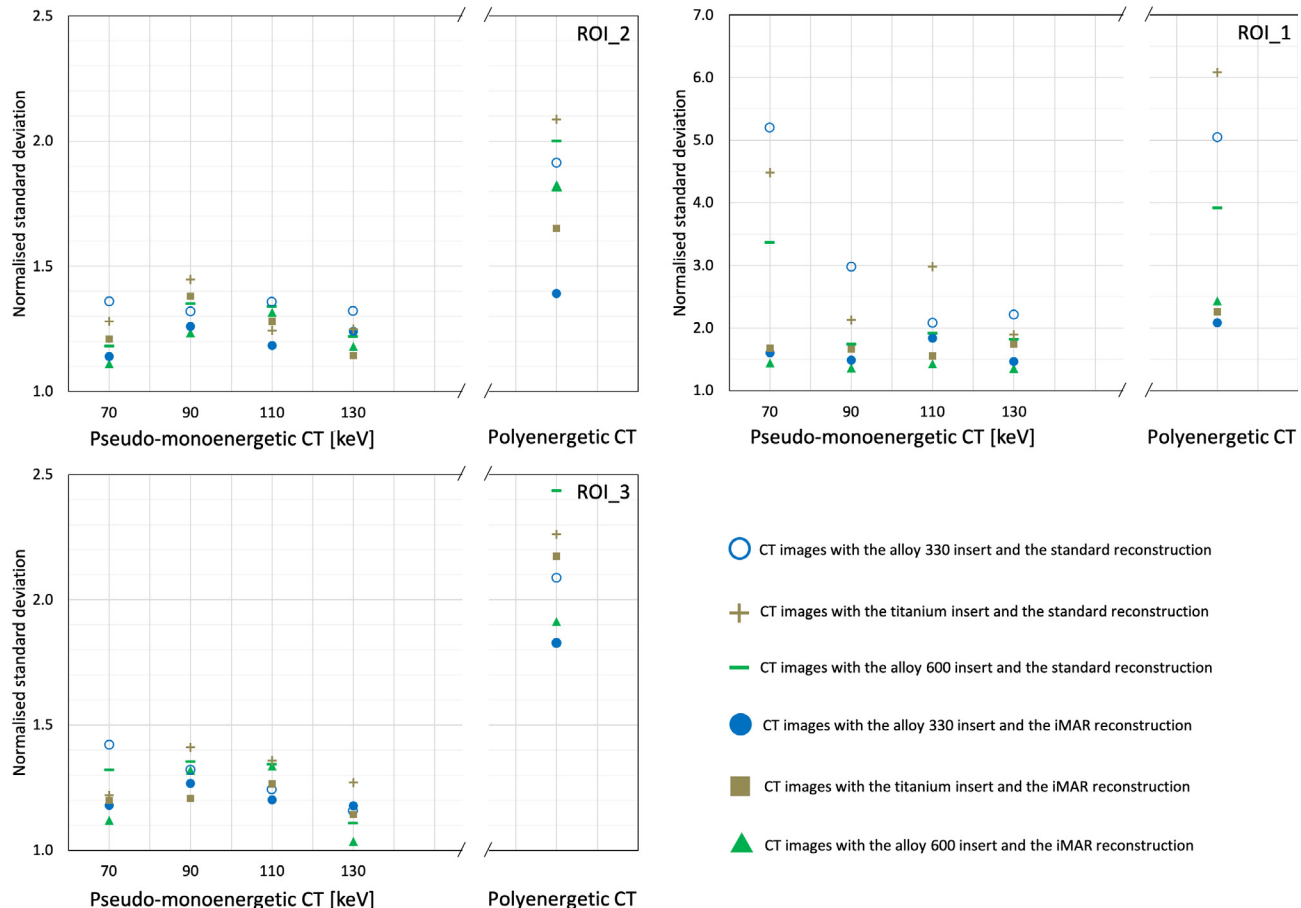


**Fig. 4.** The normalised standard deviation of CT numbers (NSD) obtained for different energies, inserts and methods of reconstruction, for each ROI separately (Phantom 1).

prostate (agarose gel) [29], rectum (mixture of wax and paraffin) [31] and bladder (mixture of water and soap). Volumes of prostate, bladder and rectum were 26 cm<sup>3</sup>, 360 cm<sup>3</sup> and 50 cm<sup>3</sup> respectively [32,33]. All inserts were made to achieve a CT number similar to structures represented (Fig. 2a). The stem of the endoprosthesis is made of ISOTAN® F (Ti – titanium) and the cup is made of ISODUR® F (CoCrMo – Cobalt-chromium alloy).

## 2.2. CT image acquisition and reconstruction

Images were obtained using the Somatom Definition AS scanner (Siemens Medical Solutions, Erlangen, Germany). The phantoms were scanned with routine settings using SAFIRE algorithm, without CARE-DOSE. The pelvis protocol (120 kV, 270 mAs, 1.0 pitch, 64 × 0.6 mm acquisition, 3 mm slice thickness, kernel Q30s) was used during the pCT scanning. DECT was performed using a two consecutive scans technique (first scan: 80 kV, 540 mAs, 0.6 pitch, 64 × 0.6 mm acquisition, 3 mm slice thickness; second scan: 140 kV, 128 mAs, 1.2 pitch, 64 × 0.6 mm acquisition, 3 mm slice thickness, kernel Q30s). Standard pCT and four monoenergetic CT sets of images (70, 90, 110 and 130 keV) were reconstructed twice: once with and once without the iMAR algorithm. The CTDIvol was 22.13 mGy for pelvis protocol and 13.10 mGy and 15.27 mGy for first and second DE scan, respectively.

## 2.3. Quantitative image analysis

Mean CT numbers were obtained for three circular regions of interest (ROI) and all Phantom 1 data sets, using Artisan software (AQUILAB, Loos les Lille, France). Fig. 1d shows ROIs distribution in

the phantom with ROI\_1 positioned in the vicinity of the high-density material.

The absolute value of CT number differences (AD) and the normalised standard deviations of CT numbers (NSD) were used to compare the data acquired for all combinations of PMR, pCT, iMAR and tested inserts [34,35]. These were defined as:

$$AD = |CTnumber_{ROI_i, E_j, I_n, Recon_k} - CTnumber_{ref}| \quad (1)$$

and

$$NSD = \frac{SD(CTnumber_{ROI_i, E_j, I_n, Recon_k})}{SD(CTnumber_{ref})} \quad (2)$$

where:  $CTnumber_{ROI_i, E_j, I_n, Recon_k}$  is the mean CT number value for the  $i$ th ROI ( $ROI_i$ ),  $n$ th insert ( $I_n$ ) in an image obtained with energy  $j$  ( $E_j$ ) and reconstructed with method  $k$  ( $Recon_k$ ).  $SD(CTnumber_{ROI_i, E_j, I_n, Recon_k})$  is the standard deviation for the same ROI.  $SD(CTnumber_{ref})$  and  $CTnumber_{ref}$  are the standard deviation and average of CT numbers from all ROIs for a reference image without a high-density insert ( $E_j$  energy, no iMAR).

CT numbers were defined according to Coolens and Childs [34] as HU plus 1000, in order to associate zero attenuation with a CT number of 0 rather than −1000.

The statistical dispersion and central tendency of ROIs were tested, respectively by Kolmogorov-Smirnov and Mann-Whitney tests [36].

Differences between ADs and NSDs obtained for all CT sets were tested using Wilcoxon test for two paired data sets (e.g. with and without iMAR reconstruction) and Friedman test (comparison of multiple data sets, e.g. energy), respectively. Multiple pairwise comparisons were accounted for Friedman test using Nemenyi's procedure. All tests were performed with a 0.05 significance level.

**Table 2**  
Summary of statistical analysis of the absolute value of CT number differences (AD) and the normalised standard deviations of CT numbers (NSD) for different energies, inserts and use of iMAR.

|  | ROI_1               | ROI_2 and ROI_3   |                     |   |
|--|---------------------|---|---------------------|---|
|  | p value (**)        | Description   | p value (**)        | Description   |
| <i>Statistical analysis for absolute values of CT number differences (AD):</i> |                     |   |                     |   |
| 1<br>with iMAR vs without iMAR   | <b>p &lt; 0.001</b> | AD for reconstruction with iMAR significantly lower                                       | <b>p = 0.727</b>    | No statistically significant differences                                    |
| 2<br>without iMAR vs Energy  | <b>p = 0.022</b>    | AD lowest for 130 keV PMR. Statistical significance between 130 keV PMR and 70 keV PMR    | –                   | –   |
| with iMAR vs Energy  | <b>p = 0.153</b>    | No statistically significant differences  | <b>p &lt; 0.039</b> | Values for pCT and 70 keV PMR significantly lower than for the rest         |
| with or without iMAR vs Energy (*)   | –                   | –   | –                   | –   |
| 3<br>without iMAR vs Insert  | <b>p = 0.368</b>    | No statistically significant differences  | <b>p = 0.541</b>    | No statistically significant differences                                    |
| with iMAR vs Insert  | <b>p = 0.421</b>    | No statistically significant differences  | –                   | –   |
| with or without iMAR vs Insert (*)   | –                   | –   | –                   | –   |
| <i>Statistical analysis for normalised standard deviations (NSD):</i>          |                     |   |                     |   |
| 1<br>with iMAR vs without iMAR   | <b>p &lt; 0.001</b> | NSD for reconstruction with iMAR significantly lower                                      | <b>p &lt; 0.001</b> | NSD for reconstruction with iMAR significantly lower                        |
| 2<br>without iMAR vs Energy  | <b>p = 0.048</b>    | NSD the lowest for 130 keV PMR. Statistical significance between 130 keV PMR and the rest | <b>p = 0.003</b>    | Values for pCT significantly higher than for the rest                       |
| with iMAR vs Energy  | <b>p = 0.113</b>    | No statistically significant differences  | <b>p = 0.002</b>    | Values for 130 keV PMR and 70 keV PMR significantly lower than for the rest |
| with or without iMAR vs Energy (*)   | –                   | –   | <b>p = 0.004</b>    | Values for 130 keV PMR and 70 keV PMR significantly lower than for the rest |
| 3<br>without iMAR vs Insert  | –                   | –   | <b>p = 0.356</b>    | No statistically significant differences                                    |
| with iMAR vs Insert  | <b>p = 0.268</b>    | No statistically significant differences  | <b>p = 0.302</b>    | No statistically significant differences                                    |
| with or without iMAR vs Insert (*)   | –                   | –   | –                   | –   |

(\*) Calculated if step 1 not statistically significant.

(\*\*) Significant differences ( $p < 0.05$ ) presented in bold.

**Table 3**

Summary of the qualitative analysis. Pseudo-monoenergetic and polyenergetic CT (pCT) images without (Group A) and with iMAR reconstruction (Group B).

| Group A     |                                      |    |     |     |            |
|-------------|--------------------------------------|----|-----|-----|------------|
| Observer    | pseudo-monoenergetic CT images [keV] |    |     |     | pCT images |
|             | 70                                   | 90 | 110 | 130 |            |
| 1           | 0                                    | 1  | 2   | 3   | 0          |
| 2           | 0                                    | 2  | 1   | 3   | 0          |
| 3           | 0                                    | 0  | 2   | 3   | 1          |
| 4           | 0                                    | 1  | 3   | 2   | 0          |
| 5           | 0                                    | 0  | 3   | 2   | 1          |
| Total Score | 0                                    | 4  | 11  | 13  | 2          |

| Group B     |  |    |     |     |                      |
|-------------|--|----|-----|-----|----------------------|
| Observer    | pseudo-monoenergetic CT images [keV] with iMAR |    |     |     | pCT images with iMAR |
|             | 70   | 90 | 110 | 130 |                      |
| 1           | 2  | 0  | 0   | 1   | 3                    |
| 2           | 3  | 0  | 0   | 2   | 1                    |
| 3           | 3  | 2  | 0   | 1   | 0                    |
| 4           | 2  | 0  | 1   | 3   | 0                    |
| 5           | 1  | 0  | 0   | 3   | 2                    |
| Total Score | 11   | 2  | 1   | 10  | 6                    |

#### 2.4. Qualitative image assessment

CT image sets acquired using Phantom 2 were evaluated by five Medical Physics Experts (MPEs). The readers were blinded to the type of reconstruction (e.g. PMR keV, use of iMAR). The evaluation criteria included: (a) efficiency of metal artefact reduction, (b) noise level and (c) high contrast resolution. All the axial images for each series were used.

In the first evaluation a set of pCT and four sets of pseudo-monoenergetic CT images (70, 90, 110 and 130 keV) that had been reconstructed without iMAR were used (Group A). Next, the corresponding of images that had been reconstructed with iMAR were scored (Group B). Readers were asked to assign scores (1–3) to three best image sets per group, where a score of 3 indicated the best image quality. They were also asked to indicate their dominant evaluation criterion (a–c).

In the last round, readers were asked to indicate the better set of CT images in a paired comparison, where a set of images from Group A was compared with the corresponding set from Group B.

Differences between scores obtained from the first two evaluations were tested using the Friedman test. Paired image comparison (Group A vs. Group B) scores were assessed using the sign test. Both tests were performed with a 0.05 significance level.

### 3. Results

#### 3.1. Quantitative assessment

Figs. 3 and 4 show, respectively, AD and NSD calculated for different energies, inserts and methods of reconstruction, for each ROI separately.

There was a statistical difference between the AD and the NSD measured for ROI\_1 and ROI\_2/ROI\_3 ( $p < 0.05$ ), and no difference between ROI\_2 and ROI\_3 ( $p = 0.346$  and  $p = 0.848$  for AD and NSD respectively).

Results of statistical analysis of AD and NSD for different energies, inserts and use of iMAR (Figs. 3 and 4) are summarised in Table 2.

For ROI\_1 the use of iMAR resulted with a significant reduction of AD ( $p < 0.001$ ) and NSD ( $p < 0.001$ ). There were no significant

differences between ROI\_1 AD ( $p = 0.153$ ) or NSD ( $p = 0.113$ ) observed for different PMR energies with iMAR.

For ROI\_2 and ROI\_3 AD values were significantly lower for pCT and 70 keV PMR with and without iMAR ( $p < 0.039$ ). Significantly lower NSD was observed in ROI\_2 and ROI\_3 for 130 keV PMR and 70 keV PMR ( $p = 0.002$ ) with iMAR.

#### 3.2. Qualitative assessment

The results of the qualitative evaluation (Phantom 2) are summarised in Table 3. The quality of images reconstructed with iMAR was superior to those without iMAR ( $p < 0.001$ ). Of the images reconstructed without iMAR (Group A, Table 3), the 130 keV pseudo-monoenergetic CT were scored as having the best image quality (13 points,  $p = 0.004$ ). The 110 keV PMR images scored second best (11 points). Readers indicated that efficacy of the metal artefact reduction was their dominant scoring decision criterion in this group.

There was more scoring discrepancy for the CT images with iMAR (Group B, Table 3). The differences in scores for different PMR and pCT were statistically significant ( $p = 0.034$ ) but two best PMR sets had comparable score (70 keV: 11 points and 130 keV: 10 points). As in the previous group, reduction of metal artefacts was the dominant indicated criterion. In addition, readers who scored the 70 keV PMR images supported their choice by better noise reduction and those who selected 130 keV PMR, by better high contrast resolution.

Representative pCT, 70 keV and 130 keV pseudo-monoenergetic images acquired for Phantom 2, with and without iMAR are presented in Fig. 5.

### 4. Discussion

Several techniques have been proposed for reducing artefacts in clinical CT images due to a presence of dense materials present in implanted devices. These include higher energy DECT reconstructed images and iterative reconstruction metal reduction techniques. Combinations of the two techniques have previously been studied [24,26,27]; however, systematic assessment of general image quality, artefact reduction effectiveness and CT number errors caused by the presence of implants, performed for a range of keV pseudo-monoenergetic reconstructions, have not yet been reported. The goal of the comparisons performed in this study was to explore optimal choice of pseudo-monoenergetic reconstructions combined with iMAR metallic artefact reduction. We explored parameters allowing for a good compromise between metal artefact reduction whilst maintaining good overall image quality and reliable CT numbers estimates, which are important in the context of radiotherapy planning.

The routine quality evaluation methods and phantoms allow determining parameters such as linearity, low and high contrast resolution, uniformity, noise and signal to noise ratio. Most of them, however, are not suitable to assess image quality in the presence of metallic materials. In this study we carried out highly reproducible tests using test objects that allow for quantitative assessment in a well geometrically defined phantom with various custom made inserts.

While the evaluation of the reduction of metal artefacts usually focuses on the regions located within close proximity of to the high-density materials, the impact on overall image quality should be performed taking the whole image into account. We therefore decided to select several regions of interest in the phantom that were used in the quantitative analysis.

The evaluation metrics used in this study were the absolute value of CT number differences (AD) and normalised standard deviation of CT number (NSD). AD relates to an increase or decrease of the average value of CT numbers, which would lead to miscalculation of relative electron or physical densities and subsequent radiotherapy dose errors. NSD indicates variances of the CT number caused by different values of Hounsfield units in the specified ROI. For the homogenous phantom, as

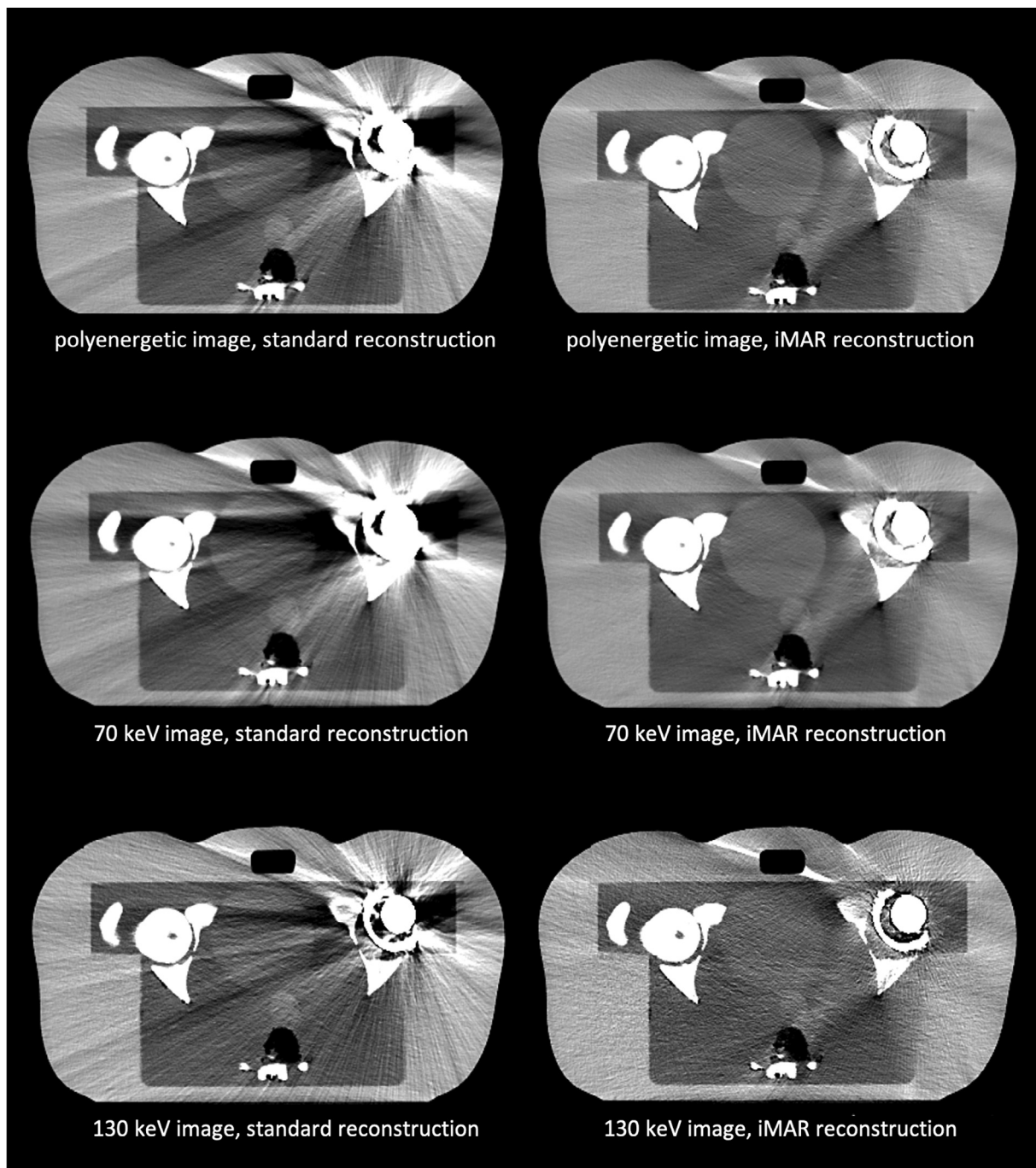


Fig. 5. Representative pCT, 70 keV and 130 keV pseudo-monoenergetic images with and without iMAR (Phantom 2).

that of Fig. 1a, the variances are expected to be small at the absence of high-density inserts. They increase significantly when images contain metallic inserts, which enables evaluation of the metal artefact in different parts of the image.

Our results show that the lowest NSDs were observed for PMR of the 70 keV and 130 keV images with iMAR reconstruction. These results were significantly better than for other pseudo-monoenergetic CT or pCT images. Moreover, while for iMAR images a significant reduction of AD and NSD was evident in the ROI placed near the high density insert, a further benefit of the high energy selection (e.g. 130 keV) on decreasing AD or NSD was not observed. These observations suggest that the combination of 70 keV PMR with iMAR results in a very good reduction of metal artefacts and a superior image quality in comparison with higher PMR and pCT images.

In order to further investigate these findings, a custom-made anthropomorphic phantom of pelvic region with unilateral hip prosthesis was prepared and imaged using combinations of the PMR and iMAR methods. In the absence of iMAR, the qualitative image evaluation revealed the highest score in 130 keV pseudo-monoenergetic images, which is in line with previous studies [22]. Overall, the sets of CT images in Group A (PMR without iMAR) were rated as having lower image quality than the sets of CT images in Group B (PMR with iMAR). In Group B, the PMR of 70 keV was top rated and 130 keV was rated second best, with a comparable score (11 and 10 respectively).

One of the limitations of this qualitative analysis was that it was performed by Medical Physics Experts, without involvement of radiation oncologists or radiologists. The analysis was, however, performed using a simplified anatomical model allowing for easy assessment of

pronounced compartments and structures. The choice of geometries and materials might not fully reflect important clinical regimes, such as small structures and subtle pathology, which might not be easily visualised. This might be especially true for the lower energy PMR such as 70 keV. This warrants further clinical evaluation, for which radiology input and review of the imaging will be essential.

## 5. Conclusion

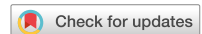
The use of 70 keV PMR with iMAR allows for significant metal artefact reduction and low CT number errors observed in the vicinity of dense materials. It is therefore an attractive alternative to high keV imaging when imaging patients with metallic implants, especially in the context of radiotherapy planning.

## Declaration of Competing Interest

The authors declare that they have no known competing financial interests or personal relationships that could have appeared to influence the work reported in this paper.

## References

- [1] Karino T, Ohira S, Kanayama N, Wada K, Ikawa T, Nitta Y, et al. Determination of optimal virtual monochromatic energy level for target delineation of brain metastases in radiosurgery using dual-energy CT. *Br J Radiol* 2020;93(1106):20180850. <https://doi.org/10.1259/bjr.20180850>.
- [2] Simard M, Lapointe A, Lalonde A, Bahig H, Bouchard H. The potential of photon-counting CT for quantitative contrast-enhanced imaging in radiotherapy. *Phys Med Biol* 2019;64(11):115020. <https://doi.org/10.1088/1361-6560/ab1af1>.
- [3] Kawahara D, Ozawa S, Yokomachi K, Higaki T, Shiinoki T, Ohno Y, et al. Evaluation of raw-data-based and calculated electron density for contrast media with a dual-energy CT technique. *Rep Pract Oncol Radiother*. 2019;24(5):499–506. <https://doi.org/10.1016/j.rpor.2019.07.013>.
- [4] Perisinakis K, Detorakis ET, Tzedakis A, Liakopoulos DA, Papadaki E, Damilakis J. Dual-energy CT imaging of orbits during episcleral brachytherapy with Ru-106 plaques: a phantom study on its potential for plaque position verification. *Phys Med* 2020;73:1–7. <https://doi.org/10.1016/j.ejmp.2020.03.020>.
- [5] Matsubara K, Nagata H, Okubo R, Takata T, Kobayashi M. Method for determining the half-value layer in computed tomography scans using a real-time dosimeter: application to dual-source dual-energy acquisition. *Phys Med* 2017;44:227–31. <https://doi.org/10.1016/j.ejmp.2017.10.020>.
- [6] Kalender WA, Perman WH, Vetter JR, Klotz E. Evaluation of a prototype dual energy computed tomographic apparatus. I. Phantom studies. *Med Phys* 1986;13(3):334–9. <https://doi.org/10.1118/1.595958>.
- [7] Patel BN, Marin D. Strategies to improve image quality on dual-energy computed tomography. *Radiol Clin North Am* 2018;56(4):641–7. <https://doi.org/10.1016/j.rcl.2018.03.006>.
- [8] Tsang DS, Merchant TE, Merchant SE, Smith H, Yagil Y, Hua C-H. Quantifying potential reduction in contrast dose with monoenergetic images synthesized from dual-layer detector spectral CT. *Br J Radiol* 2017;90:20170290. <https://doi.org/10.1259/bjr.20170290>.
- [9] Mei K, Ehn S, Oechsner M, Kopp FK, Pfeiffer D, Fingerle AA, et al. Dual-layer spectral computed tomography: measuring relative electron density. *Eur Radiol Exp* 2018;2:20. <https://doi.org/10.1186/s41747-018-0051-8>.
- [10] Sakabe D, Funama Y, Taguchi K, Nakaura T, Utsunomiya D, Oda S, et al. Image quality characteristics for virtual monoenergetic images using dual-layer spectral detector CT: comparison with conventional tube-voltage images. *Phys Med* 2018;49:5–10. <https://doi.org/10.1016/j.ejmp.2018.04.388>.
- [11] Atak H, Shikhaliev PM. Dual energy CT with photon counting and dual source systems: comparative evaluation. *Phys Med Biol* 2015;60(23):8949–75. <https://doi.org/10.1088/0031-9155/60/23/8949>.
- [12] Pawłowski B, Szweda H, Dudkowiak A, Piotrowski T. Quality evaluation of monoenergetic images generated by dual-energy computed tomography for radiotherapy: a phantom study. *Phys Med* 2019;63:48–55. <https://doi.org/10.1016/j.ejmp.2019.05.019>.
- [13] McCollough CH, Leng S, Yu L, Fletcher JG. Dual- and multi-energy CT: principles, technical approaches, and clinical applications. *Radiology* 2015;276(3):637–53. <https://doi.org/10.1148/radiol.2015142631>.
- [14] Barrett JF, Keat N. Artifacts in CT: recognition and avoidance. *Radiographics* 2004;24(6):1679–91. <https://doi.org/10.1148/rug.246045065>.
- [15] Bongers MN, Schabel C, Thomas C, Raupach R, Notohamiprodjo M, Nikolaou K, et al. Comparison and combination of dual-energy- and iterative-based metal artefact reduction on hip prosthesis and dental implants. *PLoS ONE* 2015;10(11):e0143584. <https://doi.org/10.1371/journal.pone.0143584>.
- [16] Lee MJ, Kim S, Lee SA, Song HT, Huh YM, Kim DH, et al. Overcoming artifacts from metallic orthopedic implants at high-field-strength MR imaging and multi-detector CT. *Radiographics* 2007;27(3):791–803. <https://doi.org/10.1148/rg.273065087>.
- [17] Han SC, Chung YE, Lee YH, Park KK, Kim MJ, Kim KW. Metal artifact reduction software used with abdominopelvic dual-energy CT of patients with metal hip prostheses: assessment of image quality and clinical feasibility. *AJR Am J Roentgenol* 2014;203(4):788–95. <https://doi.org/10.2214/AJR.13.10980>.
- [18] Bamberg F, Diersk A, Nikolaou K, Reiser MF, Becker CR, Johnson TR. Metal artifact reduction by dual energy computed tomography using monoenergetic extrapolation. *Eur Radiol* 2011;21(7):1424–9. <https://doi.org/10.1007/s00330-011-2062-1>.
- [19] Wellenberg RH, Boomsma MF, van Osch JA, et al. Quantifying metal artefact reduction using virtual monochromatic dual-layer detector spectral CT imaging in unilateral and bilateral total hip prostheses. *Eur J Radiol* 2017;88:61–70. <https://doi.org/10.1016/j.ejrad.2017.01.002>.
- [20] Lewis M, Reid K, Toma AP. Reducing the effects of metal artefact using high keV monoenergetic reconstruction of dual energy CT (DECT) in hip replacements. *Skeletal Radiol* 2013;42:275–82. <https://doi.org/10.1007/s00256-012-1458-6>.
- [21] Kuchenbecker S, Faby S, Sawall S, Lell M, Kachelrieß M. Dual energy CT: how well can pseudomonochromatic imaging reduce metal artifacts? *Med Phys* 2015;42:1023–36. <https://doi.org/10.1118/1.4905106>.
- [22] Zhou C, Zhao YE, Luo S, Shi H, Li L, Zheng L, et al. Monoenergetic imaging of dual-energy CT reduces artifacts from implanted metal orthopedic devices in patients with fractures. *Acad Radiol* 2011;18(10):1252–7. <https://doi.org/10.1016/j.acra.2011.05.009>.
- [23] Subhas N, Primak AN, Obuchowski NA, Gupta A, Polster JM, Krauss A, et al. Iterative metal artifact reduction: evaluation and optimization of technique. *Skeletal Radiol* 2014;43(12):1729–35. <https://doi.org/10.1007/s00256-014-1987-2>.
- [24] Axente M, Paidi A, Von Eyben R, Zeng C, Bani-Hashemi A, Krauss A, et al. Clinical evaluation of the iterative metal artifact reduction algorithm for CT simulation in radiotherapy. *Med Phys* 2015;42(3):1170–83. <https://doi.org/10.1118/1.4906245>.
- [25] Morsbach F, Bickelhaupt S, Wanner GA, Krauss A, Schmidt B, Alkadhi H. Reduction of metal artifacts from hip prostheses on CT images of the pelvis: value of iterative reconstructions. *Radiology* 2013;268(1):237–44. <https://doi.org/10.1148/radiol.13122089>.
- [26] Kim YJ, Cha JG, Kim H, Yi JS, Kim HJ. Dual-energy and iterative metal artifact reduction for reducing artifacts due to metallic hardware: a loosening hip phantom study. *AJR Am J Roentgenol* 2019;5(1–6). <https://doi.org/10.2214/AJR.18.20413>.
- [27] Lim P, Barber J, Sykes J. Evaluation of dual energy CT and iterative metal artefact reduction (iMAR) for artefact reduction in radiation therapy. *Australas Phys Eng Sci Med* 2019;42:1025–32. <https://doi.org/10.1007/s13246-019-00801-1>.
- [28] Javan R, Bansal M, Tangestanipoor A. A prototype hybrid gypsum-based 3-dimensional printed training model for computed tomography-guided spinal pain management. *J Comput Assist Tomogr* 2016;40(4):626–31. <https://doi.org/10.1097/RCT.0000000000000415>.
- [29] Niebuhr NI, Johnen W, Gündaglar T, Runz A, Echner G, Mann P, et al. Technical Note: radiological properties of tissue surrogates used in a multimodality deformable pelvic phantom for MR-guided radiotherapy. *Med Phys* 2016;43(2):908–16. <https://doi.org/10.1118/1.4939874>.
- [30] Hazelar C, Van Eijndhoven M, Dahele M, Wolff J, Forouzanfar T, Slotman B, et al. Using 3D printing techniques to create an Anthropomorphic thorax phantom for medical imaging purposes. *Med Phys* 2018;45(1):92–100. <https://doi.org/10.1002/mp.12644>.
- [31] Followill DS, Evans DR, Cherry C, Molineu A, Fisher G, Hanson WF, et al. Design, development, and implementation of the radiological physics center's pelvis and thorax anthropomorphic quality assurance phantoms. *Med Phys* 2007;34(6):2070–6. <https://doi.org/10.1118/1.2737158>.
- [32] Ingrosso G, Miceli R, Ponti E, Lancia A, di Cristino D, de Pasquale F, et al. Interfraction prostate displacement during image-guided radiotherapy using intraprostatic fiducial markers and a cone-beam computed tomography system: a volumetric off-line analysis in relation to the variations of rectal and bladder volumes. *J Can Res Ther* 2019;15:69–75. [https://doi.org/10.4103/jcrt.JCRT\\_463\\_17](https://doi.org/10.4103/jcrt.JCRT_463_17).
- [33] Filella X, Foj L, Alcover J, Augé JM, Molina R, Jiménez W. The influence of prostate volume in prostate health index performance in patients with total PSA lower than 10 µg/L. *Clin Chim Acta* 2014;436:303–7. <https://doi.org/10.1016/j.cca.2014.06.019>.
- [34] Coolens C, Childs PJ. Calibration of CT Hounsfield units for radiotherapy treatment planning of patients with metallic hip prostheses: the use of the extended CT-scale. *Phys Med Biol* 2003;48:1591–603. <https://doi.org/10.1088/0031-9155/48/11/308>.
- [35] Jeong S, Kim SH, Hwang EJ, Shin C, Han JK, Choi BI. Usefulness of a metal artifact reduction algorithm for orthopedic implants in abdominal CT: phantom and clinical study results. *AJR Am J Roentgenol* 2015;204(2):307–17. <https://doi.org/10.2214/AJR.14.12745>.
- [36] Piotrowski T, Rodrigues G, Bajon T, Yartsev S. Method for data analysis in different institutions: example of image guidance of prostate cancer patients. *Phys Med* 2014;30:249–51. <https://doi.org/10.1016/j.ejmp.2013.05.001>.



OPEN

## Accuracy of the doses computed by the Eclipse treatment planning system near and inside metal elements

Bartosz Pawałowski<sup>1,2</sup>, Adam Ryczkowski<sup>1,3</sup>, Rafał Panek<sup>4,5</sup>, Urszula Sobocka-Kurdyk<sup>1,6</sup>, Kinga Graczyk<sup>1</sup> & Tomasz Piotrowski<sup>1,3</sup>✉

Metal artefacts degrade clinical image quality which decreases the confidence of using computed tomography (CT) for the delineation of key structures for treatment planning and leads to dose errors in affected areas. In this work, we investigated accuracy of doses computed by the Eclipse treatment planning system near and inside metallic elements for two different computation algorithms. An impact of CT metal artefact reduction methods on the resulting calculated doses has also been assessed. A water phantom including Gafchromic film and metal inserts was irradiated (max dose 5 Gy) using a 6 MV photon beam. Three materials were tested: titanium, alloy 600, and tungsten. The phantom CT images were obtained with the pseudo-monoenergetic reconstruction (PMR) and the iterative metal artefact reduction (iMAR). Image sets were used for dose calculation using an Eclipse treatment planning station (TPS). Monte Carlo (MC) simulations were used to predict the true dose distribution in the phantom allowing for comparison with doses measured by film and calculated by TPS. Measured and simulated percentage depth doses (PDDs) were not statistically different ( $p > 0.618$ ). Regional differences were observed at edges of metallic objects (max 8% difference). However, PDDs simulated with and without film were statistically different ( $p < 0.002$ ). PDDs calculated by the Acuros XB algorithm based on the dose-to-medium approach best matched the MC reference regardless of the CT reconstruction methods and inserts used ( $p > 0.078$ ). PDDs obtained using other algorithms significantly differ from the MC values ( $p < 0.011$ ). The Acuros XB algorithm with a dose-to-medium approach provides reliable dose calculation in all metal regions when using the Varian system. The inability of the AAA algorithm to model backscatter dose significantly limits its clinical application in the presence of metal. No significant impact on the dose calculation was found for a range of metal artefact reduction strategies.

An increasing number of patients with metallic implants are treated with radiotherapy and so it is important to better understand the impact of these elements on the treatment process. The proximity of a metal object causes streaking image artefacts observed in the computed tomography (CT) scans deteriorating diagnostic quality and ability to confidently delineate structures such as organs at risk and tumours<sup>1–3</sup>. Misrepresentation of CT numbers can also cause errors in calculated linear attenuation coefficients leading to significant errors in dose calculation in affected areas<sup>4</sup>. The simple density override method, covering the affected area by contour with manually corrected CT numbers, can reduce the dose calculation error<sup>5</sup>. However, this method doesn't improve visualization of areas affected by artefacts, which is important for accurate delineation of anatomical structures. Several metal artefact reduction methods were proposed, such as the iterative metal artefact reduction (iMAR) algorithm<sup>6–8</sup>, the dual-energy method (enabling the pseudo-monoenergetic reconstruction (PMR) of CT images created for specified photon energy)<sup>9</sup>, and a unique technique based on the use of megavoltage CT imaging on the tomotherapy units<sup>10,11</sup>. Combinations of PMR and iMAR methods have been previously investigated and demonstrates significant reduction of metal artefacts and low CT number errors observed in the vicinity of dense

<sup>1</sup>Department of Medical Physics, Greater Poland Cancer Centre, Garbary 15, 61-866 Poznan, Poland. <sup>2</sup>Department of Technical Physics, Poznan University of Technology, Poznan, Poland. <sup>3</sup>Department of Electroradiology, Poznan University of Medical Sciences, Poznan, Poland. <sup>4</sup>Medical Physics and Clinical Engineering, Nottingham University Hospitals NHS Trust, Nottingham, UK. <sup>5</sup>School of Medicine, University of Nottingham, Nottingham, UK. <sup>6</sup>Faculty of Health Sciences, Calisia University, Kalisz, Poland. ✉email: tomasz.piotrowski@me.com

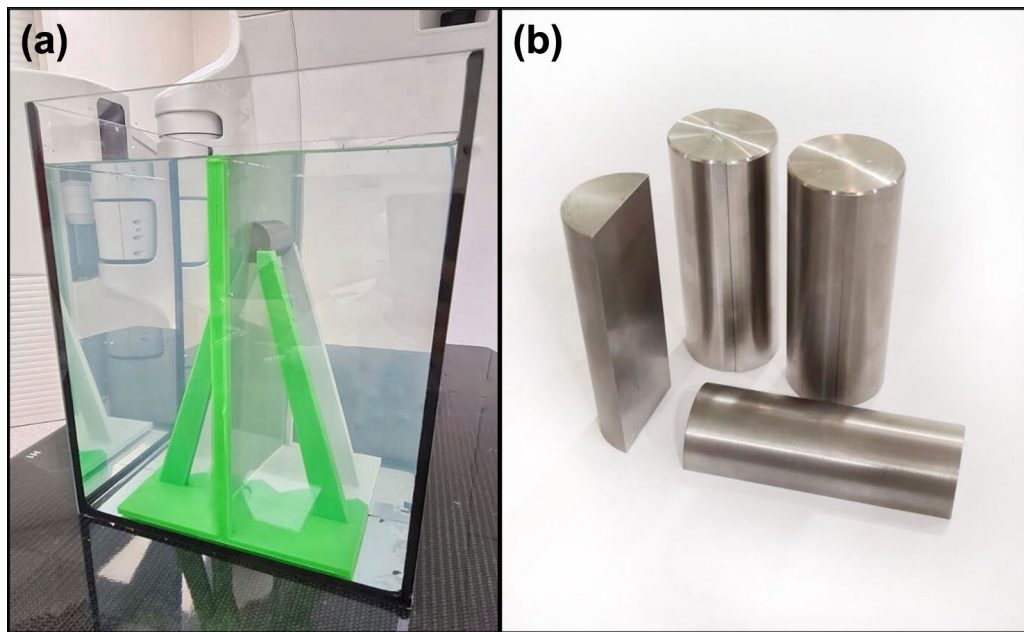


**Figure 1.** (a) A photograph of the water phantom with submerged holder made in 3D printing technology for a Gafchromic film and metallic inserts. (b) A cut in a half metal insert made of titanium, alloy 600 and tungsten used in this study.

materials<sup>12</sup>. Besides errors due to the presence of artefacts, there is also doubt related to the precision of dose calculation in the presence of high-density materials<sup>13</sup>. These metal elements lead to higher beam attenuations and reveal interface phenomena caused by backscatter radiation<sup>14</sup>. For precise dose calculation, these perturbations have to be accounted for. Currently, only algorithms utilising the medium for dose transport and calculation can model this accurately<sup>15</sup>. However, there is still a lack of comprehensive analysis of different metal artefact reduction methods and their impact on algorithms used for dose calculations. Many authors verified the impact of metals on the radiotherapy process, however, most of them used only one metal which can be insufficient for understanding the behaviour of the algorithms and their limitations<sup>16–18</sup>. Our work focused on obtaining a Monte Carlo validated simulation of three metals with different, clinically relevant densities and comparing them with different dose algorithm calculations using a range of MAR methods. In particular, we assess: (1) the accuracy of dose computation using Acuros XB and AAA (analytical anisotropic algorithm) calculation algorithms near and inside the metal structures, and (2) the impact of different methods for metal artefact reduction in CT on the accuracy of doses computed through these algorithms.

## Materials and methods

**Dose measurements.** A  $25 \times 25 \times 30 \text{ cm}^3$  water phantom with holder for Gafchromic film and metal inserts was fabricated (Fig. 1a). A 3D printed holder was designed to allow for the placement of the Gafchromic film parallel to the beam axis and to fix the removable cylindrical inserts at a precisely defined depth. The distance between the top edge of the Gafchromic film and the center of the insert was 5 cm.

Specific information about phantom components:

- (1) Phantom holder: Original Prusa i3 MK3S + 3D printer (Prusa Research; Prague, Czech Republic) was used to print the phantom holder in fused deposition modeling technology with polylactic acid filament<sup>19,20</sup>.
- (2) Inserts: The cylindrical inserts (2.8 cm diameter and 7 cm length), consisting of two halves (Fig. 1b), were made from three high-density materials: titanium, alloy 600, and tungsten with physical densities of 4.5, 8.5, and 19.4 g/cm<sup>3</sup>, respectively<sup>12</sup>. The dimensions of inserts allowed to position them in both dosimetric and CT calibration (Virtual Water™, described below) phantoms.
- (3) Film: Self-evoking EBT3 Gafchromic films (Ashland Inc., Wilmington, Delaware, USA). The films are made of an active layer with a thickness of 28 µm, located between two layers of matte-polyester substrates with a thickness of 125 µm. These films allow to measure the doses (optimal range from 0.2 to 10 Gy) obtained by radiation beams with energies ranging from 100 to 18 MeV. The film's response is independent of temperature, atmospheric pressure, and the direction of the irradiation beam<sup>21,22</sup>. To avoid delamination and the water immersion effect, whole EBT3 sheets (20.3 cm × 25.4 cm) were placed in the 3D printed watertight holder.

The phantom including EBT3 film insert was filled with water up to the top edge of the film (Fig. 1a) and positioned on the accelerator couch. The source to phantom water surface distance, SPD, was 100 cm for all measurements. Central-axis percentage depth doses (PDD) were measured and simulated for a 6 MV photon

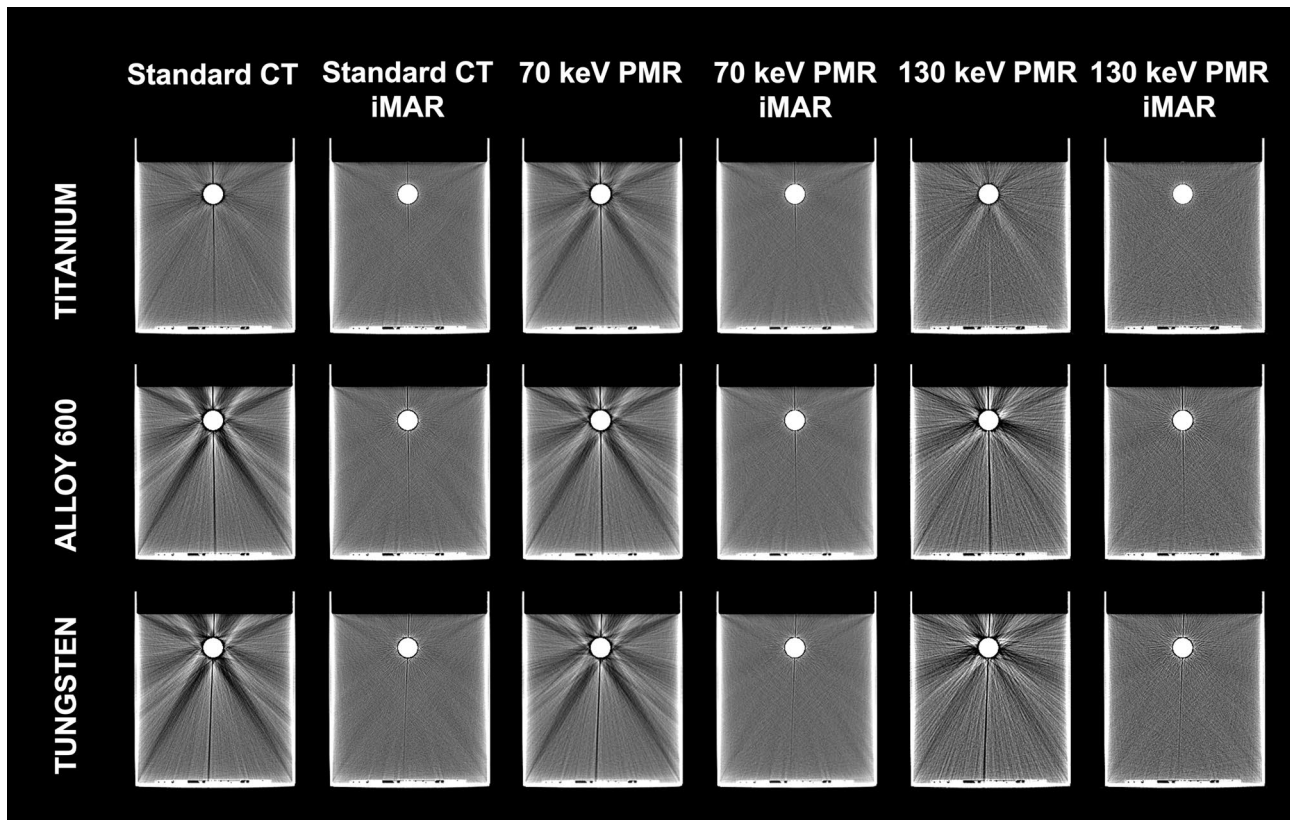


**Figure 2.** CT images of the phantom with titanium, alloy 600, and tungsten inserts obtained using a range of reconstruction modes. *PMR* pseudo-monoenergetic reconstruction, *iMAR* iterative metal artefact reconstruction.

beam produced by the TrueBeam accelerator (Varian Medical Systems, Palo Alto, USA). Films were irradiated with a dose of 5 Gy defined at the point of maximum dose located at 15 mm below water surface. The beam field size was 10 cm × 10 cm oriented perpendicular to the water surface and the central axis (CAX) of the beam was in the middle of the film.

For the dose calibration curve, EBT3 film was cut into nine pieces (3 cm × 3 cm) and irradiated with a photon beam (10 cm × 10 cm, 6 MV) in ranges from 1 to 10 Gy.

The films were scanned 30 h after being irradiated using the Epson Perfection 750 Pro scanner (Seiko Epson Corporation, Japan) with the following parameters: no color correction, transmission mode, portrait orientation, 48-bit Red–Green–Blue (RGB)<sup>23</sup>. The scan resolution was 72 dpi for calibration and measurements. Scans were then analysed using Film Analyze 1.8 (PTW Freiburg, Freiburg, Germany; single red channel analysis from RGB).

**Dose calculations.** The phantom images were acquired using a Somatom Definition AS scanner (Siemens Medical Solution, Erlangen, Germany). Two sets of CT images were obtained: (1) standard CT pelvis protocol (120 kV, 270 mAs, 0.6 pitch, 64 × 0.6 mm acquisition, 3 mm slice thickness, 2.0 mm increment, kernel B30s, extended CT scale) and (2) a dual-energy mode based on the two consecutive scan technique (first/second scan: 80 kV, 540 mAs/140 kV, 128 mAs; 0.6 pitch, 64 × 0.6 mm acquisition, 3 mm slice thickness, 2.0 mm increment, kernel B30f, extended CT scale) and used to obtain 70 and 130 keV PMR sets. The standard CT and 70 and 130 keV PMRs were reconstructed twice for each insert: once with and once without the iMAR algorithm (Siemens Medical Solution, Erlangen, Germany) (Fig. 2).

Eclipse v.16.0 (Varian Medical Systems, Palo Alto, USA) treatment planning system (TPS) was used in the study. The doses for each plan (each CT reconstruction) were normalised to the maximum depth and calculated by two available options: Acuros XB v.16.1.0 and AAA (i.e., analytical anisotropic algorithm) v.16.1.0 algorithms. In the case of Acuros XB calculations, two approaches: dose-to-medium and dose-to-water were considered. AAA calculations were based on CT density calculated by CT scanner and real CT value estimated from density. The spatial resolution of 1 mm was used for all calculations.

Six energy-dependent conversion curves (i.e., for each energy of CT reconstruction and for each class of calculation algorithm) were prepared for dose calculations. The curves were obtained using Virtual Water™ phantom (Gammex RMI, Middleton, WI, USA), with various inserts and different tissue densities<sup>12</sup>. The Virtual Water™ phantom was scanned using the same parameters as for the water phantom. Images were reconstructed for standard CT, 70 keV PMR, and 130 keV PMR series.

The segment high-density material option, available in the Eclipse TPS, was used for the insert contouring purposes. This tool finds and outlines structures with mass densities larger than 3 g/cm<sup>3</sup>. For the AAA algorithm,

three energy-dependent CT numbers to electron density conversion curves relative to water were obtained. The whole range of CT numbers reconstructed in the insert during imaging was used for dose calculation by the AAA approach based on CT density. The real CT approach, used for dose calculation, manually overrides the value of the CT number with the mean value from the whole range of CT numbers detected in the insert. Conversion curves were also calculated for Acuros XB. The Acuros XB-13.5 material table was used for the Acuros material assignment including titanium alloy (titanium insert), stainless steel (alloy 600), and gold (tungsten). Tungsten material is not currently available for Acuros XB, and gold was used instead due to its comparable density (19.3 g/cm<sup>3</sup> and 19.4 g/cm<sup>3</sup> for gold and tungsten respectively).

**Monte Carlo simulations.** The Geant4 toolkit v.10.05.p01 was used for the Monte Carlo (MC) simulation of the dose distribution in our phantom for each insert (parallel computations, 5 dual Xeon processors, 32 GB RAM each). As a primary generator, data from phase space files provided by Varian were used<sup>24</sup>. Fifty-five files for the 6 MV photon beam were used in total, each one was iterated twenty times. Two phantom configurations were modelled for dose calculations: (1) MC<sub>mea</sub> with the information of dose deposited in the film corresponding to the measurement condition in the water-filled phantom with the EBT3 film placed between the two halves of the insert, and (2) MC<sub>pla</sub> corresponding to dose calculation in Eclipse TPS without the film present. For MC<sub>pla</sub>, the information of dose deposition, unlike MC<sub>mea</sub>, was not collected for the film but in water and the insert. Simulations in both configurations were performed under the same conditions matching experimental irradiation conditions described earlier.

**Data analysis.** The PDDs obtained from direct measurements, MC simulations, and Eclipse TPS calculations were compared on depths ranging from 15 to 85 mm, where 0 mm corresponds to the water surface. In particular, the PDDs comparisons were made between: (1) experimental, measured (EBT3) versus simulated MC<sub>mea</sub> (validation of MC simulated PDD), (2) MC<sub>mea</sub> versus MC<sub>pla</sub> (influence of film on PDD) and (3) MC<sub>pla</sub> versus Eclipse TPS (comparison of MC simulated and TPS calculated PDDs for different algorithms and for different reconstruction methods).

The comparison was made in five regions:

1. water in front of the insert (15–34 mm),
2. input edge of the insert ± 2 mm (34–38 mm),
3. the insert (38–62 mm),
4. output edge of the insert ± 2 mm (62–66 mm),
5. water behind the insert (66–85 mm).

Mean dose differences were calculated for all regions and PDDs. Kolmogorov–Smirnov and Pearson tests were used to test differences between means and correlations with a 0.05 significance level.

## Results

**EBT3 film measurements versus MC<sub>mea</sub> comparison.** Measured PDDs agree well with those simulated for every insert (Fig. 3) with mean PDD values strongly correlated and not statistically different ( $p > 0.618$ ,  $R > 0.998$ ) (Table 1). Regional analysis show that the highest differences between measured and simulated doses were observed in the regions of insert edges. The maximum difference was 8% and was detected for the input edge of the tungsten insert (Fig. 3). The highest mean differences were seen on the input (3%) and output (− 3%) edges of alloy 600 insert (Table 1). In other regions, the maximum differences were within ± 2%, and the mean differences were lower than 1% for every insert.

**MC<sub>mea</sub> versus MC<sub>pla</sub> comparison.** The PDDs simulated for measurement condition, MC<sub>mea</sub>, significantly differ from those simulated for TPS condition, MC<sub>pla</sub> ( $p < 0.002$ ) (Fig. 4a). The PDD values in the insert region for MC<sub>pla</sub> (Fig. 4c) were on average lower by 23% (titanium), 26% (alloy 600), and 37% (tungsten) than corresponding MC<sub>mea</sub> values (Fig. 4b). In the region behind the insert, PDDs from MC<sub>pla</sub> were on average lower by 4% (titanium), 7% (alloy 600), and 12% (tungsten) than PDDs from MC<sub>mea</sub>.

**MC<sub>pla</sub> versus TPS comparison.** The best match to the MC<sub>pla</sub> PDDs was observed for the PDDs calculated by the Acuros XB algorithm based on the dose-to-medium approach (AXB<sub>DM</sub>) (Fig. 5). PDDs obtained from AXB<sub>DM</sub> calculations were similar to MC<sub>pla</sub> PDDs regardless of the CT reconstruction methods and inserts used ( $p > 0.078$ ,  $R > 0.987$ ) (Table 2). In contrast, PDDs obtained using other algorithms significantly differ from the MC<sub>pla</sub> PDD ( $p < 0.011$ ).

The PDDs calculated by the Acuros XB algorithm based on the dose-to-water approach (AXB<sub>DW</sub>) was grossly overestimated in the insert region. The mean dose differences between the AXB<sub>DW</sub> and the MC<sub>pla</sub> PDDs in this region, depending on CT reconstruction mode, ranged from 43.6 to 45.0% for titanium, 43.0 to 45.6% for alloy 600, and 61.1 to 62.5% for tungsten. In the water regions (both in front and behind the inserts) the mean dose differences between AXB<sub>DW</sub> and the MC<sub>pla</sub> PDDs were lower than 2% for each CT reconstruction mode. The PDDs obtained from AAA calculations are more comparable to the MC<sub>pla</sub> for the true density (AAA<sub>TD</sub>) than for the CT density (AAA<sub>CT</sub>) based approach (Fig. 5). In the region in front of the insert, both approaches of AAA dose calculations agree with MC<sub>pla</sub> (differences < 2%). In the input/output edge of the insert due to lack of backscattered radiation, the differences between MC<sub>pla</sub> simulation and doses calculated by both AAA methods were, respectively, up to 10% for titanium, 15% for alloy 600, and 50% for tungsten. In the region behind the

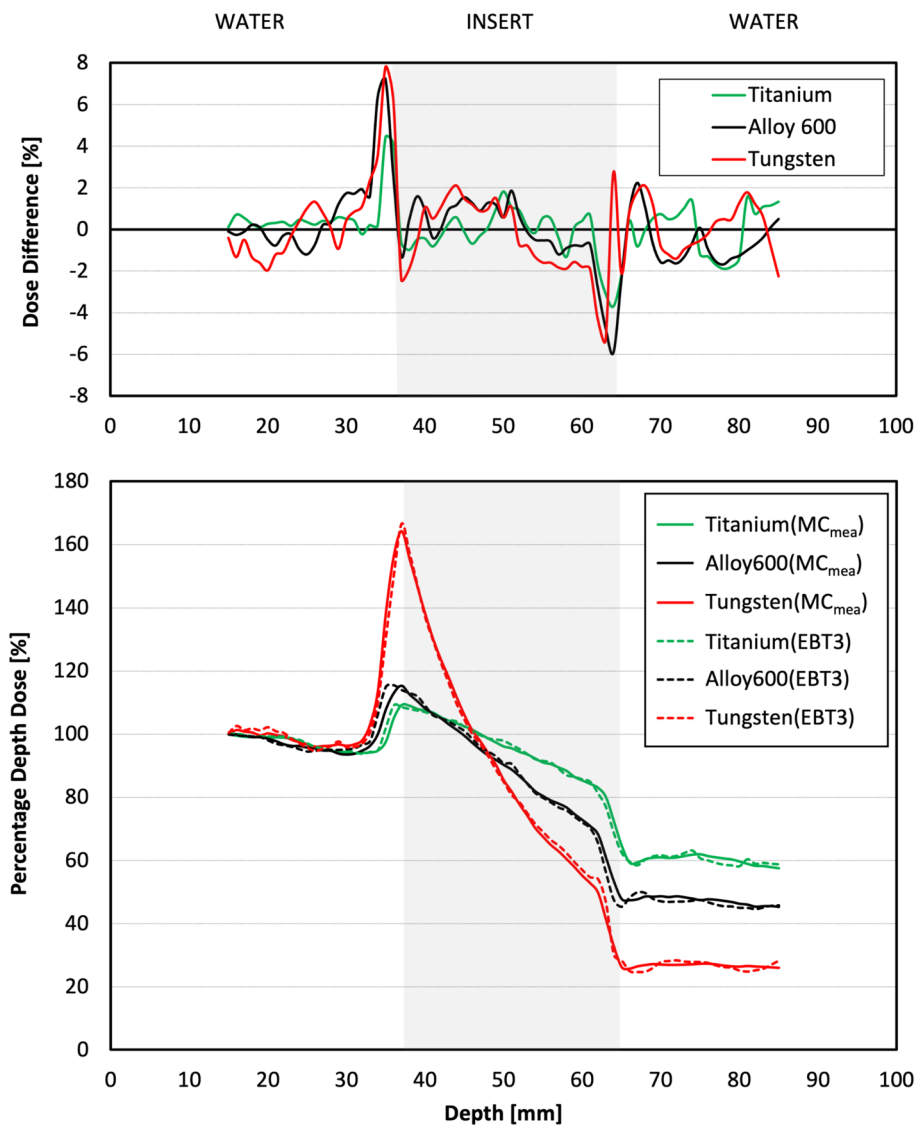


**Figure 3.** The comparison of dose differences and PDDs for measured (EBT3) and simulated ( $MC_{mea}$ ) PDDs for titanium, alloy 600, and tungsten inserts.

|   | Titanium   | Alloy 600  | Tungsten   |
|---|------------|------------|------------|
| <b>Mean dose difference (and standard deviation) [%]</b>      |            |            |            |
| Water in front of the insert                                  | 0.3 (0.3)  | 0.2 (1.0)  | -0.1 (1.2) |
| Input edge of the insert ( $\pm 2$ mm)                        | 1.4 (2.6)  | 3.0 (3.7)  | 2.6 (4.6)  |
| The insert  | 0.1 (0.7)  | 0.3 (1.0)  | -0.1 (1.4) |
| Output edge of the insert ( $\pm 2$ mm)                       | -2.1 (1.6) | -3.0 (2.6) | -1.6 (3.4) |
| Water behind the insert                                       | 0.0 (1.2)  | -0.6 (1.0) | 0.1 (1.2)  |
| <b>Comparison of whole PDDs (from 15 to 85 mm)</b>            |            |            |            |
| Similarity of distribution ( <i>Kolmogorov-Smirnov test</i> ) | $p=0.962$  | $p=0.758$  | $p=0.618$  |
| Coefficient of correlation ( <i>Pearson corelation test</i> ) | R=0.998    | R=0.998    | R=0.999    |

**Table 1.** Measured (EBT3) and simulated ( $MC_{mea}$ ; Monte Carlo; measurement conditions) percentage depth doses, and mean dose difference (EBT3— $MC_{mea}$ ) for selected regions.

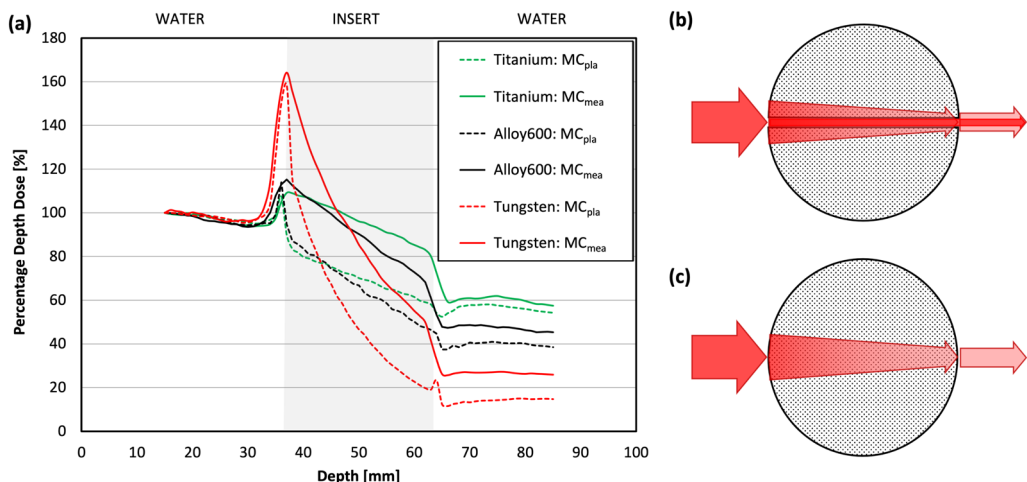


**Figure 4.** (a) The comparison of PDDs obtained from Monte Carlo simulations performed for measurement ( $MC_{mea}$ ) and TPS conditions ( $MC_{pla}$ ) for titanium, alloy 600, and tungsten inserts. Visualisation of the insert geometry, (b) two halves of the grey circle with a film gap between them ( $MC_{mea}$  conditions) and (c) solid grey circle without film gap ( $MC_{pla}$  conditions). The red arrows visible in (b) and (c) represent the radiation beam.

insert better agreement to  $MC_{pla}$  was observed for  $AAA_{TD}$  than for  $AAA_{CT}$ . The mean differences for  $AAA_{TD}$  versus  $MC_{pla}$  and  $AAA_{CT}$  versus  $MC_{pla}$  were, respectively, up to 1% and 3.5% for titanium; 2% and 10% for alloy 600; and 7.5% and 36% for tungsten. In the insert region, the mean differences between  $AAA_{TD}$  versus  $MC_{pla}$  were lower than  $AAA_{CT}$  versus  $MC_{pla}$  and were, respectively, up to 11% and 12% for titanium; 9% and 15% for alloy 600; and 6% and 25% for tungsten.

Figure 6 shows the differences between  $MC_{pla}$  and  $AXB_{DM}$  PDDs obtained from calculations on different CT reconstructions for titanium, alloy 600, and tungsten inserts.

The highest differences between the  $MC_{pla}$  and the  $AXB_{DM}$  PDDs related to different CT reconstructions were observed at insert edges and they ranged from 4 to – 2% for titanium, 16% to – 9.5% for alloy 600, and 16% to – 15% for tungsten (Fig. 6). For the input edge regions standard deviations ranged from 1.5 to 2.0% for titanium, 3.6 to 8.9% for alloy 600, and 11.4 to 17.3% for tungsten (Table 2). In regions in-front and behind the insert, differences between the  $MC_{pla}$  and the  $AXB_{DM}$  PDDs were up to 2% (Fig. 6). The differences in the insert region depended on the density of the insert and were the lowest (up to 3%) for the titanium ( $4.5\text{ g/cm}^3$ ) and the highest (up to 12%) for the tungsten ( $19.4\text{ g/cm}^3$ ). Different CT reconstruction methods lead to differences between  $AXB_{DM}$  PDDs in all compartments ranging up to 2%. Nevertheless, there is no clear superiority of one method of reconstruction over the others (Fig. 6).

All sets of PDD curves calculated using different algorithms, CT reconstructions and inserts are presented in a supplementary material.

## Discussion

Several studies show that both algorithms (AAA and AXB) could accurately calculate the doses near the metal<sup>25–27</sup>. However, these studies focus specifically on spine SBRT (stereotactic body radiation therapy) treatment in the presence of titanium screws. Due to the relatively small dimensions of the screws and titanium density, the dose calculated in the tissues surrounding the screws is in line with measurements. Our results are in line with these observations, the doses calculated by AAA and AXB algorithms in the water near the titanium insert are close to MC simulations (Fig. 5). Nevertheless, there may be metal structures with a higher density than titanium in the patient body and geometries larger than screws used for spine stabilisation<sup>13,16,28</sup>. In general, to check accuracy between calculations and measurements, the ionising chambers or EBT films for in-axis dose measurements in front and behind the metal inserts and the perpendicularly oriented to the axis EBT films for profile measurements were used. Our study focused specifically on in-axis percentage depth dose measurements and calculations. In addition to previous studies, the EBT3 film placement in our phantom allows to simulate measurement conditions inside metal inserts. We recognise that the EBT3 films between the insert's halves resulted in measurements in a thin gap (< 0.3 mm) between parts of the insert filled by the film, rather than inside of the insert. Due to scanning modes used and the film thickness, the gap between the insert halves was not visible on the reconstructed CT images. Even with the smallest possible grid for dose calculation in TPS, the grid size was three times larger than the film thickness and the TPS calculations do not take into account the gap in the insert. Therefore, the measured doses by film were used only to compare to MC simulations for measurement conditions to prove the accuracy of MC simulations. The percentage depth doses obtained from MC simulation for TPS conditions (without the gap) were used as reference data for TPS calculations.

Analysing the accuracy of dose calculation through different algorithms shows the superiority of Acuros XB algorithm based on dose-to-medium approach over the other calculation methods in agreement with previous studies<sup>16,29,30</sup>. Another option of dose reporting mode in Acuros XB, dose-to-water, was also evaluated.

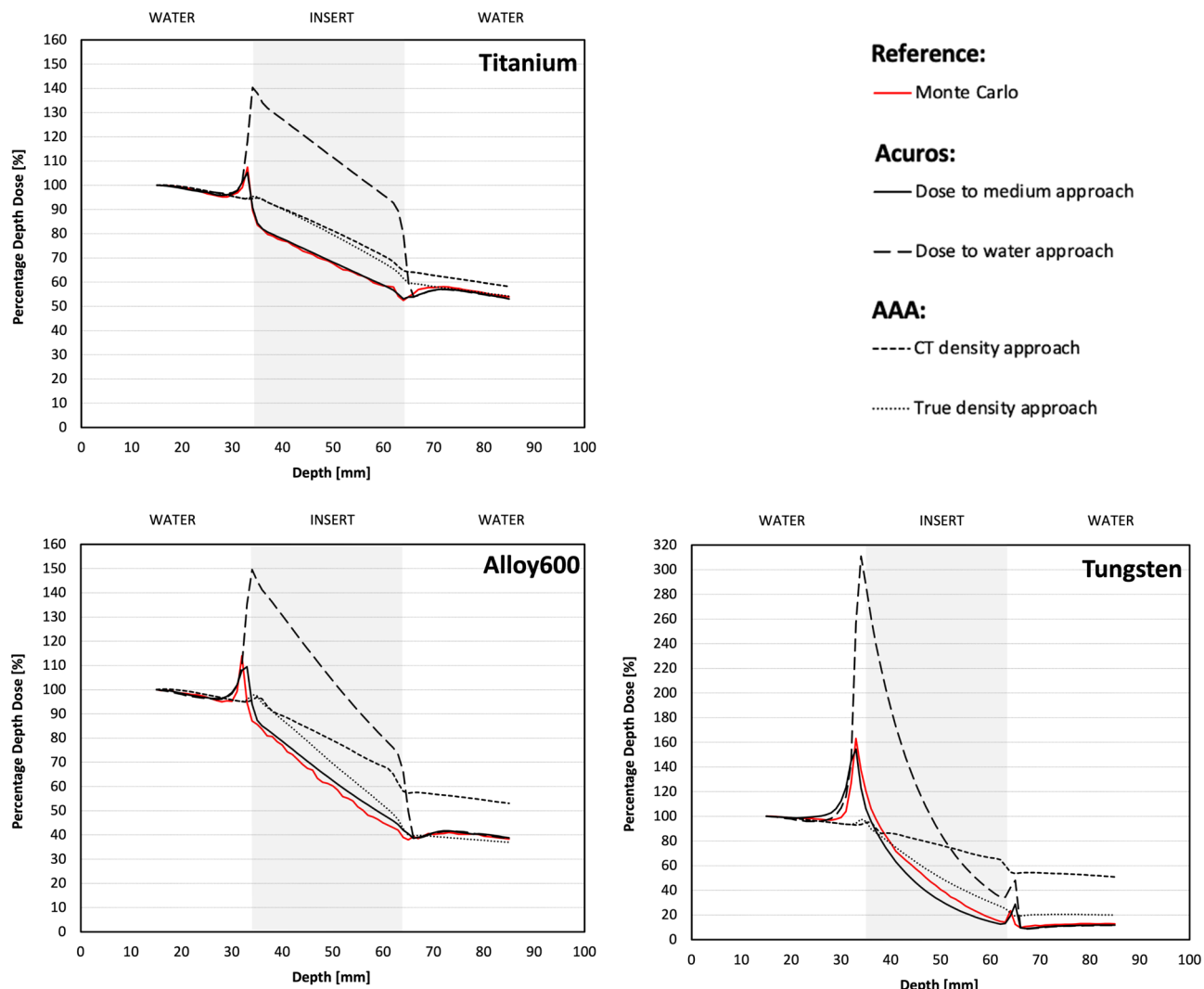


**Figure 5.** The comparison between PDDs obtained from Monte Carlo simulations performed for TPS condition (red line) and PDDs obtained from TPS calculations on standard CT reconstruction using different algorithms for titanium, alloy 600, and tungsten inserts.

Both approaches (dose-to-medium and dose-to-water) calculate the energy-dependent electron fluence based on the material properties of the interested media. Both approaches are based on the same steps of transport calculation<sup>31</sup>. The difference occurs in the post-processing step, during which the energy-dependent fluence resulting from transport calculation is multiplied by the different flux-to-dose response functions to obtain the absorbed dose value. Acuros XB uses a medium-based response function for dose-to-medium and a water-based response function for dose-to-water<sup>32</sup>. While our findings show comparable results of dose calculation around the insert for both Acuros XB approaches, the dose-to-water approach overestimates dose inside the inserts. The weak point of Acuros XB dose-to-medium approach is the rigid and non-modifiable list of high-density materials for which calculations can be made. In addition to previous studies, we performed calculations not only for titanium and stainless steel (i.e., alloy 600 in our study) but also for tungsten that is not listed in the algorithm's libraries. In order to perform calculations, we applied for the tungsten insert the closest density-similar material listed in the library, i.e., gold ( $19.3 \text{ g/cm}^3$ ). The Monte Carlo simulations were performed for real tungsten density, i.e.,  $19.4 \text{ g/cm}^3$ . Therefore, the differences between the calculated and simulated doses in the tungsten insert are bigger than for the other inserts.

The worst results were observed for the AAA algorithm, which is in line with previous research<sup>17</sup>. The main limitation of this algorithm is the inability to model backscatter radiation deriving from high-density materials. This radiation generates a dose peak observed at the entrance to high-density material. Our work shows that only Monte Carlo and Acuros XB correctly model this phenomenon. However, it is worth noting that assigning an estimated one CT value for the metal ( $\text{AAA}_{\text{TD}}$ ) over the CT values calculated by the CT ( $\text{AAA}_{\text{CT}}$ ) scanner led to a better agreement with MC simulations.

This work also verified different strategies for metal artefact reduction. We assessed six different imaging methods: standard CT, monoenergetic CTs series reconstructed for 70 keV and 130 keV with and without the

| Insert  | Titanium    |              |              |             |             |              |
|---|-------------|--------------|--------------|-------------|-------------|--------------|
| Reconstruction  | Standard CT |              | 70 keV PMR   |             | 130 keV PMR |              |
| Iterative metal artefact reduction                                      | NO          | YES          | NO           | YES         | NO          | YES          |
| <b>Mean dose difference (and standard deviation) in compartments[%]</b> |             |              |              |             |             |              |
| Water in front the insert   | 0.0 (0.4)   | 0.8 (0.6)    | 0.3 (0.6)    | 0.1 (0.7)   | 0.4 (1.1)   | 0.6 (0.8)    |
| Input edge of the insert ( $\pm 2$ mm)                                  | 0.6 (1.7)   | 1.3 (1.8)    | 1.4 (1.6)    | 1.1 (1.5)   | 2.2 (1.6)   | 1.8 (2.0)    |
| The insert  | 0.5 (0.5)   | 1.7 (0.6)    | 0.8 (0.5)    | 1.4 (0.5)   | 1.8 (0.6)   | 2.4 (0.6)    |
| Output edge of the insert ( $\pm 2$ mm)                                 | - 1.0 (1.2) | 0.6 (1.3)    | - 0.7 (1.3)  | 0.2 (1.5)   | 0.0 (1.7)   | 0.8 (1.4)    |
| Water behind the insert   | - 0.7 (0.3) | - 0.4 (0.3)  | - 0.7 (0.3)  | - 0.7 (0.3) | - 0.4 (0.2) | - 0.5 (0.2)  |
| <b>Comparison of whole PDDs (from 15 to 85 mm)</b>                      |             |              |              |             |             |              |
| Similarity of distribution (Kolmogorov-Smirnov test)                    | p=0.618     | p=0.962      | p=0.880      | p=0.758     | p=0.882     | p=0.960      |
| Coefficient of correlation (Pearson corelation test)                    | R=0.999     | R=0.998      | R=0.999      | R=0.998     | R=0.997     | R=0.997      |
| Insert  | Alloy 600   |              |              |             |             |              |
| Reconstruction  | Standard CT |              | 70 keV PMR   |             | 130 keV PMR |              |
| Iterative metal artefact reduction                                      | NO          | YES          | NO           | YES         | NO          | YES          |
| <b>Mean dose difference (and standard deviation) in compartments[%]</b> |             |              |              |             |             |              |
| Water in front the insert   | 0.4 (1.1)   | 0.5 (0.8)    | 1.3 (0.9)    | 1.1 (0.8)   | 0.9 (1.2)   | 0.9 (1.2)    |
| Input edge of the insert ( $\pm 2$ mm)                                  | 4.0 (7.6)   | 2.8 (8.5)    | 4.5 (8.4)    | 3.2 (8.9)   | - 1.1 (4.7) | - 0.1 (3.6)  |
| The insert  | 2.8 (0.8)   | 2.9 (0.8)    | 3.6 (0.7)    | 3.6 (0.7)   | 1.4 (0.9)   | 2.0 (0.9)    |
| Output edge of the insert ( $\pm 2$ mm)                                 | 1.0 (1.6)   | 2.2 (1.3)    | 1.7 (1.7)    | 2.5 (1.4)   | 0.7 (1.2)   | 1.8 (1.2)    |
| Water behind the insert   | 0.6 (0.4)   | 0.4 (0.3)    | 1.3 (0.3)    | 0.9 (0.3)   | - 0.3 (0.2) | 0.1 (0.3)    |
| <b>Comparison of whole PDDs (from 15 to 85 mm)</b>                      |             |              |              |             |             |              |
| Similarity of distribution (Kolmogorov-Smirnov test)                    | p=0.880     | p=0.618      | p=0.185      | p=0.187     | p=0.963     | p=0.758      |
| Coefficient of correlation (Pearson corelation test)                    | R=0.995     | R=0.995      | R=0.995      | R=0.995     | R=0.998     | R=0.998      |
| Insert  | Tungsten    |              |              |             |             |              |
| Reconstruction  | Standard CT |              | 70 keV PMR   |             | 130 keVPMR  |              |
| Iterative metal artefact reduction                                      | NO          | YES          | NO           | YES         | NO          | YES          |
| <b>Mean dose difference (and standard deviation) in compartments[%]</b> |             |              |              |             |             |              |
| Water in front the insert   | 2.4 (3.9)   | 1.1 (1.8)    | 1.8 (2.9)    | 0.7 (1.6)   | 2.0 (3.5)   | 1.2 (2.0)    |
| Input edge of the insert ( $\pm 2$ mm)                                  | 0.1 (17.2)  | - 5.2 (11.5) | - 1.0 (14.0) | - 5 (11.4)  | 0.0 (17.3)  | - 3.6 (11.7) |
| The insert  | - 7.7 (3.1) | - 8.0 (3.2)  | - 7.7 (3.0)  | - 7.9 (3.2) | - 7.7 (3.0) | - 7.7 (3.0)  |
| Output edge of the insert ( $\pm 2$ mm)                                 | 1.9 (8.3)   | 1.3 (7.4)    | 1.3 (7.7)    | 0.8 (7.0)   | 1.3 (9.7)   | 1.1 (9.4)    |
| Water behind the insert   | - 1.3 (0.2) | - 1.3 (0.2)  | - 1.3 (0.2)  | - 1.4 (0.2) | - 1.8 (0.2) | - 1.9 (0.2)  |
| <b>Comparison of whole PDDs (from 15 to 85 mm)</b>                      |             |              |              |             |             |              |
| Similarity of distribution (Kolmogorov-Smirnov test)                    | p=0.126     | p=0.104      | p=0.094      | p=0.084     | p=0.092     | p=0.078      |
| Coefficient of correlation (Pearson corelation test)                    | R=0.987     | R=0.991      | R=0.990      | R=0.992     | R=0.987     | R=0.991      |

**Table 2.** The statistics of similarity between calculated ( $AXB_{DM}$ : Acuros XB; dose-to-medium approach) and simulated ( $MC_{pla}$ : Monte Carlo; TPS conditions) percentage depth doses, and mean dose difference ( $AXB_{DM} - MC_{pla}$ ) for selected regions of comparison.

iMAR algorithm. Knowing how imaging affects the dose calculation is essential for choosing the proper metal artefact reduction method. Our study shows that the metal reduction strategies have no significant impact on the dose calculation results. Therefore, in our opinion, the selection of the most adequate CT reconstruction should be based on the preferences and experience of the person responsible for the delineation process. Dual-energy tomography and its monoenergetic reconstructions are an interesting metal artefact reduction method. One of the proposed methods is a combination obtained from dual-energy 70 keV monoenergetic scans with iMAR, which was reported<sup>12</sup> to decrease CT number errors and increased image quality. Other work<sup>33</sup> reported the lowest metal artefacts at 130 keV monoenergetic series without iMAR. It is important to highlight that the correct conversion from CT value to relative electron density or physical density is crucial.

A dedicated extended calibration curve should be determined and used for accurate dose calculation<sup>34</sup>. We found no significant impact of imaging mode on the dose calculation process with different strategies leading only to 2% differences and hence no disadvantages of using metal reduction strategies of choice.

This study, for the first time, compared detailed measurement around and inside the metal structure with a set of calculations by different methods using a dedicated phantom. There is a need in the future to translate and validate our phantom findings in clinical conditions.

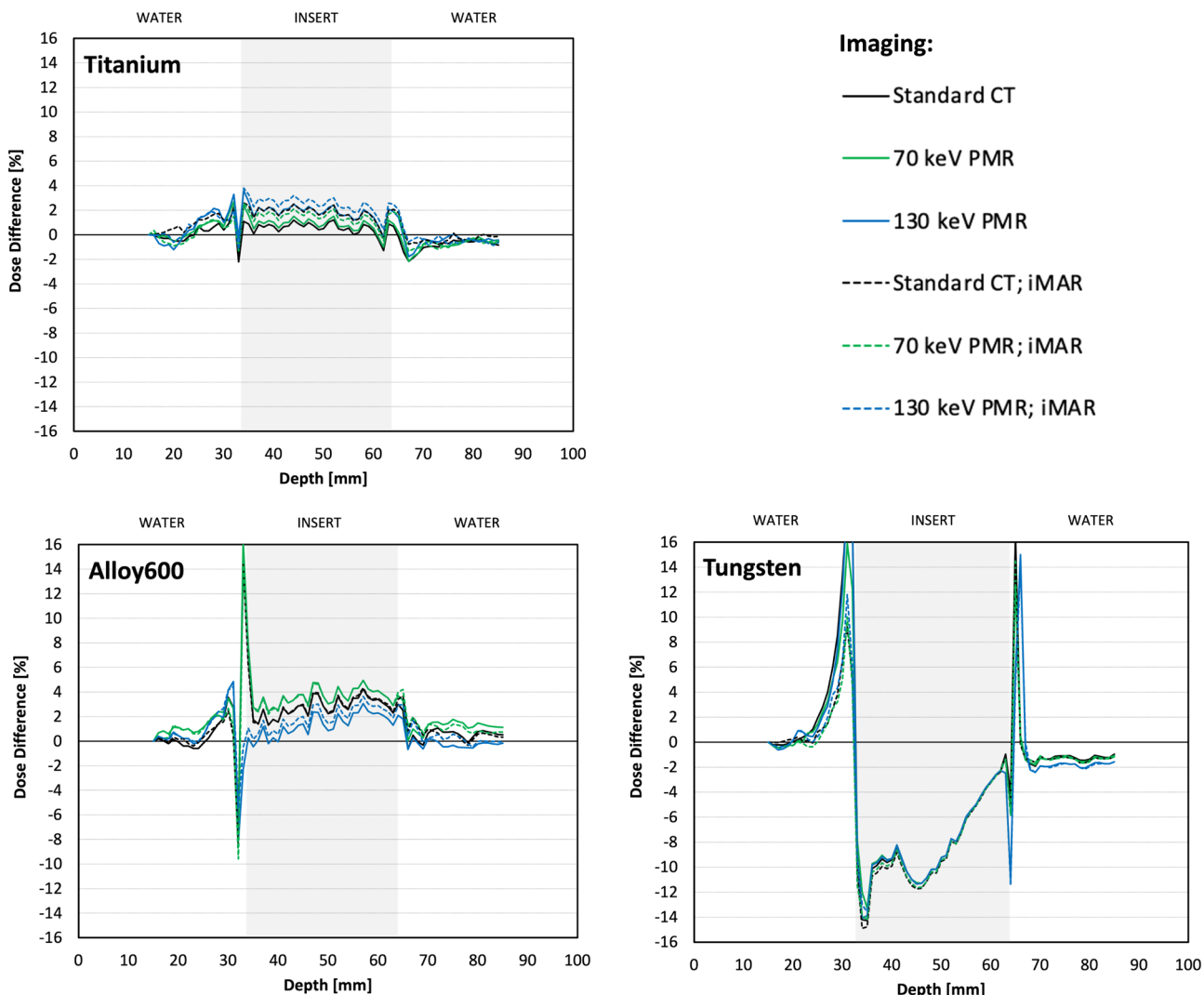


**Figure 6.** Differences between PDDs obtained from Monte Carlo simulations performed for TPS condition and PDDs obtained from TPS calculations using Acuros XB algorithm based on dose-to-medium approach on different CT reconstructions for titanium, alloy 600, and tungsten inserts, respectively.

## Conclusion

The selection of the algorithm for dose calculation was shown to have a significant impact on the accuracy of dose calculation near and inside metals. The Monte Carlo class algorithm should be used for the precise dose calculation as proved by our measurements with a phantom. We found that only the Acuros XB algorithm with a dose-to-medium approach provides comparable accuracy with Monte Carlo method for dose calculation in metal regions when using Eclipse treatment planning system. The limitation of this algorithm is the need to assign material from a predefined library for the high-density objects. Based on the tungsten insert results, it was found that the inability to indicate precise atomic composition leads to calculation errors. The inability of the AAA algorithm to model backscatter dose requires caution in its clinical use for patients with metal implants. However, we found that using an estimated CT value can improve AAA dose calculation behind the metal. No significant impact on the dose calculation was found for a range of metal reduction strategies, suggesting that the choice could be made following clinical operator preference.

## Data availability

All data generated or analysed during this study are included in this published article and its supplementary materials except the selected data (i.e., phase space files) used during Monte Carlo simulations that are provided and licenced by Varian Medical Systems (Palo Alto, USA).

Received: 27 January 2022; Accepted: 25 March 2022

Published online: 08 April 2022

## References

- Barrett, J. F. & Keat, N. Artifacts in CT: Recognition and avoidance. *Radiographics* **24**(6), 1679–1691. <https://doi.org/10.1148/rgr246045065> (2004).
- Bongers, M. N. *et al.* Comparison and combination of dual-energy- and iterative-based metal artefact reduction on hip prosthesis and dental implants. *PLoS ONE* **10**(11), e0143584. <https://doi.org/10.1371/journal.pone.0143584> (2015).
- Lee, M. J. *et al.* Overcoming artifacts from metallic orthopedic implants at high-field-strength MR imaging and multi-detector CT. *Radiographics* **27**(3), 791–803. <https://doi.org/10.1148/rgr273065087> (2007).
- Spadea, M. F., Verburg, J. M., Baroni, G. & Seco, J. The impact of low-Z and high-Z metal implants in IMRT: A Monte Carlo study of dose inaccuracies in commercial dose algorithms. *Med. Phys.* **41**(1), 011702. <https://doi.org/10.1118/1.4829505> (2014).
- Hernandez, S. *et al.* Development and dosimetric assessment of an automatic dental artifact classification tool to guide artifact management techniques in a fully automated treatment planning workflow. *Comput. Med. Imaging Graph.* **90**, 101907. <https://doi.org/10.1016/j.compmedimag.2021.101907> (2021).
- Subhas, N. *et al.* Iterative metal artifact reduction: Evaluation and optimization of technique. *Skeletal Radiol.* **43**(12), 1729–1735. <https://doi.org/10.1007/s00256-014-1987-2> (2014).
- Axente, M. *et al.* Clinical evaluation of the iterative metal artifact reduction algorithm for CT simulation in radiotherapy. *Med. Phys.* **42**(3), 1170–1183. <https://doi.org/10.1118/1.4906245> (2015).
- Morsbach, F. *et al.* Reduction of metal artifacts from hip prostheses on CT images of the pelvis: Value of iterative reconstructions. *Radiology* **268**(1), 237–244. <https://doi.org/10.1148/radiol.13122089> (2013).
- Pawlowski, B., Szweda, H., Dudkowiak, A. & Piotrowski, T. Quality evaluation of monoenergetic images generated by dual-energy computed tomography for radiotherapy: A phantom study. *Phys. Med.* **63**, 48–55. <https://doi.org/10.1016/j.ejmp.2019.05.019> (2019).
- Chapman, D., Smith, S., Barnett, R., Bauman, G. & Yartsev, S. Optimization of tomotherapy treatment planning for patients with bilateral hip prostheses. *Radiat. Oncol.* **9**(1), 43. <https://doi.org/10.1186/1748-717X-9-43> (2014).
- Martin, S. *et al.* Evaluation of tomotherapy MVCT image enhancement program for tumor volume delineation. *J. Appl. Clin. Med. Phys.* **12**(3), 112–121. <https://doi.org/10.1120/jacmp.v12i3.3505> (2011).
- Pawlowski, B., Panek, R., Szweda, H. & Piotrowski, T. Combination of dual-energy computed tomography and iterative metal artefact reduction to increase general quality of imaging for radiotherapy patients with high dense materials. Phantom study. *Phys. Med.* **77**, 92–99. <https://doi.org/10.1016/j.ejmp.2020.08.009> (2020).
- Huang, J. Y. *et al.* Approaches to reducing photon dose calculation errors near metal implants. *Med. Phys.* **43**(9), 5117. <https://doi.org/10.1118/1.4960632> (2016).
- Reft C, Alecu R, Das IJ, Gerbi BJ, Keall P, Lief E, et al. AAPM Radiation Therapy Committee Task Group 63. Dosimetric considerations for patients with HIP prostheses undergoing pelvic irradiation. Report of the AAPM Radiation Therapy Committee Task Group 63. *Med. Phys.* **30**(6):1162–82. <https://doi.org/10.1118/1.1565113> (2003).
- Han, T., Mikell, J. K., Salehpour, M. & Mourtada, F. Dosimetric comparison of Acuros XB deterministic radiation transport method with Monte Carlo and model-based convolution methods in heterogeneous media. *Med. Phys.* **38**(5), 2651–64. <https://doi.org/10.1118/1.3582690> (2011).
- Ojala, J., Kapanen, M., Sipilä, P., Hyödynmaa, S. & Pitkänen, M. The accuracy of Acuros XB algorithm for radiation beams traversing a metallic hip implant—comparison with measurements and Monte Carlo calculations. *J. Appl. Clin. Med. Phys.* **15**(5), 4912. <https://doi.org/10.1120/jacmp.v15i5.4912> (2014).
- Paulu, D. & Alaei, P. Evaluation of dose calculation accuracy of treatment planning systems at hip prosthesis interfaces. *J. Appl. Clin. Med. Phys.* **18**, 9–15. <https://doi.org/10.1002/acm2.12060> (2017).
- Alhakeem, E. A., Alshaikh, S., Rosenfeld, A. B. & Zavgorodni, S. F. Comparative evaluation of modern dosimetry techniques near low- and high-density heterogeneities. *J. Appl. Clin. Med. Phys.* **16**(5), 142–158. <https://doi.org/10.1120/jacmp.v16i5.5589> (2015).
- Bielecka, G., Marach, A., Boehlke, M., Zwierzchowski, G. & Malicki, J. 3D-printed surface applicators for brachytherapy: A phantom study. *J. Contemp. Brachyther.* **13**, 549–562. <https://doi.org/10.5114/jcb.2021.110304> (2021).
- Tino, R. *et al.* Additive manufacturing in radiation oncology: A review of clinical practice, emerging trends and research opportunities. *Int. J. Extrem. Manuf.* **2**, 22. <https://doi.org/10.1088/2631-7990/ab70af> (2020).
- Borca, V. C. *et al.* Dosimetric characterization and use of GAFCHROMIC EBT3 film for IMRT dose verification. *J. Appl. Clin. Med. Phys.* **14**, 4111. <https://doi.org/10.1120/jacmp.v14i2.4111> (2013).
- Sorriaux, J. *et al.* Evaluation of Gafchromic® EBT3 films characteristics in therapy photon, electron and proton beams. *Phys. Med.* **29**, 599–606. <https://doi.org/10.1016/j.ejmp.2012.10.001> (2013).
- Niroomand-Rad, A. *et al.* Report of AAPM Task Group 235 radiochromic film dosimetry: An update to TG-55. *Med. Phys.* **47**(12), 5986–6025. <https://doi.org/10.1002/mp.14497> (2020).
- Constantin, M. *et al.* Modeling the truebeamlinac using a CAD to Geant4 geometry implementation: dose and IAEA-compliant phase space calculations. *Med. Phys.* **38**(7), 4018–4024. <https://doi.org/10.1118/1.3598439> (2011).
- Furuya, T. *et al.* Evaluation of multi-institutional end-to-end testing for post-operative spine stereotactic body radiation therapy. *Phys. Imaging Radiat. Oncol.* **16**, 61–68. <https://doi.org/10.1016/j.phro.2020.09.005> (2020).
- Cheng, Z. J., Bromley, R. M., Oborn, B., Carolan, M. & Booth, J. T. On the accuracy of dose prediction near metal fixation devices for spine SBRT. *J. Appl. Clin. Med. Phys.* **17**(3), 475–485. <https://doi.org/10.1120/jacmp.v17i3.5536> (2016).
- Grams, M. P. *et al.* Cadaveric verification of the Eclipse AAA algorithm for spine SBRT treatments with titanium hardware. *Pract. Radiat. Oncol.* **6**(2), 131–41. <https://doi.org/10.1016/j.prro.2015.10.012> (2016).
- Parenica, H. M. *et al.* VMAT optimization and dose calculation in the presence of metallic hip prostheses. *Technol. Cancer Res. Treat.* **18**, 1533033819892255. <https://doi.org/10.1177/1533033819892255> (2019).
- Lloyd, S. A. & Ans�acher, W. Evaluation of an analytic linear Boltzmann transport equation solver for high-density inhomogeneities. *Med. Phys.* **40**(1), 011707. <https://doi.org/10.1118/1.4769419> (2013).
- Kry, S. F. *et al.* Report dose-to-medium in clinical trials where available: A consensus from the Global Harmonisation Group to maximize consistency. *Radiat. Oncol.* **159**, 106–111. <https://doi.org/10.1016/j.radonc.2021.03.006> (2021).
- Failla, G. A., Wareing, T., Archambault, Y. & Thompson, S. *Acuros XB advanced dose calculation for the Eclipse treatment planning system* (Varian Medical Systems, Palo Alto, CA, 2010).
- Yan, C. *et al.* Clinical implementation and evaluation of the Acuros dose calculation algorithm. *J. Appl. Clin. Med. Phys.* **18**(5), 195–209. <https://doi.org/10.1002/acm2.12149> (2017).
- Zhou, C. *et al.* Monoenergetic imaging of dual-energy CT reduces artifacts from implanted metal orthopedic devices in patients with fractures. *Acad.Radiol.* **18**(10), 1252–1257 (2011).
- Mullins, J. P., Grams, M. P., Herman, M. G., Brinkmann, D. H. & Antolak, J. A. Treatment planning for metals using an extended CT number scale. *J. Appl. Clin. Med. Phys.* **17**, 179–188. <https://doi.org/10.1120/jacmp.v17i6.6153> (2016).

## Acknowledgements

This work was supported by the Greater Poland Cancer Center, Poznan, Poland (Grant No. 3/2021(242)).

### Author contributions

B.P.—the concept of the study, literature analysis, writing the manuscript, phantom construction, EBT3 measurements and data analysis; A.R.—Monte Carlo simulations, data export and writing the manuscript; K.G.—imaging and EBT3 measurements; U.S.K.—treatment planning and data export; R.P.—the concept of the study, literature analysis, writing the manuscript; T.P.—the concept of the study, supervision of Monte Carlo simulation, data management and analysis, literature analysis, and writing the manuscript.

### Competing interests

The authors declare no competing interests.

### Additional information

**Supplementary Information** The online version contains supplementary material available at <https://doi.org/10.1038/s41598-022-10072-8>.

**Correspondence** and requests for materials should be addressed to T.P.

**Reprints and permissions information** is available at [www.nature.com/reprints](http://www.nature.com/reprints).

**Publisher's note** Springer Nature remains neutral with regard to jurisdictional claims in published maps and institutional affiliations.



**Open Access** This article is licensed under a Creative Commons Attribution 4.0 International License, which permits use, sharing, adaptation, distribution and reproduction in any medium or format, as long as you give appropriate credit to the original author(s) and the source, provide a link to the Creative Commons licence, and indicate if changes were made. The images or other third party material in this article are included in the article's Creative Commons licence, unless indicated otherwise in a credit line to the material. If material is not included in the article's Creative Commons licence and your intended use is not permitted by statutory regulation or exceeds the permitted use, you will need to obtain permission directly from the copyright holder. To view a copy of this licence, visit <http://creativecommons.org/licenses/by/4.0/>.

© The Author(s) 2022

Załącznik

**Oświadczenie współautora o wkładzie w publikacje naukowe doktoranta**

prof. dr hab. Alina Dudkowiak  
Politechnika Poznańska  
Wydział Inżynierii Materiałowej i Fizyki Technicznej  
Instytut Fizyki  
ul. Piotrowo 3  
60-965 Poznań

Poznań, dnia 21.11.2022 r.

**Oświadczenie współautora**

dotyczy pracy doktorskiej mgr inż. Bartosza Pawałowskiego

Oświadczam, że w ramach współpracy naukowej opublikowałam z mgr inż. Bartoszem Pawałowskim następującą pracę:

Quality evaluation of monoenergetic images generated by dual-energy computed tomography for radiotherapy: A phantom study.

Autorzy:

Pawałowski Bartosz, Szweda Hubert, Dudkowiak Alina, Piotrowski Tomasz

w której mój wkład polegał na konsultacji wyników.



Załącznik

**Oświadczenie współautora o wkładzie w publikacje naukowe doktoranta**

mgr Hubert Szweda  
Wielkopolskie Centrum Onkologii  
Zakład Fizyki Medycznej  
ul. Garbary 15  
61-866 Poznań

Poznań, dnia 21.12.2021

**Oświadczenie współautora**

dotyczy pracy doktorskiej mgr inż. Bartosza Pawałowskiego

Oświadczam, że w ramach współpracy naukowej opublikowałem z mgr inż. Bartoszem Pawałowskim następującą pracę:

Quality evaluation of monoenergetic images generated by dual-energy computed tomography for radiotherapy: A phantom study.

Autorzy:

Pawałowski Bartosz, Szweda Hubert, Dudkowiak Alina, Piotrowski Tomasz

w której mój wkład polegał na pomocy w wykonaniu pomiarów oraz przygotowaniu rekonstrukcji obrazów.

*Hubert Szweda*

Załącznik

**Oświadczenie współautora o wkładzie w publikacje naukowe doktoranta**

Prof. dr hab. Tomasz Piotrowski  
Uniwersytet Medyczny w Poznaniu  
Wydział Medyczny  
Katedra Elektroradiologii  
Ul. Garbary 15  
61-866 Poznań

Poznań, dnia 21.11.2022

**Oświadczenie współautora**

dotyczy pracy doktorskiej mgr inż. Bartosza Pawałowskiego

Oświadczam, że w ramach współpracy naukowej opublikowałem z mgr inż. Bartoszem Pawałowskim następującą pracę:

Quality evaluation of monoenergetic images generated by dual-energy computed tomography for radiotherapy: A phantom study.

Autorzy:

Pawałowski Bartosz, Szweda Hubert, Dudkowiak Alina, Piotrowski Tomasz

w której mój wkład polegał na analizie wyników i ostateczne redakcji artykułu.



Załącznik

**Oświadczenie współautora o wkładzie w publikacje naukowe doktoranta**

mgr Hubert Szweda  
Wielkopolskie Centrum Onkologii  
Zakład Fizyki Medycznej  
ul. Garbary 15  
61-866 Poznań

Poznań, dnia 21.12.2021

**Oświadczenie współautora**

dotyczy pracy doktorskiej mgr inż. Bartosz Pawałowskiego

Oświadczam, że w ramach współpracy naukowej opublikowałem z mgr inż. Bartoszem Pawałowskim następującą pracę:

Combination of dual-energy computed tomography and iterative metal artefact reduction to increase general quality of imaging for radiotherapy patients with high dense materials.  
Phantom study.

Autorzy:

Pawałowski Bartosz, Panek Rafał, Szweda Hubert, Piotrowski Tomasz

w której mój wkład polegał na pomocy w wykonaniu pomiarów oraz rekonstrukcji danych.

*Hubert Szweda*

Załącznik

**Oświadczenie współautora o wkładzie w publikacje naukowe doktoranta**

Rafał Panek  
Department of Medical Physics & Clinical Engineering  
Nottingham University Hospitals NHS Trust  
Nottingham  
United Kingdom

Poznań, dnia 21.11.2022

**Oświadczenie współautora**

dotyczy pracy doktorskiej mgr inż. Bartosz Pawałowskiego

Oświadczam, że w ramach współpracy naukowej opublikowałem z mgr inż. Bartoszem Pawałowskim następującą pracę:

Combination of dual-energy computed tomography and iterative metal artefact reduction to increase general quality of imaging for radiotherapy patients with high dense materials.  
Phantom study.

Autorzy:

Pawałowski Bartosz, Panek Rafał, Szweda Hubert, Piotrowski Tomasz

w której mój wkład polegał na analizie wyników i redakcji artykułu.

*Rafał Panek*

Załącznik

**Oświadczenie współautora o wkładzie w publikacje naukowe doktoranta**

Prof. dr hab. Tomasz Piotrowski  
Uniwersytet Medyczny w Poznaniu  
Wydział Medyczny  
Katedra Elektroradiologii  
Ul. Garbary 15  
61-866 Poznań

Poznań, dnia 21.11.2022

**Oświadczenie współautora**

dotyczy pracy doktorskiej mgr inż. Bartosz Pawałowskiego

Oświadczam, że w ramach współpracy naukowej opublikowałem z mgr inż. Bartoszem Pawałowskim następującą pracę:

Combination of dual-energy computed tomography and iterative metal artefact reduction to increase general quality of imaging for radiotherapy patients with high dense materials.  
Phantom study.

Autorzy:

Pawałowski Bartosz, Panek Rafał, Szweda Hubert, Piotrowski Tomasz

w której mój wkład polegał na analizie wyników i ostatecznej redakcji artykułu.



Załącznik

**Oświadczenie współautora o wkładzie w publikacje naukowe doktoranta**

Mgr Adam Ryczkowski  
Wielkopolskie Centrum Onkologii  
Zakład Fizyki Medycznej  
ul. Garbary 15  
61-866 Poznań

Poznań, dnia 21.11.2022

**Oświadczenie współautora**

dotyczy pracy doktorskiej mgr inż. Bartosz Pawałowskiego

Oświadczam, że w ramach współpracy naukowej opublikowałem z mgr inż. Bartoszem Pawałowskim następującą pracę:

Accuracy of the doses computed by the Eclipse treatment planning system near and inside metal elements.

Autorzy:

Pawałowski Bartosz, Ryczkowski Adam, Panek Rafał, Sobocka-Kurdyk Urszula, Graczyk Kinga, Piotrowski Tomasz

w której mój wkład polegał na opracowaniu symulacji Monte Carlo.



Załącznik

**Oświadczenie współautora o wkładzie w publikacje naukowe doktoranta**

Rafał Panek  
Department of Medical Physics & Clinical Engineering  
Nottingham University Hospitals NHS Trust  
Nottingham  
United Kingdom

Nottingham, dnia 21.11.2022

**Oświadczenie współautora**

dotyczy pracy doktorskiej mgr inż. Bartosz Pawałowskiego

Oświadczam, że w ramach współpracy naukowej opublikowałem z mgr inż. Bartoszem Pawałowskim następującą pracę:

Accuracy of the doses computed by the Eclipse treatment planning system near and inside metal elements.

Autorzy:

Pawałowski Bartosz, Ryczkowski Adam, Panek Rafał, Sobocka-Kurdyk Urszula, Graczyk Kinga, Piotrowski Tomasz

w której mój wkład polegał na analizie wyników i redakcji artykułu.

*Rafał Panek*

Załącznik

**Oświadczenie współautora o wkładzie w publikacje naukowe doktoranta**

Mgr Urszula Sobocka- Kurdyk  
Wielkopolskie Centrum Onkologii  
Zakład Fizyki Medycznej  
ul. Kaszubska 12  
62-800 Kalisz

Poznań, dnia 21.11.2022

**Oświadczenie współautora**

dotyczy pracy doktorskiej mgr inż. Bartosz Pawałowskiego

Oświadczam, że w ramach współpracy naukowej opublikowałem z mgr inż. Bartoszem Pawałowskim następującą pracę:

Accuracy of the doses computed by the Eclipse treatment planning system near and inside metal elements.

Autorzy:

Pawałowski Bartosz, Ryczkowski Adam, Panek Rafał, Sobocka-Kurdyk Urszula, Graczyk Kinga, Piotrowski Tomasz

w której mój wkład polegał na przygotowaniu planów leczenia z wykorzystaniem różnych modeli obliczeniowych.

*Urszula Sobocka - Kurdyk*

Załącznik

**Oświadczenie współautora o wkładzie w publikacje naukowe doktoranta**

Mgr Kinga Graczyk  
Wielkopolskie Centrum Onkologii  
Zakład Fizyki Medycznej  
ul. Garbary 15  
61-866 Poznań

Poznań, dnia 21.11.2022

**Oświadczenie współautora**

dotyczy pracy doktorskiej mgr inż. Bartosz Pawałowskiego

Oświadczam, że w ramach współpracy naukowej opublikowałem z mgr inż. Bartoszem Pawałowskim następującą pracę:

Accuracy of the doses computed by the Eclipse treatment planning system near and inside metal elements.

Autorzy:

Pawałowski Bartosz, Ryczkowski Adam, Panek Rafał, Sobocka-Kurdyk Urszula, Graczyk Kinga, Piotrowski Tomasz

w której mój wkład polegał na opracowaniu wyników uzyskanych metodami dozymetrii filmowej.

Kinga Graczyk

Załącznik

**Oświadczenie współautora o wkładzie w publikacje naukowe doktoranta**

Prof. dr hab. Tomasz Piotrowski  
Uniwersytet Medyczny w Poznaniu  
Wydział Medyczny  
Katedra Elektroradiologii  
Ul. Garbary 15  
61-866 Poznań

Poznań, dnia 21.11.2022

**Oświadczenie współautora**

dotyczy pracy doktorskiej mgr inż. Bartosz Pawałowskiego

Oświadczam, że w ramach współpracy naukowej opublikowałem z mgr inż. Bartoszem Pawałowskim następującą pracę:

Accuracy of the doses computed by the Eclipse treatment planning system near and inside metal elements.

Autorzy:

Pawałowski Bartosz, Ryczkowski Adam, Panek Rafał, Sobocka-Kurdyk Urszula, Graczyk Kinga, Piotrowski Tomasz

w której mój wkład polegał na analizie wyników i ostatecznej redakcji artykułu.

